

INFORMATION TO USERS

This manuscript has been reproduced from the microfilm master. UMI films the text directly from the original or copy submitted. Thus, some thesis and dissertation copies are in typewriter face, while others may be from any type of computer printer.

The quality of this reproduction is dependent upon the quality of the copy submitted. Broken or indistinct print, colored or poor quality illustrations and photographs, print bleedthrough, substandard margins, and improper alignment can adversely affect reproduction.

In the unlikely event that the author did not send UMI a complete manuscript and there are missing pages, these will be noted. Also, if unauthorized copyright material had to be removed, a note will indicate the deletion.

Oversize materials (e.g., maps, drawings, charts) are reproduced by sectioning the original, beginning at the upper left-hand corner and continuing from left to right in equal sections with small overlaps.

Photographs included in the original manuscript have been reproduced xerographically in this copy. Higher quality 6" x 9" black and white photographic prints are available for any photographs or illustrations appearing in this copy for an additional charge. Contact UMI directly to order.

ProQuest Information and Learning
300 North Zeeb Road, Ann Arbor, MI 48106-1346 USA
800-521-0600

UMI[®]

New Techniques for Computing and Factorizing Feynman Diagrams

Yongjian Feng

*Department of Physics, McGill University
3600 University St. Montreal, P.Q., Canada H3A 2T8*

**A thesis submitted to the Faculty of Graduate Studies
and Research in partial fulfillment of the requirement for
the degree of Doctor of Physics.**

(C) Yongjian Feng, Aug. 1999



**National Library
of Canada**

**Acquisitions and
Bibliographic Services**

**395 Wellington Street
Ottawa ON K1A 0N4
Canada**

**Bibliothèque nationale
du Canada**

**Acquisitions et
services bibliographiques**

**395, rue Wellington
Ottawa ON K1A 0N4
Canada**

Your file Votre référence

Our file Notre référence

The author has granted a non-exclusive licence allowing the National Library of Canada to reproduce, loan, distribute or sell copies of this thesis in microform, paper or electronic formats.

The author retains ownership of the copyright in this thesis. Neither the thesis nor substantial extracts from it may be printed or otherwise reproduced without the author's permission.

L'auteur a accordé une licence non exclusive permettant à la Bibliothèque nationale du Canada de reproduire, prêter, distribuer ou vendre des copies de cette thèse sous la forme de microfiche/film, de reproduction sur papier ou sur format électronique.

L'auteur conserve la propriété du droit d'auteur qui protège cette thèse. Ni la thèse ni des extraits substantiels de celle-ci ne doivent être imprimés ou autrement reproduits sans son autorisation.

0-612-64557-6

Canada

Acknowledgement

First I want to express my deep appreciation to my supervisor Professor C.S. Lam for his patient, guidance, encouragement, and countless inspiring, stimulating discussions on this subject. And I also want to thank Professor R. Myers, Professor C. Burgess and Professor J. Cline for everything I learnt from them.

It was a great experience for studying in McGill University in the last several years. I also want to thank my previous colleague O. Hamidi-Ravari for his co-operation.

Finally I want to thank my colleague Kim-Tuan Nguyen who helps me to translate the abstract and Van Fong who helps me to check the manuscript. Special thanks to Prof. C. Gale for his help to correct the French version abstract.

Abstract

It is found experimentally that total cross sections increase with energy. Partonic total cross sections can be calculated in perturbative QCD provided the coupling constant is small, though multiloop diagrams must be included at high energies. Such calculations are difficult and can usually be carried out only in the leading-log approximation. The resulting BFKL Pomeron violates the Froissart bound, which forbids total cross sections asymptotically to grow faster than the square of the logarithm of energy. To restore unitarity and the Froissart bound, subleading contributions of all orders must be included. Unfortunately existing techniques for computing Feynman diagrams prove to be inadequate for this difficult task. The purpose of this thesis is to develop new techniques capable of solving this problem. Since factorization in the impact-parameter space is a main ingredient needed to reach unitarity, such a technique must be capable of implementing factorization in an efficient way. We introduce the non-abelian cut diagrams for that purpose. We use it to compute quark-quark scattering amplitude to the two-loop order and show how the new technique can overcome the inadequacies of the existing method. We are also able to use this method to prove factorization of a class of Feynman diagrams, which we shall refer to as 's-channel ladder diagrams', though the proof of general factorization is not attempted in this thesis. We have also developed a more efficient method to calculate the high-energy dependences of individual Feynman and non-abelian cut diagrams. This method relies on a systematic study of the paths used by momenta to flow through the diagram, and will thus be referred to as the path method for flow diagrams. These new techniques can be used to implement unitarity and to restore the Froissart bound, but this final goal is not carried out here.

ABSTRACT

Expérimentalement, il a été démontré que la section efficace totale augmente avec l'énergie. Les sections efficaces partoniques totales peuvent être calculées en QCD perturbatif tant que la constante de couplage est petite, sans toutefois oublier que les diagrammes à boucles multiples doivent être inclus aux énergies élevées. De tels calculs sont complexes et ne peuvent être effectués qu'à l'approximation du logarithme dominant. Il en résulte que le Poméron BFKL viole la limite de Froissart, laquelle stipule que la section efficace ne peut varier de façon asymptotique plus rapidement que le carré du logarithme de l'énergie. Pour restorer l'unitarité ainsi que la limite de Froissart, des contributions de tous ordres doivent être incluses. Malheureusement, les méthodes actuelles pour calculer les diagrammes de Feynman sont inadéquates pour ce genre de tâche. Le but de cette thèse est donc de développer de nouvelles techniques capable de résoudre ce problème. Étant donné que la factorisation dans l'espace de paramètre d'impact est un élément essentiel pour atteindre l'unitarité, une telle technique se doit d'implémenter la factorisation de manière efficace. C'est dans ce but qu'on introduit des diagrammes coupés non-Abéliens. On les utilise pour calculer l'amplitude de dispersion quark-quark à l'ordre de la double boucle et on démontre que la nouvelle technique est la solution aux faiblesses des techniques actuelles. Cette méthode peut aussi être utilisée pour prouver la factorisation d'une classe de diagrammes de Feynman, les diagrammes échelle dans le canal s . Toutefois, la preuve de cette factorisation ne fera pas partie de cette thèse. Nous avons aussi développé une méthode plus efficace pour calculer les diagrammes individuels de Feynman ainsi que les diagrammes coupés non-Abéliens aux hautes énergies. Cette méthode se base sur une étude systématique des parcours de l'impulsion à travers le diagramme; Ces nouvelles techniques peuvent être utilisées pour restorer et la limite de Froissart.

List of Figures

1	HERA experiment of electron-proton collision.	3
2	Reggeon exchange diagram.	7
3	An elastic process $A + B \rightarrow A + B$	19
4	Contour integral.	20
5	Feynman diagrams in QCD contributing to an octet exchange.	24
6	An inelastic scattering of gluons.	28
7	First order Feynman diagrams in Lipatov vertex.	32
8	One of the diagrams contributing to BFKL Pomeron.	36
9	Multi-reggeon exchange diagrams in QCD.	42
10	QED diagrams for $ee \rightarrow ee$. Here solid lines are used to denote fermion, and the thin lines are used for photons.	44
11	A tree level Feynman diagram in QED.	44
12	6th order Feynman diagrams in QED.	47
13	A relation between QED cut diagrams.	48
14	Two examples of flow diagrams.	57
15	Feynman diagrams for quark-quark elastic scattering at 6th order.	71
16	An example of using non-abelian cut diagram.	72
17	Non-abelian cut diagrams.	73
18	Graphical representation of the identities in $SU(N_c)$ algebra.	74

19	Reorganization of $\bar{C}1$ and $\bar{C}2$ for 6th order.	75
20	An example of how to cut diagram C6.	76
21	Reorganization of 6th order diagrams with upside-down Y vertex. . .	76
22	Decomposition of the color factor of C3 into planar color diagram. . .	78
23	Color decomposition of 6th order diagrams with Y vertex.	79
24	Color decomposition of 6th order diagrams with Y vertex.	79
25	Color decomposition of 6th order diagrams with Y vertex.	80
26	Color decomposition of all the cut diagrams at 6th order.	81
27	Flow diagram for $B2_c, \bar{C}1_c, C11_c, \bar{C}2_c,$ and $C19_c$	84
28	Summing cut diagrams to introduce cut in the lower fermion line. . .	86
29	The connection between cuts and factorization.	90
30	Examples of 8th order SC diagrams.	96
31	An example of the decomposition of SCC diagrams into sums of re- duced diagrams.	100
32	Examples of how primitive color factors are obtained from reduced components.	102
33	An example of a disconnected reduced diagram and the corresponding regge color factor.	103
34	An example of a connected reduced diagram that is not primitive. . .	103
35	Another example of a connected reduced diagram that is not primitive.	104
36	An example of re-organizing diagrams.	106

37	Folding formula.	112
38	B2c and C2c	119
39	Cancellation of the non primitive color factor.	122

Contents

1	Introduction	1
2	Regge pole theory and Reggeon	17
2.1	Regge pole theory	18
2.1.1	Sommerfeld-Watson transformation	18
2.1.2	Asymptotic behavior	21
2.2	Reggeization of gluons in QCD	22
2.2.1	Rapidity and light-cone coordinate	24
2.2.2	Multi-Regge limit	27
3	BFKL Pomeron	30
3.1	BFKL equation	31
3.2	Unitarity problem of the BFKL pomeron	39
4	Multi-Reggeon exchanges	41
4.1	QED eikonal formula	43
4.1.1	eikonal formula for QED	44
4.1.2	Cut diagram in QED	47
4.2	Generalization to QCD and related difficulties	50
5	Relevant techniques	55
5.1	Path method for integration	55

5.1.1	Residue calculus and flow diagram	55
5.1.2	Line reversal and path method	58
5.2	Non-abelian cut diagram	67
6	Calculation of diagrams up to 6th order	70
7	High order calculation	93
7.1	Color factors	98
7.2	Factorisation of sums of spacetime amplitudes	105
8	Conclusion	108
A	Multiple commutator formula	111
B	Spacetime amplitudes	115
C	Color factors of nonabelian cut diagrams	121

Chapter I. Introduction

It is well-known that there are four fundamental forces in the universe, namely gravity, electromagnetic, weak, and strong forces. They govern the interactions among all the elements in the universe, as large as a planet and as small as an atom. To better understand these four fundamental forces is still the central theme of modern theoretical physics. The topic of this thesis explores the region of strong interaction.

The strong interaction is one of the fundamental forces at the nuclear and sub-nuclear level. A nucleus is known to be made up of neutrons and protons, which in turn consist of quarks and gluons. According to the 'constituent' quark model invented by Gell-Mann and Zweig [1], quarks are considered as fundamental particles. They carry fractional electric charges as well as a new kind of quantum number called color. Afterwards, Quantum Chromodynamics (QCD) was developed to describe interactions between quarks. Just like in Quantum Electrodynamics (QED) whose quantum is called 'photon' and couples to charge in a universal manner, there is also a quantum called 'gluon' in QCD, which couples to color universally. Hence quarks with different colors interact with each other by exchanging gluons. But what makes QCD more complicated than QED is that the gluons, themselves carrying color, can also interact with one another directly. Through these interactions,

quarks and gluons are strongly bound together to form different kinds of strongly-interacting particles in the universe. These particles are all colorless although gluons and quarks carry color.

The most important features of QCD are asymptotic freedom and the confinement of quarks. They refer to the fact that the interaction between quarks and gluons at short distance is weak, while at long distance becomes so strong that the colored objects can never be isolated from one another. Using perturbation theory, QCD can successfully explain all the experimental phenomena in the large momentum-transfer region.

However, there are still areas requiring more efforts. One of the unsolved problems at hand is the behavior of the total cross section of hadron-hadron scattering. It was found in experiments that the total cross section σ of the proton-proton scattering remains roughly constant in a region $10\text{GeV} < \sqrt{s} < 10^3\text{GeV}$, when s , the square of center-of-mass energy, increases. But after \sqrt{s} goes beyond 10^3GeV , σ begins to rise slowly. This rise can be fitted by [2]

$$\sigma \sim s^{0.08} \quad (1.1)$$

Qualitatively, this phenomenon of rising cross-section can be explained as follows. In the region of $10\text{GeV} < \sqrt{s} < 10^3\text{GeV}$, σ is determined by the size of the proton, which is about 1fm . But as s increases further, the virtual gluon clouds surrounding the protons become less and less transparent. Then the contribution from this opaque

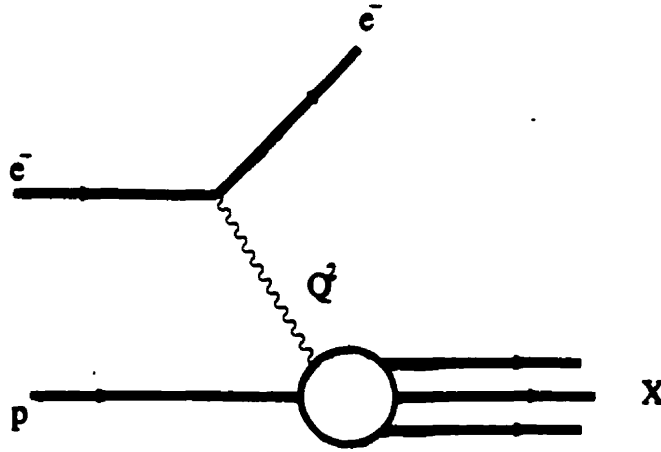


Figure 1: HERA experiment of electron-proton collision.

gluon cloud cannot be ignored, and equivalently, this increases the effective size of the proton and leads to the rise of the total cross section.

More recently, HERA [3] has measured the total cross section of a virtual photon colliding with a proton. It was found that this cross section can also be described by a power law behavior

$$\sigma \sim s^\lambda. \quad (1.2)$$

The exponent λ varies with the virtuality Q^2 of the photon, being chosen to 0.08 at $Q^2 = 0$, and increases to about 0.2 to 0.3 at the largest Q available. This experiment in HERA is performed by making an electron collide with a proton. The electron emits a photon with high virtuality Q^2 , and this virtual photon interacts with the proton as shown in Fig. 1.

To get the data for the total cross sections like equ. (1.1) and (1.2) experimentally, we can either measure the total cross section directly, or alternatively we can measure

the corresponding forward elastic scattering amplitude. These two are known to be related by the Optical Theorem as will be briefly explained below. The forward elastic scattering amplitude measures the loss of the incoming beam in the forward direction. According to the conservation of probability, this loss is caused by elastic and inelastic scatterings included in the total cross section. Hence the Optical Theorem. For simplicity, in the following, we shall focus on near-forward elastic scattering amplitude as a means of getting the elastic and the total cross section.

Scatterings are caused by the exchange of objects between the interacting particles. Particularly, in elastic scatterings this object must carry vacuum quantum number in order to preserve the quantum numbers of the scattered particles. At high energy, the object which gives rise to the dominant contribution to the elastic scattering is called the Pomeron. The contribution to equ. (1.2) is referred as the hard Pomeron [4] because the virtual photon carries large virtuality Q^2 . The one contributing to equ. (1.1) is called the soft Pomeron [5] since particles are always on-shell. It is difficult to calculate the soft Pomeron because confinement effects cannot be neglected in the corresponding region. On the other hand, since in equ. (1.2) the virtual photon carries large momentum transfer, it is possible that perturbative QCD can be applied to explain the hard Pomeron effect. The fundamental degrees of freedom in QCD are quarks and gluons, and it is known that using the dipole model [6, 7], quark-quark elastic scattering can be related to the hadron-hadron elastic scattering. As a result, from now on in this thesis, we shall focus on near

forward elastic scattering of quarks and gluons.

The first model to explain Pomeron employing perturbative QCD is the Low-Nussinov model [8]. It can be illustrated by using the electron-proton scattering shown in Fig. 1. The virtual photon emitted by the electron splits into a quark-antiquark pair. They interact with the quarks inside the incoming proton by exchanging gluons. Since gluon carries octet color, a single gluon exchange cannot contribute to proton-proton elastic scattering, although it has the smallest power of the coupling constant. The two-gluon process, on the other hand, contributes to both the color singlet and octet channels. Therefore, as a first approximation, Low and Nussinov proposed that QCD Pomeron be constructed by two gluons.

In the Low-Nussinov model, all the higher order processes are ignored. These processes are however important for improving this model, especially at the high energy limit we are taking. The reason is because calculations show that in the high energy limit, the coupling constant g^2 often appears with a factor of $\ln s$. Together they form an effective coupling constant, which governs interactions at this energy level. Potentially, this effective coupling constant can be close to 1 or even larger when s is large, even if the coupling constant itself remains very small in the perturbative QCD region. As a result, higher order corrections cannot be ignored when we try to explain the hard Pomeron by perturbative QCD, and what we really need then is a summation up to all orders of the coupling constant in the perturbative expansion.

It is clear that such a summation is not an easy one, since in perturbative QCD, the scattering amplitude is calculated *order by order* using Feynman diagrams. At high order, the number of the Feynman diagrams becomes very large, and each of them becomes very complicated to compute. It is beyond our computational ability to calculate every one of them without any approximation, let alone doing the summation. A conceivable solution is to isolate the leading contribution from each Feynman diagram, and do the summation over these leading terms at the high energy limit. This can greatly simplify the calculations, because the leading terms have relatively simpler structures compared with the non-leading ones. At large s , the leading term appears as a power of $\ln s$, and this approximation is usually called the leading logarithm approximation.

The leading logarithm approximation was used by Balitskii, Lipatov and others [10, 11, 13, 14], as well as by Lipatov and his colleagues to investigate the QCD Pomeron problem. They first calculated the inelastic scattering of two quarks going to two quarks and n gluons. It was found that the leading contribution from Feynman diagrams to this inelastic scattering can be summed up in the high energy limit. Furthermore, by the help of dispersion relation, the above result was used to calculate quark-quark two-body scattering. Lipatov and his colleagues were able to show that the final result satisfies an integral equation, call the BFKL equation [10]. This equation can be solved for the color octet channel exactly, and for the singlet channel approximately.

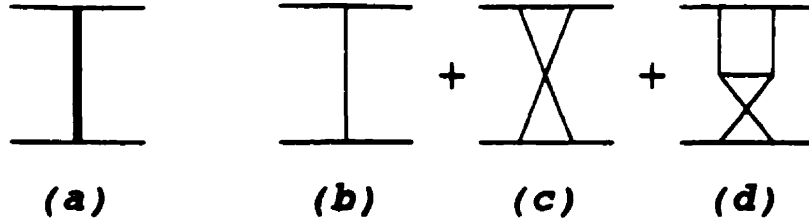


Figure 2: Reggeon exchange diagram.

For the octet channel solution, the amplitude computed by Lipatov is proportional to $s^{\alpha(\Delta)}$, where Δ is the momentum transfer, and the actual expression of $\alpha(\Delta)$ is given later in Chapter III. As we know, if two particles scatter by exchanging an elementary object with spin j , then the amplitude at high energy is proportional to s^j . Therefore this result shows that the object being exchanged in the color octet channel carries an effective spin of $\alpha(\Delta)$. Such an object is called a Reggeon, and this effective spin $\alpha(\Delta)$ is called a Regge trajectory. This process can be shown in Fig. 2(a), where we use solid line to represent the Reggeon, or the *reggeized gluon*. It should be noted that a single diagram like Fig. 2(a) should be viewed as the sum of an infinite number of Feynman diagrams such as Fig.2(b, c, and d).

The solution in the singlet channel leads to a cross section which is approximately

$$\sigma \sim s^{\frac{11\alpha_0}{4}}, \quad (1.3)$$

where $\alpha = g^2/4\pi$. At the energy of the mass of Z (91Gev), g can be taken as 0.2, and

this makes the power of s to be 0.529, which is twice as large as the hard Pomeron result from HERA. Although the recently published 2nd order correction [15] makes this power lower, the numerical disagreement, either big or small, is however only the result of a more serious problem about the BFKL Pomeron, as we shall explain below. Now 3rd order correction is under discussion in [16].

This serious problem of the BFKL Pomeron is that it violates the Froissart bound [17] if extrapolated to the infinite energy limit. In quantum field theory, there is a theorem stating that to preserve unitarity, the s -dependence of the total cross section in the asymptotic limit cannot exceed $\ln^2 s$. This is known as the Froissart bound. This bound is violated by the BFKL Pomeron as can be seen in equation (1.3). At the energy level of HERA, s is large but not infinite. So an apparent violation of the Froissart bound is not disastrous. However, since the BFKL Pomeron is calculated by using the leading logarithm approximation, equation (1.3) should be more applicable for large s . This then will inevitably lead to a violation of the Froissart bound.

The real reason for this violation is that BFKL Pomeron does not obey the fundamental principle of probability conservation, otherwise known as unitarity. This has been a long standing and difficult problem, because the unitarity equation is highly nonlinear and difficult to solve. The purpose of this thesis is to make a preliminary investigation of this problem, and to develop theoretical tools needed for its solution. The new tools are discussed mainly in Chapter V, with an illustration

of their application in Chapter VI. They will be used to investigate a factorization property needed for unitarization. This is carried out in Chapters VII and VIII for special sets of diagrams; the application of these tools to the full solution of the unitarity problem can be found in Ref. [18]

To understand the role of unitarity, we assume that in the high energy limit QCD interactions are described by multiple reggeon exchange as well as productions and absorptions of gluons between these reggeons. All the gluons along the s -channel are reggeized. According to the unitarity relation, the imaginary part of the scattering amplitude M_{fi} can be expressed as

$$\text{Im } M_{fi} = 1/2 \sum_n (2\pi)^4 \delta^4(P_i - P_n) \frac{M_{fn}^* M_{ni}}{\prod_k f_k}, \quad (1.4)$$

where P_i and P_f are the total four-dimensional momenta of the initial and final states, and f_k is defined to be E_k/m for a fermion with energy E_k and mass m , or $2E_k$ for a boson. It can be seen that if there is a two-reggeon contribution in the scattering amplitude M , putting this on the right hand side of the above equation will generate the imaginary part of a four-reggeon exchange amplitude. That is to say, if the two reggeon exchange contribution is included in the scattering amplitude, the unitarity relation above requires the four-reggeon exchange amplitude to be there as well. Using a similar procedure, it can be shown further that keeping the two and four reggeon exchange amplitudes will generate the six reggeon exchange amplitudes etc. As a result, the multi-reggeon exchange amplitudes are interrelated, and the

two reggeon exchange amplitude cannot be isolated without violating unitarity.

From the above discussion, it is clear that in order to unitarize the BFKL Pomeron it is necessary to include the multi-reggeon exchange contributions provided the assumption we made above is true. Therefore, the first question we need to answer is whether the elastic scattering amplitude at the high energy limit can be described by multi-reggeon exchange contributions, even though 3-reggeon contribution, called Odderon[19], and 4-reggeon contribution[20], have already been studied.

Since in perturbative QCD, scattering amplitude is given by summing Feynman diagrams of different orders, this question can then be re-phrased as to whether multi-reggeon exchange contributions can be obtained by summing Feynman diagrams in the leading logarithm approximation. It is far from obvious that the Reggeon diagrams and the Feynman diagrams are related. Although the reggeon diagrams shown in Fig. 2 look like Feynman diagrams, they are actually very different. First of all, the reggeon, although carrying the same color as the gluon, has a different propagator shown as

$$\frac{g^2}{\Delta^2} s^{(\alpha(\Delta))} . \quad (1.5)$$

Secondly, the production and absorption of gluon from a reggeon are described by a new coupling called a Lipatov vertex[21], instead of the triple gluon vertex in ordinary Feynman diagram[22]. In addition, the particles involved in reggeon

diagrams carry two-dimensional momentum, while particles in a Feynman diagram carry four-dimensional momentum. Finally, unlike gluons, the reggeons exchanged in the t -channel are *factorized* along the s -channel, and they do not cross each other.

To prove that the reggeon diagrams in Fig. 2 can be obtained from summing Feynman diagrams, we need to satisfy at least these four points. Lipatov and his co-workers have done a lot[10] about the first two points as we are going to review in the next sections, and in this thesis the last two points are the main topic.

To “reduce” the four-dimensional momentum into a two-dimensional one, we need to make use of the high energy approximation. In a near-forward scattering in the high energy limit, the momenta of the two incoming particles span the longitudinal subspace. All the momenta in the transverse subspace are considered to be order of 1 as $s \rightarrow \infty$. Therefore, to get to the first point above, we need to perform the integration of the longitudinal momenta to get the s dependence for individual Feynman diagram, and then sum up the results. It should be noticed that usually this calculation for each Feynman diagram can only be performed for the leading logarithm order because of the complicated structure of each multiloop diagram of high order. However, as shown by calculations in the literatures, the leading logarithm from individual Feynman diagrams unfortunately get cancelled quite often when we sum up Feynman diagrams, and the first difficulty we encounter is that to obtain useful result, we are forced to retain subleading or even subsubleading contribution.

A good example to see this cancellation is the electron-electron elastic scattering in QED by exchanging photons. As stated before, each loop in a Feynman diagram can potentially contribute a factor of $g^2 \ln s$. For an n -loop level Feynman diagram, the leading contribution can possibly be of the order of $\ln^n s$, which can easily exceed the Froissart bound because n varies from 0 to ∞ . Practical calculations show that all the contributions from individual Feynman diagrams of the order of $\ln^n s$ with $n \geq 1$ get cancelled in the summation [23]. This means that for each Feynman diagram, we must keep the contribution to the order independent of s , and so a direct calculation using Feynman diagrams is extremely difficult, if not impossible.

For the QCD case, Cheng, Wu and their colleagues calculated the quark-quark elastic scattering by using Feynman diagrams. They were able to prove up to the 6th order of the coupling constant that summing Feynman diagrams does give the multi-reggeon exchange amplitudes. It is these cancellations that make the computations complicated in higher order, so Cheng and colleagues were only able to partially calculate them up to the 8th and the 10th order [24, 25, 26]. Similar discussion can also be found in [27].

The cancellation of the leading contributions is not an accident to make life difficult. It is actually essential for the unitarity to be preserved. According to the multi-reggeon amplitudes, the leading contributions are of the order of

$$(g^2)^n s (g^2 \ln^2 s)^m, \quad (1.6)$$

where n is the corresponding number of Reggeons. In the case of the 8th order calculations, if $n = 3$, then the contributions to retain are of order $\ln s$. Since a three-loop Feynman diagram can potentially give $\ln^3 s$, this means the leading and subleading contributions will all be cancelled, and subsubleading order must be maintained.

To deal with this difficulty, it is worthwhile to look at the similar process in QED in more detail. The same difficulty exists in the QED case. It was solved by using the so-called eikonal formula[28, 29]. For an n photon exchange process, the $n!$ Feynman diagrams required by gauge invariance can be represented by a single expression which is independent of s . Since nothing else is present to cancel it, it can be evaluated just using the leading approximation.

This problem can be viewed from different angle. The photons obey Bose-Einstein statistics. In a multi-photon process, the involved photons interfere with each other and generate narrow peaks, which essentially are δ functions. It turns out that this is a destructive interference. The final expression, which is the eikonal[29] expression in the case of QED, has already taken account this interference.

However the eikonal formula is suitable for vertices that are effectively number, or a scalar. This is true for QED. But for QCD, because the gluons carry color and can couple to themselves, it is described by a non-abelian gauge theory[30], and the corresponding vertices in this theory are color matrices[22], which do not commute with each other. The original eikonal formula cannot be applied on QCD. On the

other hand, gluons are also Bose-Einstein particles. As an analogy to QED, one might expect the presence of a similar destructive interference in QCD would lead to a similar formula. If this idea is right, the formula we are seeking is an extension of the eikonal formula, which can be used to sum the QCD Feynman diagrams before the actual calculations of the individual ones. The summation should include all the corresponding cancellations, after which it needs to be calculated up to leading contributions only. Indeed, this formula has been found recently, and is called the *multiple commutator formula* [31]. Using this formula, Feynman diagrams in QCD are re-organized. Unlike the case in QED where a single expression can be achieved after using eikonal formula, due to the complexity of QCD, after making use of the multiple commutator formula, the result is represented by a number of terms. For convenience, graphical representation has been invented for these terms, and they are called *nonabelian cut diagrams* [32]. The nonabelian diagram has an advantage that the delicate cancellations mentioned above have been removed, and it thus provides a powerful tool to bypass the difficulty of having to calculate up to subleading contribution of individual Feynman diagrams.

The second issue of this thesis is the factorization problem. As we pointed out above, using the eikonal formula alone, we can prove that the electron-electron scattering in QED in the high energy limit can be factorized as single-photon exchange amplitudes. Hence we can say photons are not reggeized in the high energy limit.

To prove that multi-reggeon exchange can be obtained from summing Feynman

diagrams, we need to demonstrate that the sum of QCD Feynman diagrams also possess this factorizable characteristic. However the non-abelian feature of the gluon complicates this proof. All the Feynman diagrams are related in a more complicated way due to the non-abelian feature [33]. As a result, gluons combine into reggeons at the high energy limit, and it is the single reggeon-exchange amplitude that can be factorized. All these complicate the proving of the factorization in QCD, and a complete proof by explicit computing QCD Feynman diagrams has only been done up to 6th order by Cheng and his colleagues.

To start with a simple case, we first concentrate on Feynman diagrams constructed by purely gluon-quark vertices. This is a first order approximation in the sense of assuming that each gluon does not emit or absorb any other particle when it propagates between those two energetic quarks. Using the non-abelian cut diagrams, we can prove the reggeized factorization hypothesis for this class of diagrams, which will be referred as s -channel diagrams later.

In all the discussion above, to get the s -dependence of the amplitude, we need to perform the integrations of the longitudinal momenta. This integration is done by using contour integral, as discovered by Cheng and Wu [28]. They invented a method by putting arrows on each internal line of a Feynman diagram so as to identify the pole position for each loop momentum integral. This method works well for the low order calculation, but when we deal with multi-loop diagrams, it becomes difficult to identify all the possibilities. Thus we have invented a new way

[34] to get all the poles for a multi-loop Feynman diagram. In addition, by using this new way, we can bypass a potential problem overlooked by the original method of Cheng and Wu.

To provide details for the above discussion, this thesis is organized as follows. In Chapter II, we briefly review the regge pole theory. The discussion about the BFKL pomeron is presented in Chapter III, together with its problem of unitarity violation. The unitarity problem can be solved by including multiple-Reggeon exchanges. This will be discussed in Chapter IV. The implementation of such a unitarization program requires new techniques which we will discuss in Chapter V. Using these techniques, the 6th order diagrams are recalculated in Chapter VI. In Chapter VII, we shall use the non-abelian cut diagram to prove the factorization of one special class of Feynman diagrams. Finally, Chapter VIII contains the conclusion.

Chapter II. Regge pole theory and Reggeon

As mentioned in the introduction, gluons exchanged in a scattering are reggeized at the high energy limit. According to the Regge theory[35], this Reggeon contributes a singularity to the scattering amplitude described by the corresponding Regge trajectory, and as we shall see later, this trajectory determines the s -dependence of this amplitude at the high energy limit.

To see the relation between the property of the exchange particle, the singularity and the s -dependence of the amplitude in the high energy limit, we first look at two simple examples. Consider an elastic process $A + B \rightarrow A + B$. Assume that all the particles are scalars, then the amplitude is $-g^2/t \sim s^0$ where g is the coupling constant; t is the square of the momentum transfer; s is the square of the total energy in the CM frame. Now if this is a QED process, then the coupling between electrons and photon will give an extra factor of s . Thus the amplitude is proportional to s^1 . In general, the exchange of a particle of spin- l will contribute a factor of s^l to the scattering amplitude. When more internal particles are involved, the power will get modified, and even becomes dependent on t . The resulting exponent can be regarded as an effective angular momentum, or Regge trajectory. It has the property that each trajectory can contain one or more different particles, as long as all the particles

have the same internal quantum numbers. In addition, this trajectory turns out to be the singularity of the amplitude in the complex angular momentum plane. All these are covered by the Regge Theory as reviewed briefly below.

2.1 Regge pole theory

2.1.1 Sommerfeld-Watson transformation

Consider a process $A + B \rightarrow A + B$ as shown in Fig. 3. The scattering amplitude $f(\cos \theta, E)$ can be decomposed into a Legendre series

$$f(\cos \theta, E) = \sum_{l=0}^{\infty} (2l+1) a_l(E) P_l(\cos \theta), \quad (2.1)$$

where $a_l(E)$ is usually called the *partial wave amplitude*, E is the energy, and P_l is a Legendre polynomial. If we generalize a_l and P_l into analytic functions of a complex variable l , the summation can be changed into a contour integral:

$$f(\cos \theta, E) = \frac{i}{2} \int_{C_1} \frac{(2l+1)}{\sin \pi l} a(l, E) P(l, -\cos \theta) dl. \quad (2.2)$$

The chosen contour C_1 is shown in Fig. 4. To get from equ. (2.1) to (2.2), we have made use of the following. First we have assumed that $a(l, E)$ contains only simple poles located in the complex plane away from the real axis. These poles are shown in Fig. 4 as $\alpha_i(E)$. Secondly, we have used $P(l, -\cos \theta) = (-)^l P(l, \cos \theta)$ for integer l .

We can now open up C_1 , and deform it continuously to C_2 , which runs parallel to

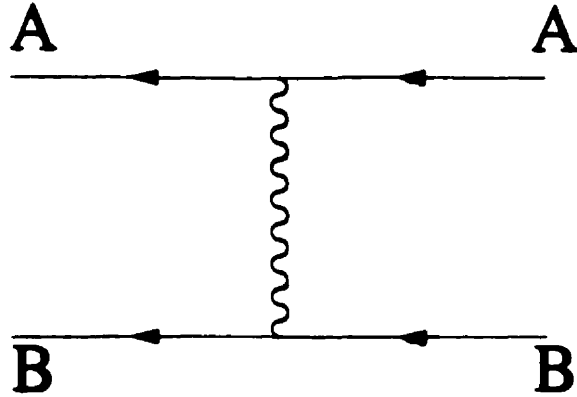


Figure 3: An elastic process $A + B \rightarrow A + B$.

the imaginary axis through the point $(-1/2, 0)$. The Regge poles can be excluded by adding loops shown as dotted circles in Fig. 4.

With suitable convergence, the integral along C_2 gives *background* terms. The dotted circles give a sum of characteristic terms, depending on the Regge poles α_i . The Regge poles are generally functions of energy, and can be written as $\alpha_i(E)$. Using this notation, we have

$$\begin{aligned}
 f(\cos \theta, E) &= i/2 \int_{-1/2-i\infty}^{-1/2+i\infty} \frac{2l+1}{\sin \pi l} a(l, E) P(l, -\cos \theta) dl \\
 &\quad - \sum_i \frac{\pi(2\alpha_i + 1)}{\sin \pi \alpha_i} \beta_i P(\alpha_i, -\cos \theta). \quad (2.3)
 \end{aligned}$$

As a function of energy, α_i is also called Regge trajectory. From equ. (2.3), we can see that $f(\cos \theta, E)$ has singularities as α_i takes on an integer value. These singularities represent resonances.

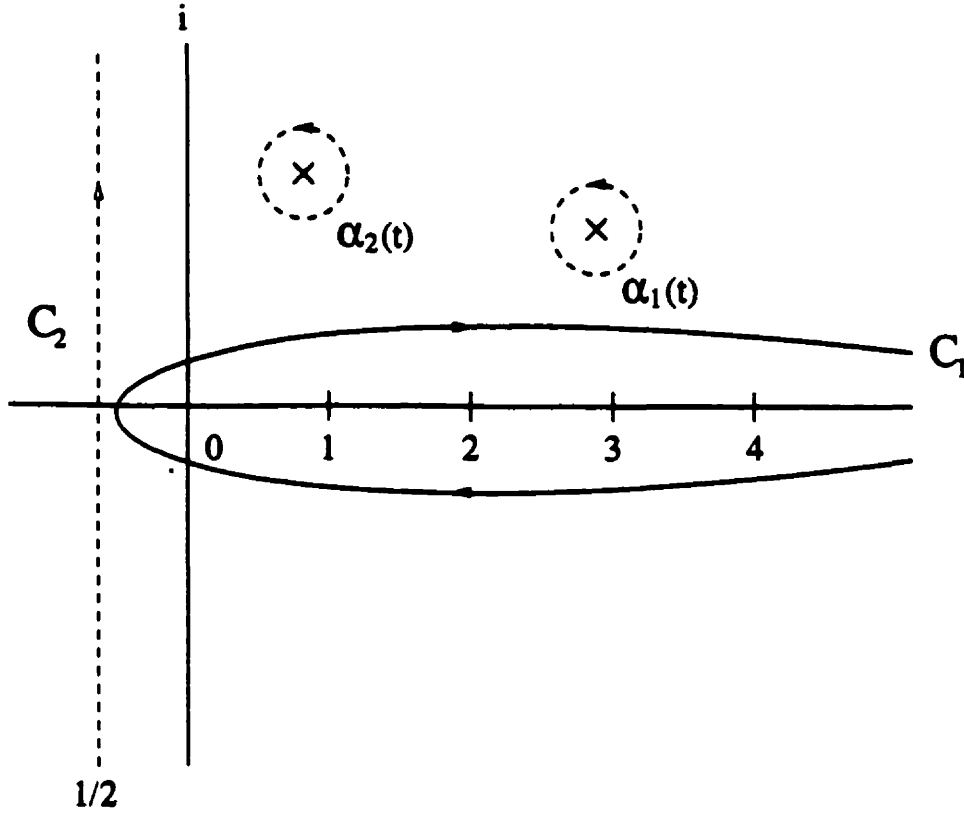


Figure 4: Contour integral.

There is a subtle point, which has been skipped before. If in the above process, particle A is its own antiparticle $A = \bar{A}$, then there is a forward- backward symmetry for the t -channel process $\bar{B} + B \rightarrow \bar{A} + A$. Thus the amplitude is $s \rightarrow u$ symmetric. This requires that in the decomposition shown in equ. (2.1) only even angular momenta l contribute, or say a_l vanishes for any odd integer l . As a result, we should first decompose the amplitude $f(\cos \theta, E)$ into its $s \rightarrow u$ symmetric/antisymmetric parts $f_{\pm}(\cos \theta, E)$:

$$f_{\pm}(\cos \theta, E) = \sum_{l=0}^{\infty} (2l+1) a_l(E) (P_l(\cos \theta) \pm P_l(-\cos \theta)), \quad (2.4)$$

and then perform the Sommerfeld-Watson transformation for them respectively. The resulting $a_l^{\pm}(E)$ in equ.(2.1) will in general have different singularities, and give two

different Regge trajectories. Signatures $+/-$ are used to identify these two different trajectories.

$$f_{\pm}(\cos \theta, E) = i/2 \int_{-1/2-i\infty}^{-1/2+i\infty} \frac{2l+1}{\sin \pi l} a(l, E) (P_l(\cos \theta) \pm P_l(-\cos \theta)) dl - \sum_i \frac{\pi(2\alpha_i+1)}{\sin \pi \alpha_i} \beta_i (P(\alpha_i, \cos \theta) \pm P(\alpha_i, -\cos \theta)). \quad (2.5)$$

2.1.2 Asymptotic behavior

Let us look at the asymptotic behavior of equ. (2.3). To simplify the discussion, we consider high energy scattering of equal-mass spinless particles. We use s and t here. s is the square of center-of-mass (cm) energy, and $-t$ is the square of cm momentum transfer. So that we have

$$\begin{aligned} s &= 4(m^2 + p_s^2), \\ t &= -2p_s^2(1 - \cos \theta_s). \end{aligned} \quad (2.6)$$

Here p and $\cos \theta$ are momentum and angle, and the subscript s is to specify s -channel. Now look at the cross channel (t -channel), t now represents the square of total energy. According to Mandelstam representation [36], a single invariant amplitude represents both the s - and t - channel processes; although their physical regions correspond to different ranges of s and t . So that we have

$$\begin{aligned} s &= 4(m^2 + p_t^2) = -2p_t^2(1 + \cos \theta_t) \\ t &= 4(m^2 + p_s^2) = -2p_s^2(1 - \cos \theta_s) \\ \cos \theta_t &= \frac{s - 2m^2 + 1/2t}{2m^2 - 1/2t}. \end{aligned} \quad (2.7)$$

Therefore, the high-energy small-angle region in the s channel corresponds, in the t channel, to an unphysical region with large $\cos \theta_t$. Under this limit, we can see that $\cos \theta_t \rightarrow s$.

Hence, by assuming that the scattering amplitude has singularities, Regge theory tells us that these singularities are determined by the particle or effective particle being exchanged between the incoming particles. In addition, after taking the high energy limit, the asymptotic behavior of the scattering amplitude has a simple form $s^{\alpha(t)}$, with s being the total energy square and $\alpha(t)$ being the trajectory.

2.2 Reggeization of gluons in QCD

Regge theory provides us a general framework about particle interactions. This framework still needs to be proven by using dynamic theory like QED or QCD. Now we look at SU(3) QCD specifically and consider the same process mentioned at the beginning of this section. The incoming particles are two quarks; the particles being exchanged are gluons. Pair-productions are neglected in this thesis as a first order approximation. The Feynman diagram shown in Fig. 5(a) is the lowest order one, in which only one gluon propagates along the t -channel. The scattering amplitude at this order is determined by the spin of the gluon. However, higher order corrections will enter as shown by the Feynman diagrams in Fig. 5(b,c,d). They all contribute to the octet color channel. In these diagrams, more than one gluon propagate along the t -channel, and the angular momentum in this channel is not fixed. As a

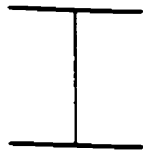
result, in general the scattering amplitude for the octet color channel is much more complicated than s to the power of the spin of the gluon.

However, in the high energy limit it turns out that a simple result can still be obtained. Using leading logarithm, it has been proven that the only change of the s dependence of the scattering amplitude is the exponent [21, 37]. Hence the scattering amplitude can be written as proportional to $s^{\alpha(t)}$. According to Regge theory, a scattering amplitude like this can be interpreted as two quarks exchanging an artificial particle carrying effective spin $\alpha(t)$. This artificial particle is called the Reggeon, or reggeised gluon. It carries the same color factor as a gluon, and its effective propagator is given by

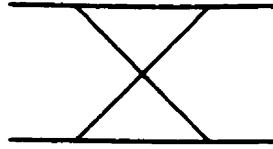
$$\frac{g^2}{\Delta^2} s^{\alpha(\Delta)} . \quad (2.8)$$

Using this Reggeon concept, the scattering amplitude can be represented by simple diagrams such as Fig. 2(a) where the solid line represents a Reggeon.

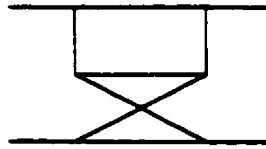
The above argument is just a special case of a more general result first shown by Fadin, Kuraev, and Lipatov [21]. According to their calculation, in an elastic scattering process $qq \rightarrow qq + ng$, under leading logarithm approximation and taking the multi-regge limit as defined in the next subsection, the final amplitude can be represented by two quarks exchanging a Reggeon which emits gluons. This result was used to construct the BFKL Pomeron as shown in the next section, but before we go to the details, we first look at the definition of rapidity and the multi-regge



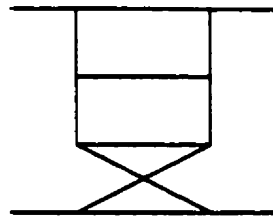
(a)



(b)



(c)



(d)

.....

Figure 5: Feynman diagrams in QCD contributing to an octet exchange.

limit which will be used throughout this thesis.

2.2.1 Rapidity and light-cone coordinate

In the high energy limit, it is convenient to use rapidity, because under one special kind of Lorentz transformation, the boost along the beam direction, the rapidity obeys an additive rule. This makes the calculations easier.

Rapidity y is defined as the following.

$$\begin{aligned} \tanh y &= \frac{p_{\parallel}}{E} = v_{\parallel} , \\ y &= \frac{1}{2} \ln \frac{E + p_{\parallel}}{E - p_{\parallel}} , \end{aligned} \quad (2.9)$$

where p_{\parallel} is the longitudinal momentum, E is the energy and y is rapidity. The first equation in equ.(2.9) tells us that longitudinal momentum and the energy scale like $\sinh y$ and $\cosh y$ respectively. From the relation between momentum and energy, we get

$$E^2 = m^2 + p^2 = m^2 + p_{\parallel}^2 + p_{\perp}^2 . \quad (2.10)$$

If we define

$$m_{\perp}^2 = m^2 + p_{\perp}^2 , \quad (2.11)$$

Then equ.(2.10) can be rewritten as

$$\left(\frac{E}{m_{\perp}} \right)^2 - \left(\frac{p_{\parallel}}{m_{\perp}} \right)^2 = 1 , \quad (2.12)$$

which gives

$$\begin{aligned} p_{\parallel} &= m_{\perp} \sinh y ; \\ E &= m_{\perp} \cosh y . \end{aligned} \quad (2.13)$$

It is often convenient to introduce light-cone coordinates too. In these coordinates the longitudinal momentum is combined with energy as follows:

$$p^{\pm} = E \pm p_{\parallel} , \quad (2.14)$$

where $p = (p^+, p^-, p_\perp)$. In this coordinate system, the metric is

$$2g_{+-} = 2g_{-+} = -g_{xx} = -g_{yy} = 1 , \quad (2.15)$$

where x and y stands for the transverse components.

The dot product of two vectors is

$$p \cdot q = (1/2)(p^+ q^- + p^- q^+) - p_\perp q_\perp . \quad (2.16)$$

Using the equ.(2.10) and equ.(2.12), the 4-momentum of a particle can be rewritten as

$$p = (p^+, p^-, p_\perp) = (m_\perp e^y, m_\perp e^{-y}; p_\perp) , \quad (2.17)$$

For massless particles the definition of rapidity in equ. (2.10), we can see that

$$\tanh y = \cos \theta , \quad (2.18)$$

where θ is the angle between the direction of the scattered particle and the beam.

Inverting this we get for the massless particle

$$y = \frac{1}{2} \ln \frac{1 + \cos \theta}{1 - \cos \theta} = -\ln \left(\tan \frac{\theta}{2} \right) . \quad (2.19)$$

For massive particles, equ. (2.19) defines the *pseudo-rapidity*, which we will denote by η . This $\eta = y$ when $m = 0$, and $\eta \sim y$ when $m \neq 0$ but the particle moving with extremely relativistic speed. Pseudo-rapidity is easy to measure experimentally, but it is the rapidity that transforms additively under boosts in the beam direction.

2.2.2 Multi-Regge limit

Let us look at an inelastic scattering in which $n+2$ particles are produced as shown in Fig.6. We choose the center-of-mass frame. The momenta of the incoming particles a and b are parameterized as:

$$\begin{aligned} p_a &= (\sqrt{s}x_A, 0; 0) , \\ p_b &= (0, \sqrt{s}x_B; 0) . \end{aligned} \quad (2.20)$$

The momenta of the outgoing particles are given by

$$k_i = (k_{i\perp}e^{y_i}, k_{i\perp}e^{-y_i}; k_{i\perp}) , \quad (2.21)$$

with $i = 0, 1, 2, 3, \dots, n+1$.

Momentum conservation can be written as

$$\begin{aligned} 0 &= \sum_{i=0}^{n+1} k_{i\perp} , \\ x_A &= \sum_{i=0}^{n+1} \frac{k_{i\perp}}{\sqrt{s}} e^{y_i} , \\ x_B &= \sum_{i=0}^{n+1} \frac{k_{i\perp}}{\sqrt{s}} e^{-y_i} . \end{aligned} \quad (2.22)$$

The Mandelstam invariants can be expressed as function of rapidity

$$\begin{aligned} \hat{s} &= x_A x_B s = \sum_{i,j=0}^{n+1} k_{i\perp} k_{j\perp} e^{y_i - y_j} \\ \hat{s}_{ai} &= -2p_a \cdot k_i = - \sum_{j=0}^{n+1} k_{i\perp} k_{j\perp} e^{-(y_i - y_j)} \\ \hat{s}_{bi} &= -2p_b \cdot k_i = - \sum_{j=0}^{n+1} k_{i\perp} k_{j\perp} e^{y_i - y_j} \\ \hat{s}_{ij} &= 2k_i \cdot k_j = 2k_{i\perp} k_{j\perp} [\cosh(y_i - y_j) - 1] . \end{aligned} \quad (2.23)$$

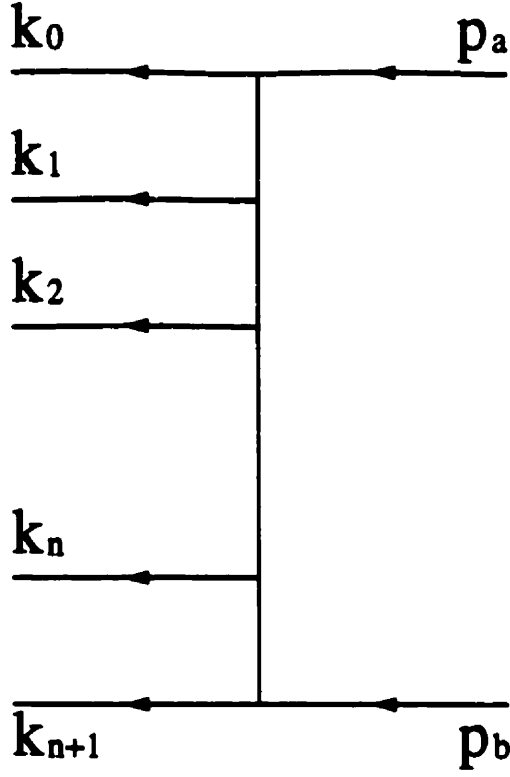


Figure 6: An inelastic scattering of gluons.

Now we look at a special region where the outgoing particles are strongly ordered in rapidity and have comparable transverse momentum of size k_{\perp} ,

$$y_0 \gg y_1 \gg \dots \gg y_{n+1} ; k_{i\perp} \simeq k_{\perp} , \quad (2.24)$$

Then the Mandelstam invariants are approximately

$$\begin{aligned} \hat{s} &\simeq k_{0\perp} k_{n+1\perp} e^{y_0 - y_{n+1}} , \\ \hat{s}_{ai} &\simeq -k_{0\perp} k_{i\perp} e^{y_0 - y_i} , \\ \hat{s}_{bi} &\simeq -k_{i\perp} k_{n+1\perp} e^{y_i - y_{n+1}} , \\ \hat{s}_{ij} &\simeq k_{i\perp} k_{j\perp} e^{|y_i - y_j|} . \end{aligned} \quad (2.25)$$

Therefore, equ.(2.23) can also be written as

$$\begin{aligned} \hat{s} &\gg \hat{s}_{ij} \gg k_{i\perp}^2, \\ \sum_{i=0}^n \hat{s}_{i,i+1} &\simeq \hat{s} \sum_{i=1}^n k_{i\perp}^2. \end{aligned} \quad (2.26)$$

This defines the *multi-Regge kinematic region*.

Chapter III. BFKL Pomeron

The BFKL Pomeron and the associated violation of unitarity will be discussed in this chapter.

As mentioned previously, Pomeron is the effective object whose exchange gives rise to the high-energy growth of total cross sections. Optical theorem relates total cross section to the diffractive part of the elastic amplitude, thus requiring the Pomeron to carry a vacuum quantum number. The question in QCD is how to construct the Pomeron in terms of gluons, and maybe quarks.

In order for it to be colorless the Pomeron must contain at least two gluons. This two-gluon picture of a Pomeron was first proposed by Low and Nussinov [8] and was the very first model of the Pomeron in QCD. Now that we know the gluon to be reggeized, the natural generalization for the Pomeron is a two-Reggeon model. Taking into account that these two Reggeons can interact through emission and absorption of gluons, what emerges is the BFKL Pomeron [10] which we shall review below.

3.1 BFKL equation

A brief review of the BFKL Pomeron will be presented in this section. Since the mathematics is a bit complicated, it might be useful first to outline the main steps

involved in getting to the final result, that the exchange of a BFKL Pomeron will produce a total cross section growing with energy like s^A , with A being a constant given in eqn. (3.32).

A BFKL Pomeron is made up of two mutually interacting Reggeons. In the original approach, the diffractive two-body amplitude is obtained from the dispersion relation (3.9), and its discontinuity (3.27) is computed from the absolute square of the n -gluon production amplitude (3.2) and (3.25). Via the dispersion relation, the t -channel partial wave amplitude can be computed, and this is used in the Sommerfeld-Watson transformation to obtain an expression for the amplitude (3.19), suitable for taking the asymptotic limit of large s and fixed t . From this expression the exponent A for the energy growth can be extracted.

We start by computing the lowest order Feynman graph for one gluon production, in the leading-log approximation. The amplitudes corresponding to Figs. 7(a), (b), (c) are respectively M_1, M_2, M_3 , and are given by

$$\begin{aligned}
 iM_1 &\simeq (g_s f^{ade_1} g_{\mu_0 \mu_0}) \frac{1}{\hat{t}_1} \\
 &\cdot (g_s f^{c_1 d_1 c_2}) (\hat{s}(q_1 + q_2)^\mu + 2\hat{s}_{b1} p_a^\mu - 2\hat{s}_{a1} p_b^\mu) \frac{1}{\hat{t}_2} \\
 &\cdot (ig_s f^{bd_2 c_2} g_{\mu_0 \mu_2}) ; \\
 iM_2 &\simeq (g_s f^{ade_1} g_{\mu_0 \mu_0}) \frac{1}{\hat{s}_{a1}} \\
 &\cdot (g_s f^{c_1 d_1 c_2}) (\hat{s} p_a^\mu) \frac{1}{\hat{t}_2} \\
 &\cdot (ig_s f^{bd_2 c_2} g_{\mu_0 \mu_2}) ;
 \end{aligned}$$

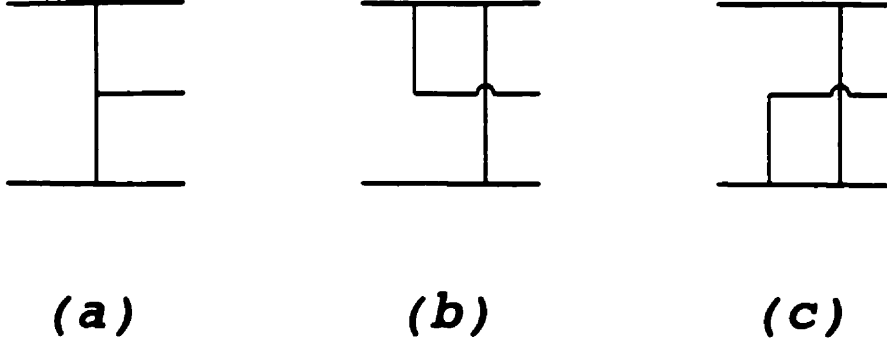


Figure 7: First order Feynman diagrams in Lipatov vertex.

$$\begin{aligned}
iM_3 &\simeq (g_s f^{ad_0 c_1} g_{\mu_0 \mu_0}) \frac{1}{\hat{t}_1} \\
&\cdot (g_s f^{c_1 d_1 c_2}) (\hat{s} p_b^\mu) \frac{1}{\hat{s}_{b1}} \\
&\cdot (ig_s f^{bd_2 c_2} g_{\mu_1 \mu_2}) ;
\end{aligned} \tag{3.1}$$

Jacobi identity has been used to decompose the color factor of Figs. 7(b) and 7(c).

Now we can simplify the sum of these three terms as

$$\begin{aligned}
iM &= iM_1 + iM_2 + iM_3 \\
&\simeq 2i\hat{s} (ig_s f^{ad_0 c_1} g_{\mu_0 \mu_0}) \frac{1}{\hat{t}_1} \\
&\cdot (ig_s f^{c_1 d_1 c_2} \Gamma^{\mu_1}(q_1, q_2)) \frac{1}{\hat{t}_2} \\
&\cdot (ig_s f^{bd_2 c_2} g_{\mu_1 \mu_2}) ,
\end{aligned} \tag{3.2}$$

where the Lipatov vertex can be expressed as

$$\Gamma^\mu(q_1, q_2) \simeq \left[(q_1 + q_2)_1^\mu - \left(\frac{\hat{s}_{a1}}{\hat{s}} + 2 \frac{\hat{t}_2}{\hat{s}_{b1}} \right) p_b^\mu + \left(\frac{\hat{s}_{b1}}{\hat{s}} + 2 \frac{\hat{t}_1}{\hat{s}_{a1}} \right) p_b^\mu \right] . \tag{3.3}$$

It can be proven that this vertex is gauge invariant because

$$\Gamma^\mu(q_1, q_2)(q_1 - q_2)_\mu = 0 . \quad (3.4)$$

It has been shown by Dickinson [37] that the higher order correction for the same process in the same color channel effectively reggeizes the gluons in the t -channel. Therefore the amplitude containing all the corrections can be obtained from equ. (3.2) above by changing the gluon propagators into the Reggeon propagator

$$\frac{1}{\hat{t}_i} \rightarrow \frac{1}{\hat{t}_i} e^{\alpha(t_i)(w_i - w)} , \quad (3.5)$$

where $\alpha(t_i)$ is the Regge trajectory given by

$$\alpha(t_i) = \alpha_s N_c \hat{t}_i \int \frac{d^2 k_\perp}{(2\pi)^2} \frac{1}{k_\perp^2 (q - k)_\perp^2} . \quad (3.6)$$

Lipatov proved that for a general n , the amplitude has a similar structure as equ. (3.2). The only thing we need is to add in more reggeized gluon propagators and more Lipatov vertices [10, 21]. In this way, we get the n -gluon amplitude to be

$$\begin{aligned} iM_{\mu_0 \mu_1 \mu_2 \dots \mu_{n+1}}^{ab d_0 d_1 \dots d_{n+1}} &\simeq 2i\hat{s} \left(i g_s f^{ad_0 c_1} g_{\mu_0 \mu_2} \right) \frac{1}{\hat{t}_1} e^{\alpha(\hat{t}_1)(w_0 - w_1)} \\ &\cdot \left(i g_s f^{c_1 d_1 c_2} \Gamma^{\mu_1}(k_1, k_2) \right) \left(\frac{1}{\hat{t}_2} e^{\alpha(\hat{t}_2)(w_1 - w_2)} \right) \\ &\cdot \dots \\ &\cdot \dots \\ &\cdot \left(i g_s f^{c_n d_n c_{n+1}} \Gamma^{\mu_n}(k_n, k_{n+1}) \right) \left(\frac{1}{\hat{t}_{n+1}} e^{\alpha(\hat{t}_{n+1})(w_n - w_{n+1})} \right) \\ &\cdot \left(i g_s f^{bd_{n+1} c_{n+1}} g_{\mu_n \mu_{n+1}} \right) . \end{aligned} \quad (3.7)$$

According to Lipatov's method, the elastic amplitude is evaluated by using the dispersion relation. The amplitude as a function of \hat{s} has two branch cuts over the real axis of complex \hat{s} plane, $-\hat{t} \leq \hat{s} < \infty$ and $-\infty < \hat{s} \leq 0$, hence we can write a Cauchy integral for an general scalar amplitude $A(\hat{s}, \hat{t})$ to be

$$A(\hat{s}, \hat{t}) = \int_{-\infty}^0 \frac{ds' \text{Disc}A(s', \hat{t})}{2\pi i (s' - \hat{s})} + \int_{-\hat{t}}^{\infty} \frac{ds' \text{Disc}A(s', \hat{t})}{2\pi i (s' - \hat{s})}, \quad (3.8)$$

where the discontinuity of the amplitude is defined as

$$\text{Disc}A(s', \hat{t}) = A(s' + i\epsilon, \hat{t}) - A(s' - i\epsilon, \hat{t}). \quad (3.9)$$

Since we have

$$z_t = - \left(1 + \frac{2\hat{s}}{\hat{t}} \right), \quad (3.10)$$

the dispersion relation can also be written as an integral over the complex plane of z_t as

$$A(\hat{s}, \hat{t}) = \int_{-\infty}^{-1} \frac{dz'_t \text{Disc}A(z'_t, \hat{t})}{2\pi i (z'_t - z_t)} + \int_1^{\infty} \frac{dz'_t \text{Disc}A(z'_t, \hat{t})}{2\pi i (z'_t - z_t)}. \quad (3.11)$$

In the physical region $-1 \leq z_t \leq 1$, the t -channel amplitude can be used to project out the partial wave:

$$A_l(\hat{s}, \hat{t}) = \frac{1}{2} \int_{-1}^1 dz_t P_l(z_t) A(\hat{s}, \hat{t}). \quad (3.12)$$

Using the associated Legendre function defined by

$$Q_l(z') = \frac{1}{2} \int_{-1}^1 \frac{dz'' P_l(z'')}{z' - z''}, \quad (3.13)$$

we can substitute the dispersion relation equ. (3.11) into the partial wave amplitude equ. (3.12). Using the identity [38]

$$\begin{aligned} Q_l(-z) &= (-1)^{l+1} Q_l(z), \\ \text{Disc}A(-z, t) &= -\text{Disc}A(z, t) \end{aligned} \quad (3.14)$$

the l th partial wave amplitude becomes

$$A_l(\hat{s}, \hat{t}) = [1 + (-1)^l] \int_1^\infty \frac{dz'}{2\pi i} Q_l(z') \text{Disc}A(z', \hat{t}). \quad (3.15)$$

Now we introduce the Sommerfeld-Watson representation of the amplitude $A(\hat{s}, \hat{t})$ in the complex plane of the angular momentum l as discussed in Chapter II,

$$A(\hat{s}, \hat{t}) = \int_{C_1} \frac{dl}{2i} (2l+1) A_l(\hat{s}, \hat{t}) \frac{P_l(-z_t)}{\sin \pi l}. \quad (3.16)$$

The path C_1 is the same as we used in Sec II. Under the high energy limit: $\hat{s} \rightarrow \infty$ at fixed \hat{t} , we have

$$\begin{aligned} z_t &\rightarrow -\frac{2\hat{s}}{\hat{t}}, \\ P_l(z) &\rightarrow (2z)^l, \\ Q_l(z) &\rightarrow (z)^{-l-1}, \end{aligned} \quad (3.17)$$

the partial wave amplitude in equ. (3.16) can be rewritten as

$$A(\hat{s}, \hat{t}) = -\frac{1}{4\pi} \int_{C_1} dl \frac{(-1)^l + 1}{\sin \pi l} e^{l\nu} F_l(\hat{t}), \quad (3.18)$$

where $F_l(\hat{t})$ is the Laplace transform of the discontinuity of the amplitude

$$F_l(\hat{t}) = \int_0^\infty dy' e^{-l\nu'} \text{Disc}A(z_t, \hat{t}), \quad (3.19)$$

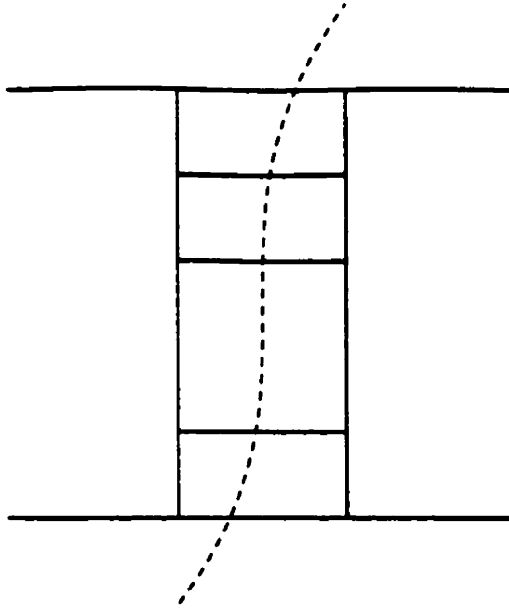


Figure 8: One of the diagrams contributing to BFKL Pomeron.

with

$$y' = \ln(z'_i/2) , \quad y = \ln(z_i/2) . \quad (3.20)$$

It is shown in equ. (3.19), to calculate an elastic amplitude, we need to calculate the discontinuity of the amplitude. To that end, we need to sum over all Cutkosky cut diagrams like Fig. 8 for all n , with intermediate gluon lines cut. This is accomplished by replacing the Feynman propagator with the Cutkosky propagator,

$$\frac{i}{k_i^2} \rightarrow 2\pi\delta(k_i^2) , \quad (3.21)$$

which has the effect of putting all the cut lines on mass shell

$$k_i^2 = 0 . \quad (3.22)$$

With the kinematical factor

$$\prod_{i=0}^n \int \frac{d^4 k_i}{(2\pi)^4} \prod_{j=0}^{n+1} 2\pi\delta(k_j^2) = \prod_{i=0}^{n+1} \int \frac{dy_i d^2 k_{i\perp}}{4\pi(2\pi)^2} (2\pi)^4 \delta^4(p_a - p_b - \sum_{i=0}^{n+1} k_i)$$

$$= \int \frac{1}{2\hat{s}} d^2 k_{0\perp} (2\pi)^2 \left(\prod_{i=1}^n \frac{dy_i d^2 k_{i\perp}}{4\pi(2\pi)^2} \right) \frac{d^2 k_{n+1\perp}}{(2\pi)^2} (2\pi)^2 \delta^2 \left(\sum_{i=0}^{n+1} k_{i\perp} \right), \quad (3.23)$$

the discontinuity of the amplitude in Fig. 8, with n summed from $0 \rightarrow \infty$ becomes

$$\begin{aligned} \text{Disc}[iM_{\mu_a \mu_b \mu_c \mu_d}^{abab'}(\hat{s}, \hat{t})] = & \\ & \sum_{n=0}^{\infty} \int \frac{1}{2\hat{s}} d^2 k_{0\perp} (2\pi)^2 \left(\prod_{i=1}^n \frac{dy_i d^2 k_{i\perp}}{4\pi(2\pi)^2} \right) \frac{d^2 k_{n+1\perp}}{(2\pi)^2} (2\pi)^2 \delta^2 \left(\sum_{i=0}^{n+1} k_{i\perp} \right) \\ & \cdot (2i\hat{s})^2 \delta_{\perp}^{\mu_a \mu_c'} \delta_{\perp}^{\mu_b \mu_d'} (ig_s f^{d_0 c_1}) (ig_s f^{c'_1 d_0 a'}) \\ & \cdot \frac{1}{\hat{t}'_1} e^{\alpha(i_1)(y_n - y_1)} \frac{1}{\hat{t}'_1} e^{\alpha(i'_1)(y_n - y_1)} \\ & \cdot (ig_s f^{c_1 d_1 c'_2}) (ig_s f^{c'_2 d_1 c'_2}) \Gamma^{\mu_1}(q_1, q_2) (-g_{\mu_1 \mu'_1}) \Gamma^{\mu'_1}(q - q_1, q - q_2) \\ & \cdot \frac{1}{\hat{t}'_2} e^{\alpha(i_2)(y_1 - y_n)} \frac{1}{\hat{t}'_2} e^{\alpha(i'_2)(y_1 - y_n)} \\ & \cdot \dots \\ & \cdot (ig_s f^{c_n d_n c_{n+1}}) (ig_s f^{c'_{n+1} d_n c'_{n+1}}) \Gamma^{\mu_n}(q_n, q_{n+1}) (-g_{\mu_n \mu'_n}) \Gamma^{\mu'_n}(q - q_n, q - q_{n+1}) \\ & \cdot \frac{1}{\hat{t}'_{n+1}} e^{\alpha(i_{n+1})(y_n - y_{n+1})} \frac{1}{\hat{t}'_{n+1}} e^{\alpha(i'_{n+1})(y_n - y_{n+1})} \\ & \cdot (ig_s f^{b_{n+1} c_{n+1}}) (ig_s f^{c'_{n+1} d_{n+1} b'}), \end{aligned} \quad (3.24)$$

where $\hat{t} = q^2$ is the momentum transfer and $\hat{t}'_i = (q - q_i)^2$. The contraction of two

Lipatov vertices is

$$\Gamma^{\mu}(q_i, q_{i+1}) \Gamma_{\mu}(q - q_i, q - q_{i+1}) = 2 \left(q_{\perp}^2 - \frac{(q - q_i)_{\perp}^2 + (q - q_{i+1})_{\perp}^2}{(q_{i\perp} - q_{i+1\perp})^2} \right). \quad (3.25)$$

Now we need to decompose equ. (3.24) into singlet and octet contributions. It can be checked that the octet contribution just gives the reggeized gluon exchange,

which provides a self-consistency check. But we are more interested in the singlet exchange, which is identified as the BFKL pomeron. After we change the integration variables from k_i to q_i using the conservation of the transverse momentum, the singlet part $A(\hat{s}, \hat{t})$ can be written in a compact form

$$\begin{aligned} DiscA(\hat{s}, \hat{t}) &= \sum_{n=0}^{\infty} (-g_s^2 N_c)^{n+2} \int \prod_{i=1}^n \frac{dy_i}{4\pi} \prod_{j=1}^{n+1} \frac{d^2 q_{j\perp}}{(2\pi)^2} \\ &\cdot 2i\hat{s} \prod_{i=1}^{n+1} \frac{1}{\hat{t}_i \hat{t}'_i e^{(n-1-u)[\alpha(\hat{t}_i) + \alpha(\hat{t}'_i)]} \prod_{m=1}^n 2K(q_m, q_{m+1})}, \quad (3.26) \end{aligned}$$

We can perform the integral of the rapidity. First we introduce a Laplace transformation to the left hand side of the above equation. And then we change the integration variables to be the rapidity differences. The integral over y_i can be performed easily and we get

$$\begin{aligned} F_l(\hat{t}) &\equiv \int_0^{\infty} dy e^{-ly} DiscA(\hat{s}, \hat{t}) \\ &= -2i\hat{t}(4\pi\alpha_s)^2 N_c^2 \sum_{n=0}^{\infty} \int \prod_{j=1}^{n+1} \\ &\cdot \frac{1}{\hat{t}_1 \hat{t}'_1 l - 1 - \alpha(\hat{t}_1 - \hat{t}'_1)} \\ &\cdot (-2\alpha_s N_c) K(q_1, q_2) \\ &\cdot \frac{1}{\hat{t}_2 \hat{t}'_2 l - 1 - \alpha(\hat{t}_2 - \hat{t}'_2)} \\ &\cdot \\ &\cdot \\ &\cdot (-2\alpha_s N_c) K(q_n, q_{n+1}) \\ &\cdot \frac{1}{\hat{t}_{n+1} \hat{t}'_{n+1} l - 1 - \alpha(\hat{t}_{n+1} - \hat{t}'_{n+1})} \quad (3.27) \end{aligned}$$

If we define a function $f_l(q_1, \hat{t})$ satisfying the following recursive relation

$$f_l(q_1, \hat{t}) = \frac{1}{l-1-\alpha(\hat{t}_1)-\alpha(\hat{t}'_1)} (1-2\alpha_s N_c) \int \frac{d^2 q_{2\perp}}{(2\pi)^2} \frac{K(q_1, q_2)}{q_{2\perp}^2 (q-q_2)_\perp^2} f_l(q_2, \hat{t}), \quad (3.28)$$

Then we can see $F_l(\hat{t})$ is related to this function as

$$F_l(\hat{t}) = -2i\hat{t}(4\pi\alpha_s)^2 N_c^2 \int \frac{d^2 q_{1\perp}}{(2\pi)^2} \frac{1}{q_{1\perp}(q-q_1)_\perp^2} f_l(q_1, \hat{t}). \quad (3.29)$$

The above recursive relation is the BFKL equation.

After discussion of the cancellation of the infra and ultraviolet divergences, the Pomeron solution can be found as

$$f_l(k_a, k_b) \simeq \frac{1}{(2\pi)^2} \frac{1}{(k_{a\perp}^2 k_{b\perp}^2)^{1/2}} \frac{\pi}{[B(l-1-A)]^{1/2}} e^{-\nu_0 |\ln(k_{a\perp}^2/k_{b\perp}^2)|}. \quad (3.30)$$

with

$$A = 4 \ln 2 \frac{\alpha_s N_c}{\pi}; \quad B = 14\eta(3) \frac{\alpha_s N_c}{\pi}; \quad \nu_0 = \left(\frac{l-1-A}{B} \right)^2. \quad (3.31)$$

This will give a total cross section

$$\sigma_{tot} = s^A. \quad (3.32)$$

3.2 Unitarity problem of the BFKL pomeron

As we can see from the derivation above the total cross section is proportional to s^A , with $A = 4 \ln 2 \frac{\alpha_s N_c}{\pi}$. In SU(3) QCD, $N_c = 3$. For a coupling constant $\alpha_s = 0.2$, we get $A = 1.53$.

Since $A > 1$, the total cross section obtained from BFKL pomeron violate the Froissart bound, and thus violates the unitarity condition. The reason for this violation is because only two-reggeon exchange amplitudes are included in the BFKL Pomeron. For unitarity to be satisfied, an infinite number of Reggeon exchanges is required. We shall discuss that in the next Chapter.

Chapter 4. Multi-Reggeon exchanges

As we can see in the above section, the BFKL Pomeron is computed from two-Reggeon-exchange amplitude, which is actually dominant in the leading-log approximation as described in the introduction of this thesis. As we will see later, the multi-Reggeon exchange amplitudes shown in Fig. 9(c,d,f,g..) are of the order of $(g^2)^n s (g^2 \ln^2 s)$, with n being the number of Reggeons. Hence for a fixed order of the coupling constant g , the multi-Reggeon exchange amplitudes possess lower powers of $\ln s$, and can be excluded in the leading logarithm approximation. On the other hand, the unitarity condition generates higher multi-Reggeon amplitudes from the two-Reggeon amplitude, and the absence of them can lead to the violation of unitarity at asymptotic limit. To restore unitarity, one therefore needs to go beyond the leading-log approximation to include all multi-Reggeon exchange amplitudes.

Before we start the calculation in QCD, it is worthwhile at this point to review the calculation of electron-electron elastic scattering in QED in the high energy limit. It shares many similarities with the quark-quark elastic scattering at hand, and hopefully it can give us some guidance. Consequently, in the following section, we shall review the QED calculation first, and then discuss how to generalize the idea to QCD calculations, where the real difficulties are.

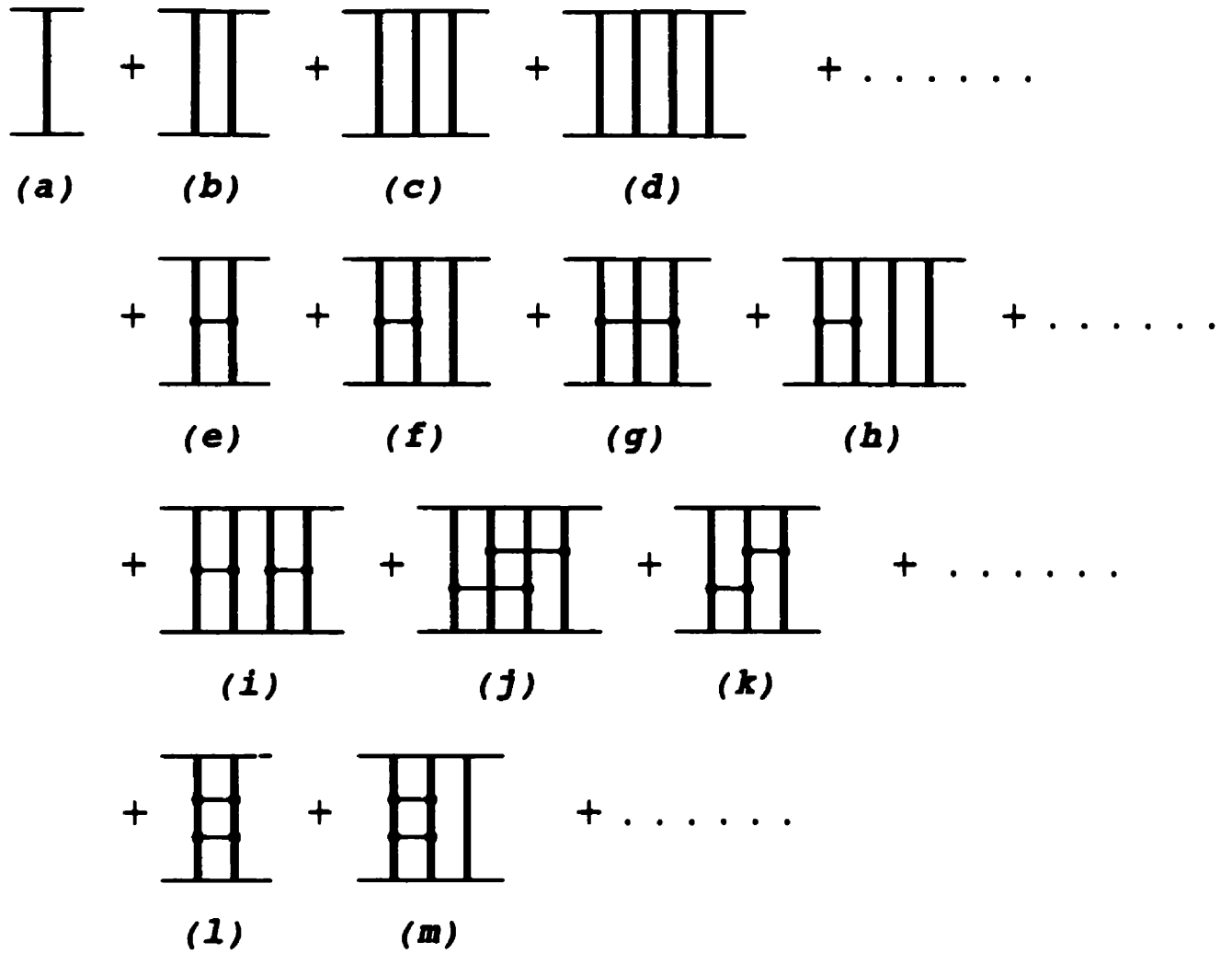


Figure 9: Multi-reggeon exchange diagrams in QCD.

4.1 QED eikonal formula

Here we focus on $e + e \rightarrow e + e$ elastic scattering. It has been known that the high energy forward scattering in QED has the following property [28]:

1. The energy dependence is the result of creation of e^+e^- in the intermediate state. It is of order of $(e^4)(e^4 \ln s)$ and is imaginary.
2. The sum of these leading terms gives a total cross section $\sigma_{tot} = s^J$, with $J = 1 + \frac{11\alpha^2\pi}{32}$. This violates the Froissart bound[17].
3. The photon remains elementary, not reggeized.
4. After including the multi-photon exchange, the final result is unitary.

The problem of unitarity violation shown in point 2 for electron-electron elastic scattering in QED is similar to the problem encountered in quark-quark scattering. To restore unitarity, we need to add in multi-photon exchange. For simplicity, to illustrate this point, we are going to focus in this thesis on the simplest case by ignoring pair production. In this case, according to the point 1) above, we shall reproduce a total cross section that is independent of energy. What we need to calculate is all the possible Feynman diagrams with N -photon exchanged in the t channel, and then sum N from 0 to ∞ . This is shown in Fig. 10 for diagrams up to 6th order. It turns out that all these diagrams can be summed into a compact form by using the eikonal formula and the resulting cut diagrams. These two techniques

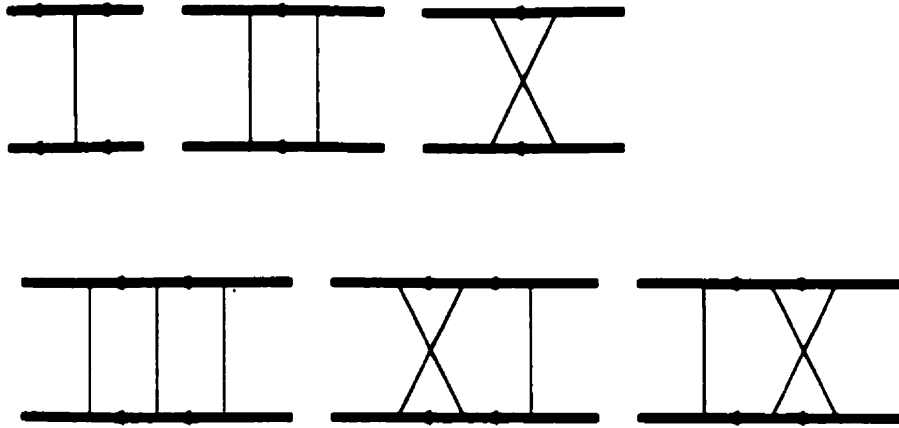


Figure 10: QED diagrams for $ee \rightarrow ee$. Here solid lines are used to denote fermion, and the thin lines are used for photons.

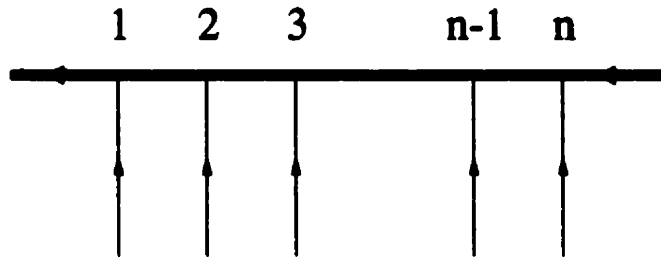


Figure 11: A tree level Feynman diagram in QED.

will be later generalized to QCD.

4.1.1 eikonal formula for QED

We look at a tree diagram as shown in Fig. 11. First we use a number to label each external photon line as shown in the picture. We then use a convention $a[12 \cdots n]$ to denote the amplitude of this tree $[12 \cdots n]$, where the ordering inside the square bracket is the same as the ordering of the external photon lines along the fermion

line. Let $[T_1 T_2 \cdots T_N]$ denote the tree by merging all these $[T_i]$ trees together. Another useful notation is $\{T_1; T_2; \cdots; T_N\}$, which is used to denote the sum of all tree diagrams obtained by *interleaving* the trees T_1, T_2, \cdots, T_A in all possible ways. For example if $T_1 = [123]$, $T_2 = [45]$, Then $[T_1 T_2] = [12345]$, and $\{T_1; T_2\}$ contain the following 10 trees: $[12345]$, $[12435]$, $[12453]$, $[14235]$, $[14253]$, $[14523]$, $[41235]$, $[41253]$, $[41523]$, and $[45123]$. We also use $a\{T_1; T_2; \cdots; T_N\}$ to denote the sum of all the amplitudes $a[T]$ for every tree T in the set of $\{T_1; T_2; \cdots; T_N\}$.

Consider the limit where the momentum p carried by the fermion line is much larger than the momentum k_i carried by the i th photon line, we can rewrite the denominator of a fermion propagator as

$$(p + \sum_{j=1}^i k_j)^2 - m^2 + i\epsilon \simeq 2p \cdot \prod_{j=1}^i k_j + i\epsilon, \quad (4.1)$$

Using the notation above, the amplitude of the tree diagram in Fig. 11 can be written as

$$a[12 \cdots n] = -2\pi i \delta(\sum_{j=1}^n k_j) \left(\sum_{i=1}^{n-1} \frac{1}{\sum_{j=1}^i p \cdot k_j + i\epsilon} \right) C. \quad (4.2)$$

where C contains all the QED factors. To get equ. (4.2), we have used high energy approximation. (See App. B for normalization we choose.)

It has been found in [31] that under this high energy approximation, the amplitude $a\{T_1; T_2; \cdots; T_N\}$ can be factorized as follows:

$$a\{T_1; T_2; \cdots; T_N\} = \prod_{i=1}^N a[T_i]. \quad (4.3)$$

This can be proven as follows. Consider $[T] = [t_1 t_2 \cdots t_n]$, then $a[T]$ is its amplitude

$$a[T] = (-i)^n \int_{-\infty}^{\infty} d\tau_{t_n} \int_{-\tau_{t_n}}^{\infty} d\tau_{t_{n-1}} \int_{-\tau_{t_{n-1}}}^{\infty} \cdots \int_{\tau_{t_2}}^{\infty} d\tau_{t_1} \exp\left(i \sum_{i=1}^n \omega_{t_i} \tau_{t_i}\right). \quad (4.4)$$

Performing the integral of τ_i we can get back to an expression similar to equ. (4.3).

Note that the integration variables are all in the order $\infty \geq \tau_{t_1} \geq \tau_{t_2} \geq \cdots \geq \tau_{t_n}$.

When we sum over all the trees belonging to $\{t_1; t_2; \cdots; t_n\}$, the integration variables

τ_{t_i} retains the ordering only within each individual tree T_i , and for each tree they

integrate from $-\infty$ to $+\infty$. Therefore, it is just the product of the amplitudes

of the corresponding trees. This factorization formula is similar to the string-like

representation in Ref.[39]. It remains valid when the photon lines are off-shell.

This factorization can be exhibited graphically by putting a *cut* (a vertical bar) in

every propagator between trees T_i and T_{i+1} , thereby changing the Feynman tree

diagram $[T_1 T_2 \cdots T_N]$ into a *cut diagram* $[T_1 | T_2 | \cdots | T_N]$. By definition, the cut turns

a Feynman propagator with factor $1/[(p+K)^2 - m^2 + i\epsilon] \simeq 1/[2p \cdot K + i\epsilon]$ into

a Cutkosky propagator with factor $-2\pi i \delta[(p+K)^2] \simeq -2\pi i \delta[2p \cdot K]$. With the

definition of $a[T_i]$ given in (4.2), it is now obvious that (4.3) can be written as

$a\{T_1; T_2; \cdots; T_N\} = \prod_{i=1}^N a[T_i] = a[T_1 | T_2 | \cdots | T_N]$. In short, a semi-colon ";" can

be replaced by a vertical bar "|", and both can be interpreted as a symbol for the

factorization of the amplitude.

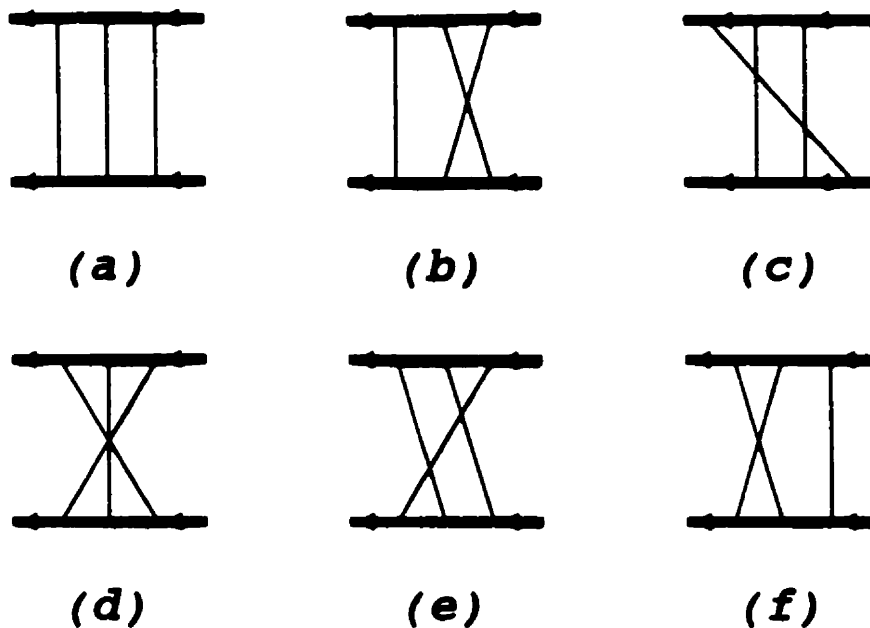


Figure 12: 6th order Feynman diagrams in QED.

4.1.2 Cut diagram in QED

We shall discuss in this section QED electron-electron elastic scattering in the high energy limit. We first look at the 6th order calculation, then we give a general argument for higher order calculations.

All six Feynman diagrams at the 6th order are shown in Fig. 12(a)-12(f). If we label the bottom of the photon lines according to the ordering they are joined to the bottom fermion line, the $n! = 3! = 6$ diagrams are related by the permutation of the upper ends of the photon lines. Using equ. (4.2) and (4.3), we can apply the factorization formula above to the top line, and cut all the fermionic propagators on it. In general, for $(2n)$ th order, there are $n!$ Feynman diagrams, and every fermion

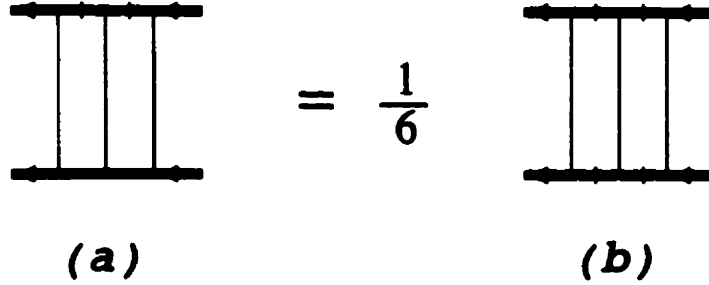


Figure 13: A relation between QED cut diagrams.

propagator on the top fermion line can be cut as well. This is shown in Fig. 13(a) for $n = 3$. Since putting a cut on a line is effectively making it on-shell, the n photon lines joined to the top fermion line can be permuted at will. As a result, further permutation of these photon lines along the bottom fermion line will not change anything. If we sum up all the $n!$ permutations of these n photon lines, we can use the factorization formula again and introduce a cut to all the fermion propagators on the bottom line as well. Thus we can get the identity shown in Fig. 13.

To perform the loop momenta integrals, we use the light-cone coordinate we introduced before. The loop momentum integral for each independent loop can be written as

$$i \frac{1}{(2\pi)^4} d^4 q = \frac{1}{8\pi^2} dq^- dq^+ \frac{1}{(2\pi)^2} d^2 q_\perp . \quad (4.5)$$

We will choose the $n - 1$ smallest loops to be the independent loops. For each of the loops we choose, there are two on-shell δ -functions, one on the top line, the other

on the bottom line. These two δ -functions will get rid of the q^+ and q^- integrals, and leaving behind only the transverse momentum integrals. For $(2n)$ th order, this amplitude is simply

$$\frac{T_n}{2s} = -\frac{g^{2n}}{n!} (-i)^{n-1} \int \left(\prod_{i=1}^n \frac{d^2 q_{i\perp}}{(2\pi)^2 q_{i\perp}^2} \right) (2\pi)^2 \delta\left(\sum_{i=1}^n q_{i\perp} - \Delta\right) \equiv -\frac{g^{2n}}{n!} (-i)^{n-1} I_n(\Delta) \quad (4.6)$$

where Δ is the momentum transfer. We can see that the function $I_n(\Delta)$ is the n th-power convolution of I_1 with itself. Thus if we perform a Fourier transformation and change it into the impact-parameter-space, it will become a simple product:

$$\bar{I}_n(b) = [\bar{I}_1(b)]^n . \quad (4.7)$$

Thus the $(2n)$ th order of the T -matrix in the impact-parameter-space can be given by

$$\frac{\bar{T}_n(b)}{2s} = -i \frac{1}{n!} [-ig^2 \bar{I}_1(b)]^n . \quad (4.8)$$

It can then be summed up for n from 1 to ∞ to get

$$\sum_{n=1}^{\infty} \frac{\bar{T}_n(b)}{2s} = -i \sum_{n=1}^{\infty} \frac{[-ig^2 \bar{I}_1(b)]^n}{n!} = -i \exp(-ig^2 \bar{I}_1(b)) - 1 . \quad (4.9)$$

To get back to the momentum space, we carry out the inverse Fourier transform.

This yields

$$\frac{T}{2s} = -i \int d^2 b e^{iq_{\perp} \cdot b} \left(\exp[-ig^2 \bar{I}_1(b)] - 1 \right) , \quad (4.10)$$

which is called the *eikonal formula*. The amplitude given by this formula is unitary.

Note that it is important to include the contribution of multi-photons to obtain unitarity.

There is no s dependence on the right-hand side of (4.10). It is important to realize that this is *not* the case for individual Feynman diagrams, which may contain (even high) powers of $\ln s$. When Feynman diagrams are summed and the factorization formula (4.3) is used, these $\ln s$ powers all get cancelled to yield (4.10). This is because the Born amplitude with one-photon exchange is s independent, so if the multi-photon amplitude is factorized into product of one-photon amplitudes, it must be s independent as well. Something similar also happens in QCD, so it is important to understand in a more general way how factorization (4.3) is related to cancellation of $\ln s$ factors.

As noted before, factorization is equivalent to replacing certain Feynman propagators $1/(2p \cdot K + i\epsilon) \equiv 1/(x + i\epsilon)$ by the Cutkosky propagators $-2\pi i \delta(2p \cdot K) = -2\pi i \delta(x)$. If a $\ln s$ factor arises from the original Feynman diagram in a loop containing this propagator, it comes from integrals of the form $\int dx/(x + i\epsilon) \sim \ln s$, in which the lower limit of integration is proportional to $1/s$. In the corresponding cut diagram where $1/(x + i\epsilon)$ is replaced by $\sim \delta(x)$, the integral is convergent, thus losing the $\ln s$ factor.

4.2 Generalization to QCD and related difficulties

Now let us look at quark-quark elastic scattering in QCD. Its non-abelian nature prevents simple factorization to occur as in the case of QED. However, it is known from leading-log calculations [40] that gluons are reggeized at high energy though

photons are not. So one might think that gluons should be replaced by Reggeons before factorization can take place. This turns out to be the case as we shall discuss in the next Chapter.

The factorization of Reggeons also gets rid of some of the $\ln s$ dependence of the corresponding loop, as discussed at the end of the last section. This can help us estimate the $\ln s$ dependence of the final amplitude. As pointed out before, a Reggeon is made up of numerous gluons. In general, in an n -Reggeon exchange amplitude, $n - 1$ factors of $\ln s$ are removed by factorization, so this gives us a power of $\ln s$ as bounded by

$$(g^2)^n (g^2 \ln s)^m . \quad (4.11)$$

In principle, equ. (4.11) tells us that we need to calculate diagrams up to this subleading order, in order to prove that summing Feynman diagrams can yield a multi-reggeon exchange amplitude. Direct calculations were carried out to the sixth order [28], which shows that such multiple Reggeons are indeed present. However, direct calculations to the 8th and 10th orders encountered intrinsic difficulties unable to be overcome with the usual techniques, so now twenty years later, we are still searching for the complete proof of the emergence of multi-Reggeons from summing Feynman diagrams. We shall make some progress in this thesis using a new technique to be discussed in the next Chapter.

Technically, there are the following difficulties to be overcome:

1. The calculations in Non-Abelian theories are more difficult than those in QED, because the vertex of interaction in Yang-Mills theories[30] are more complicated. As one of the results, QCD involves many more Feynman diagrams compared to the same order calculation of QED. It was reported that for the 8th order calculation, thousands of diagrams have to be included in the computation. And the situation gets even worse when higher order calculations are under consideration.
2. The Yang-Mills vector meson, here the gluon, carries color and may emit other vector mesons. This contrasts with the situation in QED, where the photon is chargeless and cannot emit other photons. It makes the Feynman diagrams in QCD more complicated. When we integrate the longitudinal components of each loop momentum, we will encounter a multi-dimensional integral.
3. The high energy amplitude due to the exchange of gauge bosons is always proportional to s times a power of $\ln s$. For most Feynman diagrams, this power exceeds two. Thus the contribution to the scattering amplitude from individual Feynman diagram always violates the unitary bound $s \ln^2 s$. Since the sum of all these Feynman diagrams must satisfy the unitarity condition, extensive cancellations must occur in the summation. According to equ. (4.11), contribution of powers of $\ln s$ larger than m will be cancelled in the sum. Consequently beyond the leading logarithm approximation, which is usually

an impossible task. We will discuss a method in Chapter 5 whereby this unpleasant cancellation can be avoided.

4. On account of the presence of non-commuting color matrices, QCD amplitudes do not factorize as simply as the QED amplitudes, and QCD s -channel diagrams like Fig. 12 cannot be summed up to be a single diagram displayed in Fig. 13, where no $\ln s$ factors appear. The upshot is that there are many more non-trivial $\ln s$ dependences to compute in QCD. To compute them we follow the technique in the book of Cheng and Wu [28] where lightcone coordinates are used for loop integrations. If k_a is the loop momentum of the a th loop, the integration over k_{a+} is done exactly using residue calculus. To carry out this integration it is necessary to know which of the poles lie in the upper k_{a+} plane and which lie in the lower plane, as only poles in one half plane contributes to the integral. For that purpose Cheng and Wu invented *flow diagrams*, which can be regarded as a graphical way to keep track of the location of these poles. For one loop this method works beautifully, but as the number of loops increases the straight-forward application of this method becomes not only difficult, but sometimes even problematical. We shall discuss in Sec. 5.1 the problems encountered with this method and a new *path method* to solve the difficulties.
5. As we found in the above calculations of QED, the final result contains two

parts: s and $\ln s$ to a certain power, and the coefficient of the transverse momentum integrals. In QCD, the transverse momentum integral for certain Feynman diagrams is divergent. According to the 6th order calculations [28], part of this divergence contribution comes from infra divergence, and can be renormalized by introducing mass to the gluons [41]. The rest gets cancelled when we sum up the corresponding Feynman diagrams. The cancellation part is complicated for higher order calculation, as a result, for the published 8th and 10th order calculations [24, 45], this kind of cancellation was assumed to be true without proof. We shall show in Chapter VI that by using non-abelian cut diagrams, we can reorganize a special kind of Feynman diagrams in such a way that this kind of cancellation takes place before the actual calculations.

Chapter 5. Relevant techniques

In this Chapter, we are going to deal with the difficulties mentioned at items 2 and 3 at the end of the last Chapter. Item 4 will be discussed in Chapter 5.1 and item 3 will be discussed in Chapter 5.2.

5.1 Path method for integration

5.1.1 Residue calculus and flow diagram

Given an l -loop Feynman diagram, we can write its amplitude as

$$\mathcal{T} = - \left(\frac{i}{2(2\pi)^4} \right)^l \int \left(\prod_{a=1}^l d^2 k_{a\perp} dk_{a-} dk_{a+} \right) \frac{N}{\prod_{i=1}^n D_i}. \quad (5.1)$$

The numerator N contains the vertices and other necessary factors. Each independent loop momentum shall be integrated from $-\infty$ to $+\infty$. In what follows we focus on quark-quark elastic scattering, and take the high energy limit $s \gg -t$. We will also assume that all the particles are massless. We will use the same conventions as those used for QED Feynman diagram in the last Chapter. In addition, we shall call the upper fermion line of a Feynman diagram the *top line*. Its momentum has only “+” components with magnitude \sqrt{s} . Similarly, the lower quark line shall be called *bottom line*. It has only “-” component with magnitude of \sqrt{s} . For each propagator,

the corresponding D_i is

$$q_{i+}q_{i-} - q_{\perp}^2 + i\epsilon, \quad (5.2)$$

where q_i is the momentum passing through that propagator. Since q_i is always linear in k_i , the independent loop momentum, so is D_i . Therefore, we can carry out the dk_{a+} integrations by using residue calculus. We choose the contour to be the real axis and a semi-circle at infinity. This semi-circle can be either on the upper half plane or the lower one, determined by convenience. Each of the internal lines in the loop gives rise to a pole, and our task is to determine whether this pole is on the upper plane or the lower one. For this purpose, flow diagrams were introduced by Cheng and Wu [28], which will be briefly reviewed here. We will then point out difficulties emerging in higher order calculations that have not been mentioned previously. We shall provide solutions to these problems in Chapter 5.1.2 [34].

Whether the pole at $d_i = 0$ of the dk_{a+} integral is on the upper plane or the lower plane depends on the sign of the coefficient of k_{a+} in that denominator. See equ. (5.2). A flow diagram is a convenient way to keep track of the relations between these signs. Since the coefficient of k_{a+} in the i th propagator is just q_{i-} , the location of the i th pole depends on the sign of q_{i-} . The flow diagram is just a Feynman diagram with an arrow on each line indicating the direction of the flow of the “-” component of the momentum of this line, viz., the sign of q_{i-} . To satisfy momentum conservation, there must be some incoming momenta and some outgoing momenta at

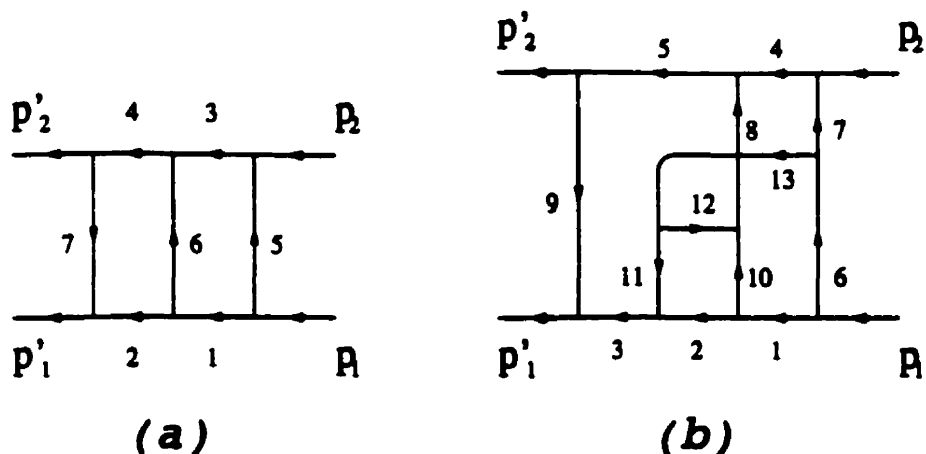


Figure 14: Two examples of flow diagrams.

each vertex. The lines with the arrows pointing in the same (clockwise or counter-clockwise) direction contribute to pole in the same half plane, while those with arrows pointing in opposite directions give rise to poles in the other half plane. A Feynman diagram can have several flow diagrams, each of them corresponds to a different integration region of the “-” component of the momentum. For example, Fig. 14(a) depicts a flow diagram of a two-loop Feynman diagram, and Fig. 24(b) is a flow diagram for a four-loop Feynman diagram. In the loop (1,5,3,6) of Fig. 14(a), the poles for lines 1 and 6 lie in one half-plane, and the poles for lines 3 and 5 lie in the other half. Similarly, in the loop (2,6,4,7), the pole for lines 2 lies in one half plane of that loop variable, and the lines 6,4, and 7 lie in the other half plane.

There are two general simplifications that can be made on flow diagrams. First, at high energies, a propagator on the top line can be approximately written as

$$D_i \simeq \sqrt{s}q_{i-} - q_{i\perp}^2 + i\epsilon \simeq \sqrt{s}q_{i-} . \quad (5.3)$$

It is independent of the "+" component of the loop momentum, and can be ignored in the integration of k_{a+} . For this reason, we may merge all the propagators on the top line in a flow diagram and ignore them.

Secondly, a flow diagram with a loop with all the arrows pointing in the same direction can be neglected. The reason is that this means all the poles are on the same half-plane in the integration of the loop momentum of this loop. When we choose the other half-plane to close the contour, we see that the amplitude for this Feynman diagram vanishes.

To summarize, given a Feynman diagram, we must first decide how the minus component of the momentum goes around the diagram according to momentum conservation subject to the condition that they do not flow all in the same direction around any closed loop. This will give us all the possible flow diagrams for to this Feynman diagram. This is basically the method invented by Cheng and Wu. However there are several subtle points in the approach which have been ignored before. These points are quite general, not limited to quark-quark elastic scattering. They will be discussed below.

5.1.2 Line reversal and path method

From the above discussion, we can see that the position of a pole is determined by the sign of q_{i-} , or equivalently by the arrow direction on the flow diagram. This is true before any k_{a+} integration is performed. However for multiloop diagrams,

we perform some of the k_{n+} integrations, the arrow might not indicate the sign of the “-” component any more. The reason for that will be explained below. Nevertheless, it turns out that this problem can usually be bypassed in low order calculations by choosing suitable independent loops, and/or different orders of integrations. As a result, it is a point that has been neglected in the literature.

To understand the problem in using flow diagrams for multi-loop situations, let us suppose there are n_1 poles picked up by the first loop integration $\int dk_{1+}$, each contributing to a term in the integral. As a result of the integration k_{1+} acquires an imaginary part $\mp i\epsilon/q_{i-}$ from the i th pole. The sign is $-/+$ if the direction of k_{1+} and q_{i-} are the same/opposite. This imaginary part in turn imparts an imaginary part on every q_{j+} of the first loop, which is why the location of poles for the second and subsequent integrations may be altered. For simplicity, we shall assume from now on that ϵ is finite and positive, and has a common value in all the propagators.

This imaginary part of k_{1+} affects the location of poles in subsequent integrations only for lines j lying in loop 1. In that case, the imaginary part of the quantity D_j in (5.2) is changed from $i\epsilon$ to

$$i\epsilon(\mp q_{j-}/q_{i-} + 1) , \quad (5.4)$$

with sign $-/+$ when lines j and i are in the same/opposite directions around the loop 1. Unless the sign is $-$ and $q_j > q_i$, the imaginary part of D_j remains positive and the location of pole j in subsequent integrations is once again determined solely

by the direction of its arrow around the integration loop, viz., it can be determined directly from the flow diagram. However, if lines j and i are in the same direction around the first loop, and that $q_j > q_i$, then the sign of the imaginary part of D_j becomes negative, and the pole location (upper or lower plane) will now be opposite to naive expectations from the flow diagram. This situation can still be accommodated into the flow diagram if we simply reverse the arrow of this line.

This is *flow reversal*.

To see how flow reversal works, we first look at a simple example shown in Fig. 14(a). This is a two-loop flow diagram. The corresponding Feynman diagram has two flow diagrams. The other one can be obtained by flipping line-6.

We have the freedom to choose different independent loops. Here we take $l_1 = (2, 6, 4, 7)$ and $l_2 = (1, 5, 3, 6)$ as independent loops. We can perform the loop integral of either one first.

l_1 first : For l_1 , we can take the pole on line-2. Then after the integration of this loop momentum, the loop left is l_2 , and we can take line-5 as the pole (remember the remark in equ. (5.3)). So the poles lie in lines (2,5).

l_2 first : For l_2 , of course, we can choose only line-5 as the pole. But we can also choose both line-1 and line-6 as poles. It is the latter case that gives problem. So we look at this case here. When we take the contributing pole from line-1 to perform the loop integral of l_2 , then the loop left after this is still l_1 ,

and we can pick up line-2 as the pole. Now take the pole of l_2 from line-6. Since line-6 is on the boundary of l_1 and l_2 , the remaining integration must be conducted on loop $l_3 = (1, 5, 3, 4, 7, 2)$. Without line reversal, this loop has two poles: line-1, and line-2, so we finally end up taking the pole contributions from $(1, 2) + (6, 1) + (6, 2)$, which is not the same as the above one. To get the right answer, we have to take into account line reversal. When we choose line-6 to perform the l_2 integral, because $q_6 < q_1$, line-1 gets reversed. So that in the integral of l_3 , only line-2 should be taken as contributing pole. Thus the answer is actually $(2, 1) + (2, 6)$, which is just the same as $(2, 5)$.

As we can see from the above example, line reversal must be taken into account in order to get the right answer. At low order calculations, there might be ways to bypass line reversal as we pointed out above, but at the multi-loop level, when the independent loops become more involved like Fig. 14(b), line reversal is inevitable. The situation becomes even worse, because there is not a unique way to choose the independent loops, nor a unique way to choose the order of integrations. Also, when the pole we pick up is on the boundary of the independent loops we choose, the loops sharing this boundary will be merged after we perform the corresponding integration. Thus in general for a multi-loop diagram detailed calculations must take place loop by loop, with careful consideration of line reversal and loop merging, so as to obtain the correct contributing poles. This makes the explicit calculations at higher order extremely messy.

To demonstrate how tedious this procedure is when the old method is used, we consider a four-loop level diagram shown in Fig. 14(b). After trying different choices, one will find out that the simplest case for independent loops is $l_1 = (4, 8, 12, 13, 7)$, $l_2 = (5, 9, 3, 11, 12, 8)$, $l_3 = (13, 12, 10, 1, 6)$, and $l_4 = (10, 12, 11, 2)$. We do the integrations according to this order, because it turns out to be the most convenient order. First we introduce some notation to simplify the discussion. We use $l_1(3)$ to denote taking line-3 as the pole in the integration of loop l_1 . And we use $l_1.l_2$ to denote the union loop of these two. This union loop can be construct by merging l_1 and l_2 , and deleting all the boundary lines.

For l_1 , we can take line-7 as the only pole. Because line-7 is not on the boundary of any of the independent loops we choose, so that we are left with three independent loops l_2, l_3, l_4 . For l_2 , there are two possible poles: $l_2(3)$ and $l_2(11)$. And we need to consider these two possibilities separately:

1. $l_1(7)l_2(3)$

For l_3 , because again line-3 is not on the boundary of the independent loops we choose, so when we perform the integration of l_3 , we can choose $l_3(1)$ and $l_3(10)$.

(a) $l_1(7)l_2(3)l_3(1)$

We can take line-10 and line-11 as the poles for l_4 , and get $l_1(7)l_2(3)l_3(1)l_4(10)+l_1(7)l_2(3)l_3(1)l_4(11)$.

(b) $l_1(7)l_2(3)l_3(10)$

Since line-1 is on the boundary of l_3 and l_4 , therefore the loop left is $l_3.l_4$. In addition, because $q_1 > q_{10}$, so that line-1 is reversed. Therefore, we have only one contributing pole for this case: $l_1(7)l_2(3)l_3(10)l_4.l_3(2)$.

2. $l_1(7)l_2(11)$

Because line-11 is on the boundary of l_2 and l_4 , so what is left now is l_3 and $l_2.l_4$. It is simpler to do the integral of $l_2.l_4$ first. Note that line-3 is reversed due to the fact that $q_{11} > q_3$ in this case, so for $l_2.l_4$ only line-2 is taken as a contributing pole. We have then $l_1(7)l_2(11)l_2.l_4(2)$. And for l_3 , we take line-1 and line-10. And the contribution pole is then $l_1(7)l_2(11)l_2.l_4(2)l_3(10) + l_1(7)l_2(11)l_2.l_4(2)l(1)$.

Therefore, in total there are 5 contributing poles for this diagram: $l_1(7)l_2(3)l_3(1)l_4(10) + l_1(7)l_2(3)l_3(1)l_4(11) + l_1(7)l_2(11)l_2.l_4(2)l_3(10) + l_1(7)l_2(11)l_2.l_4(2)l(1)$.

This is not the only way to get to the answer, and taking another way would be many more complicated. For example, if we choose to do l_4 after we perform l_1 , then we get to $l_1(7)l_4(11) + l_1(7)l_4(10)$. For these two cases, we need to compare q_{10} with q_{11} . This complicates the discussion a lot, although after careful discussion we can still get to the right answer.

Fortunately, there is a recipe to solve this problem. We shall call this the *path method* in the following.

For a general multi-loop *flow* diagram, we first choose a path P of the “-” flows. It is defined to be one of the continuous tree paths in which the “-” momentum goes through from the beginning to the end. In principle, any one of these paths can be used to find the contributing poles, but for a reason we will see later, we choose the longest path so as to make the practical calculation simpler.

Let us see how to get contributing poles from the path. For an l -loop flow diagram, after we choose the longest path, the internal lines that are *not* on the path are called *removed* lines. In general, the number of these removed lines N_r can be larger than or equal to l . A contributing pole is l lines selected from N_r removed lines. We can find all the contributing poles according to the following *directional rules*.

Rule.1 If $N_r = l$, then all these N_r removed lines are the only contributing pole to the flow diagram.

Rule.2 If $N_r > l$, then there is more than one contributing poles. Any one of them contains l lines. These l lines will satisfy the following conditions. (i) Removing these l -lines from the original l -loop diagram render it into a tree; (ii) When any one of these l lines is inserted back to the tree, a loop is formed. It is called *natural loop*. And the direction of this inserted line must be opposite to the natural loop it reconstructed.

Before we prove this directional method, we first consider the example of a

four-loop diagram shown in Fig. 14(b). The longest path can be taken to be $P = (6, 13, 12, 8, 5, 9)$. The removed lines are $(7, 3, 1, 2, 10, 11)$. We can see, if we insert line-7 to the path, it satisfies the directional rule. So every contributing pole should contain line-7. We still need to choose 3 lines from the remaining $(1, 2, 3, 10, 11)$. There are 10 possibilities. $(7, 2, 3, 11)$ and $(7, 1, 2, 10)$ violate rule.2.(i), because there is a loop remaining even after these 4 lines are removed. $(7, 3, 10, 11)$ violates rule.2.(ii) when line-11 is inserted; $(7, 1, 10, 11)$ violates the same one when line-10 is inserted; and $(7, 1, 2, 3)$ violates that rule when line-2 is inserted. Therefore there are 5 contributing poles: $(7, 3, 1, 10)$, $(7, 3, 1, 11)$, $(7, 3, 10, 2)$, $(7, 11, 2, 1)$, $(7, 11, 2, 10)$. A comparison with the ordinary method used above shows the high efficiency of our method. As an additional advantage, this method can be easily implemented into computer programs [42]. A successful example has been written up in *Mathematica*^R and C-language.

In summary, this method solves two problems at the same time, i.e. it chooses independent loops and the contributing poles.

Now we proceed to prove the above rules.

rule.1 It is easy to prove this rule; notice the fact that we are using flow diagrams.

If $N_p = l$, then when we insert any of these l lines to the path, it forms the corresponding natural loop. In this loop, only the inserted line is not on the path. According to the definition of the path, all the other lines are in the same direction. The inserted line must be in the opposite direction because

this is a flow diagram. Thus it is the pole we take for this loop.

rule.2 For an l -loop diagram, we can choose the path P according to its definition.

Also from this diagram, we can obtain trees by removing l lines. We call the set of these trees that share path P as their common backbone $S[P]$. $T[P]$ is a subset of $S[P]$ satisfying the condition that each tree in $T[P]$ corresponds to l removed lines which are a set of contributing poles. Then there is a one-to-one correspondence between the contributing poles and the trees in $T[P]$. A tree t in $T[P]$ defines l natural loops $N[t]$. The special feature of $N[t]$ is that the removed lines are never on the boundary of two natural loops of the original diagram.

The proof is then based on the following three assumptions, which will be proven in the Appendix. They are : i) $T[P]$ is never empty; ii) none of the lines in the contributing poles are in the reversed direction when a pole is taken from them; and (iii) the same contributing poles never occur more than once in the set.

There are also two observations: i) the contributing poles we take shall always have arrows running in the opposite direction as those on P ; ii) these contributing poles are independent of the choice of loops and the order of integrations from which they are obtained.

Take t_0 from $S[P]$, we have a set of natural loops $N[t_0]$, according to assump-

tion i). Because of assumption ii), we can perform the integrations in these loops and obtain the contributing poles, each of them corresponding to a tree in $S[P]$ obtained by removing the contributing poles from the original diagram. This set of trees will be denoted by $T'[P]$. We need to show $T'[P] = T[P]$.

Any tree in $T'[P]$ must satisfy the directional rules, so we have $T'[P] < T[P]$. On the other hand, if we take a tree from $T[P]$, and use the corresponding natural loops $N[t]$ to compute the contributing poles, and based on the two observations, we can conclude that the lines removed to get t from the original diagrams are one set of the contributing poles. Thus $T[P] < T'[P]$.

Therefore, we can see that $T[P] = T'[P]$, and it proves our directional method.

5.2 Non-abelian cut diagram

The multiple commutator formula is a generalization of the eikonal formula to the non-abelian amplitude [31]. We will first present the formula here, and then give examples to illustrate how to use this formula. The complete proof will be presented in the Appendix.

When we compute a tree process in a non-abelian gauge theory, we write the amplitude of a Feynman diagram in two parts as before.

$$a[123 \cdots n] \cdot t[123 \cdots n] \equiv a[123 \cdots n] t_1 t_2 t_3 \cdots t_n, \quad (5.5)$$

where t_a is the non-abelian color factor associated with the vertex. The multiple

commutator formula states that

$$\sum_{\sigma \in S_n} a[\sigma] t[\sigma] = \sum_{\sigma \in S_n} a[\sigma]_c t[\sigma]'_c, \quad (5.6)$$

where $S_n = \{1; 2; \dots; n\}$ is just all the permutation of $(1, 2, \dots, n)$, $a[\sigma]_c$ is a cut amplitude for the cut diagram $[\sigma]_c$, and $t[\sigma]'_c$ is the corresponding nonabelian factor computed from the *complementary cut diagram* $[\sigma]'_c$. The cut diagram and the complementary cut diagram are defined in the following way. Proceeding from left to right along the tree $[\sigma]$, a cut is put after a number iff there is not a smaller number to its right. Hence, we can have the following example:

$$[1234]_c = [1|2|3|4], \quad [2314]_c = [231|4], \quad [4321]_c = [4321]. \quad (5.7)$$

The complementary cut diagram $[\sigma]'_c$ is the one where lines cut in $[\sigma]_c$ are not cut in $[\sigma]'_c$, and vice versa. Therefore we have

$$[1234]'_c = [1234], \quad [2314]'_c = [2|3|14], \quad [4321]'_c = [4|3|2|1]. \quad (5.8)$$

To calculate the non-abelian factor from the complementary cut diagram, we replace a cut with a commutator. So that

$$\begin{aligned} [1234]'_c &= [1234] = t_1 t_2 t_3 t_4, \\ [2314]'_c &= [2|3|14] = [t_2, [t_3, t_1]] t_4, \\ [4321]'_c &= [4|3|2|1] = [t_4, [t_3, [t_2, t_1]]]. \end{aligned} \quad (5.9)$$

Here we just look at two examples for $n = 2$ and $n = 3$, and leave the complete proof in App.A.

1. $n=2$:

According to the rule above, we can have the cut diagrams as:

$$a[1|2]t[12] + a[21]t[2|1] . \quad (5.10)$$

To see this is the right answer of the summation of all the Feynman diagrams for $n = 2$, we can just expand all the cuts:

$$\begin{aligned} a[1|2]t[12] + a[21]t[2|1] &= (a[12] + a[21])t[12] + a[21](t[21] - t[12]) \\ &= a[12]t[12] + a[21]t[21] . \end{aligned} \quad (5.11)$$

2. $n=3$:

The amplitude can again be written as:

$$\begin{aligned} &a[1|2|3]t[123] + a[1|32]t[13|2] + a[21|3]t[2|13] + a[231][2|3|1] \\ &+ a[31|2]t[3|12] + a[321]t[3|2|1] . \end{aligned} \quad (5.12)$$

Again a straightforward expansion of all the cuts can restore the 6 Feynman diagrams.

Chapter 6. Calculation of diagrams up to 6th order

In this section, we are going to use the techniques introduced in the previous chapter to re-do the calculation of all the Feynman diagrams up to 6th order. Furthermore, we will use the calculations here as an illustration of how to do higher order computations. All the Feynman diagrams are given in Fig. 15. Note that from now on, for simplicity, we draw the fermion lines (the top line and the bottom line) the same as the gluon line.

As we can see from the QED case, by introducing cuts to the top line of the Feynman diagrams, we can simplify calculations. With this in mind, we intend to do the same thing for non-Abelian Feynman diagrams up to 6th order in this chapter. All the relevant Feynman diagrams are shown in Fig. 15, using the same convention as in Ref.[34]. All the diagrams can be divided into 2 groups according to the different topology. The first group contains all the diagrams with same number of gluon lines joined to the top line and the bottom line, the second group consists of all the rest.

Group 1 This group consists of the 2nd order diagram A1, the 4th order diagrams B1 and B2, together with the 6th order diagrams C15, C16, C17, C18, C19, C20,

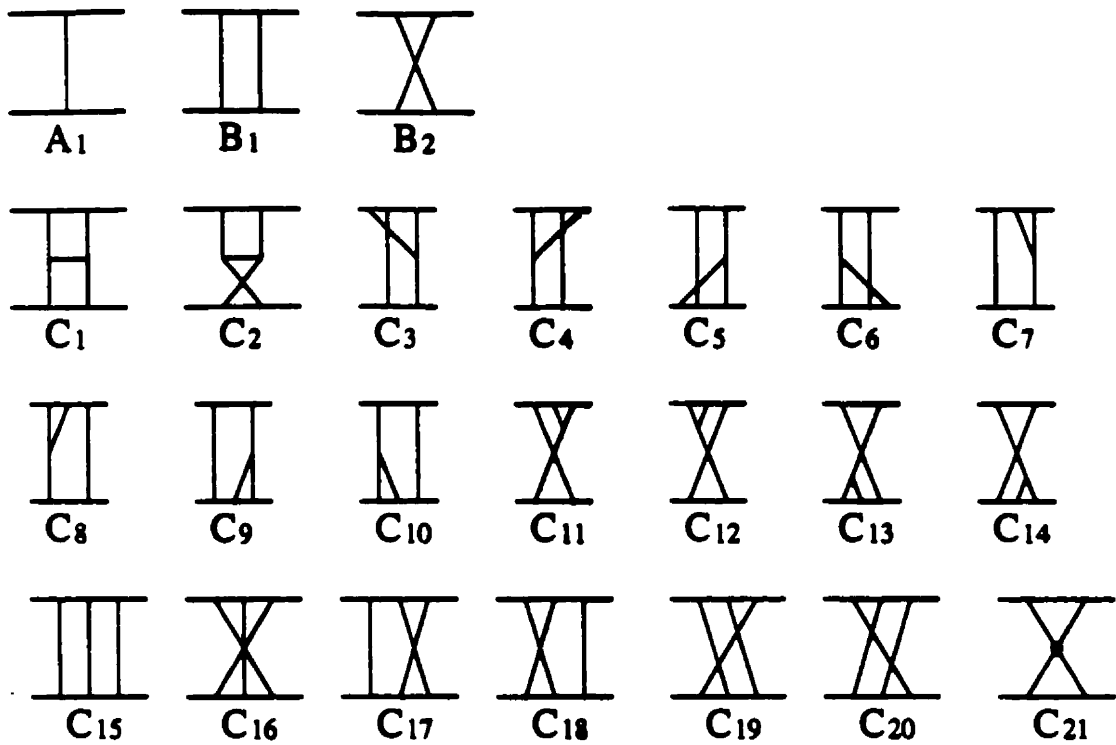


Figure 15: Feynman diagrams for quark-quark elastic scattering at 6th order.

C21, C1, and C2. We can introduce cuts to the top line by a direct application of the non-abelian cut diagrams mentioned in the last chapter. First we look at A1, B1, B2, C15, C16, C17, C18, C19, and C20. These diagrams contains only fermionic vertices. We shall call them *s-channel ladder diagrams* [34]. If we remove the bottom line of a *s-channel ladder diagram*, it will become a tree diagram. Here we use C18 as an example. The resulting tree by removing the bottom line is shown in Fig.16. Each gluon line is given a number as illustrated in Fig. 16(a). Using the rule introduced in the last chapter, we know that the spacetime diagram can be cut as in Fig. 16(b). As for the color diagram, it can be cut according to the complementary rule as follows. Since the propagator

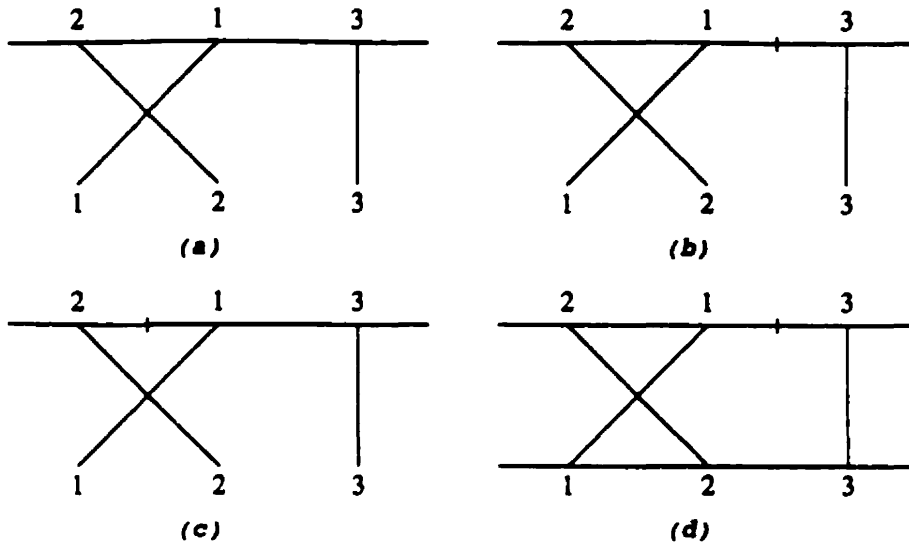


Figure 16: An example of using non-abelian cut diagram.

between lines 1 and 3 is cut in the spacetime diagram Fig. 16(b), it should not be cut in the color diagram Fig. 16(c). And the propagator between line 2 and 1 is not cut in Fig. 16(b), so it should be cut in Fig. 16(c). By putting back the bottom line, we get the non-abelian cut diagram for C18 as shown in Fig. 16(d). This example shows how to apply the rule introduced in the last chapter to loop diagrams. Following the same way, we can get the non-abelian cut diagrams corresponding to all the s -channel ladder diagrams. The result is shown in Fig. 17. Here $A1$ is a special s -channel ladder diagram since there is not propagator on the top line. So $A1_c = A1$.

Again, a cut on a spacetime diagram means a δ function replacing the ordinary propagator in the Feynman rule. On the other hand, a cut in a color diagram

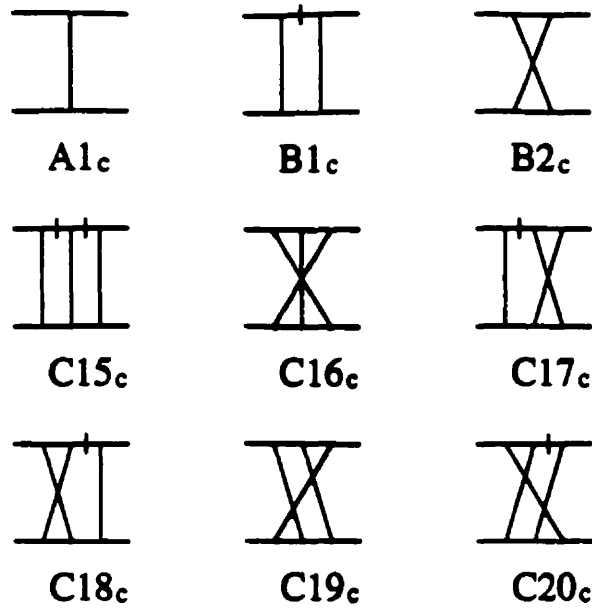


Figure 17: Non-abelian cut diagrams.

means a commutator of the color matrices t_a, t_b of a quark: $[t_a, t_b] = [t_a, t_b] = [t_a, t_b] - [t_b, t_a]$. Graphically this identity can be shown as Fig. 18(a). To get the last diagram of this identity, we have used the following equation:

$$[t_a, t_b] = if_{abc}t_c, \quad (6.1)$$

together with the fact the color factor of a triple gluon vertex is just if_{abc} . Other useful identities are given in Fig. 18(b, c, d), where $c = N_c/2$ for a color $SU(N_c)$ group. Note that Fig. 18(b) has an extra minus sign compared with Fig. 18(a). This minus sign comes from the different orientation of the triple gluon vertex. As for identity Fig. 18(c,d), they are the graphical representation of the following two equations:

$$f_{abc}f_{abd} = 2c\delta_{cd}, \quad i^3 f_{adg}f_{bed}f_{cge} = ci f_{abc}. \quad (6.2)$$

These identities will be used later to uncross the gluon lines so as to get desired

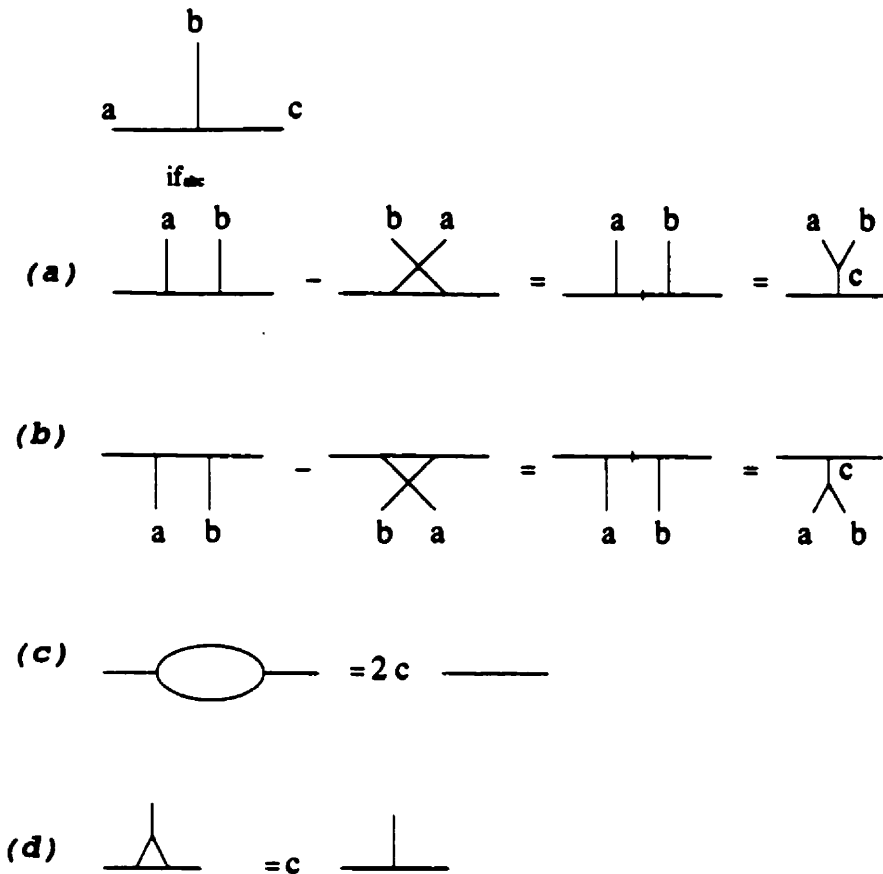


Figure 18: Graphical representation of the identities in $SU(N_c)$ algebra.

planar color diagrams.

Now we look at the remaining three diagrams in this group, namely $C1$, $C2$, and $C21$. We can combine part of $C21$ with $C1$ to form $\bar{C}1$, and combine the rest of $C21$ with $C2$ to form $\bar{C}2$, as done by Cheng and Wu [28]. We keep on using the same pictures to represent $\bar{C}1$ and $\bar{C}2$. They are the same as the s -channel diagrams above in the sense that the number of gluon lines joined to the top line is the same to the number of gluon lines joined to the bottom line.



Figure 19: Reorganization of $\bar{C}1$ and $\bar{C}2$ for 6th order.

As a result, if we ignore the horizontal gluon line, then they become 4th order s -channel diagrams. Similarly we can introduce cut to the upper fermion line. Then $\bar{C}1$ and $\bar{C}2$ can be reorganized as cut diagrams shown in Fig. 19.

Group 2 This group contains the rest of the diagrams from Fig. 15. Note that each of these diagrams contains a triple gluon vertex. We want to put cuts on the top line of each diagram as well.

This group can be further divided into two subgroups according to the number of gluon lines joined to the top and bottom lines. We shall use a different way to put cuts on the top lines for these two subgroups respectively.

(a) This subgroup consists of C5, C6, C9, C10, C13, and C14 from Fig. 15.

All these diagrams contain a triple gluon vertex showing as an upside-down Y. To apply the rule we used in Group 1, we just need to ignore the right branch of the triple gluon vertex. Take C6 for example. It is shown as in Fig. 20(a). If we ignore the right branch of the triple gluon vertex, then we get a fourth order s -channel diagram Fig. 20(b), and it can be cut as Fig. 20(c) according to the rule before. Thus C6 can be

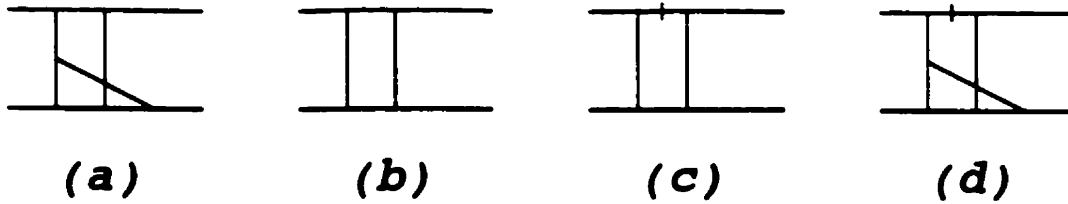


Figure 20: An example of how to cut diagram C_6 .

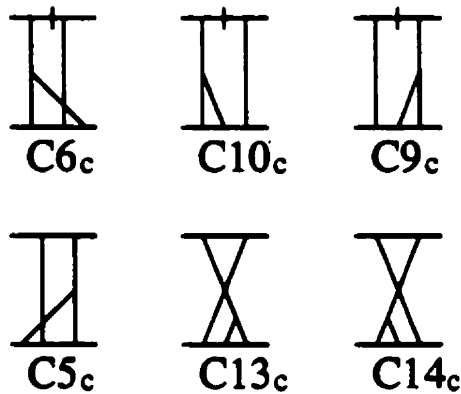


Figure 21: Reorganization of 6th order diagrams with upside-down Y vertex.

cut as Fig. 20(d), which we shall call C_{6c} later. The same is true for all the other diagrams in this subgroup. We put all the corresponding cut diagrams in Fig. 21. It is worth remembering that there is no equivalence between individual Feynman diagram and its corresponding cut diagram. Only the sum of diagrams in this subgroup equals to the sum of the corresponding cut diagrams in Fig. 21.

(b) This subgroup contains C3, C4, C7, C8, C11, and C12. As a general rule, the non-abelian cut diagram used above is also applicable to all diagrams in this subgroup by choosing appropriate numbering of the gluon lines. However, this will get to $2 * 3! = 12$ cut diagrams as shown in [32], where $3!$ comes from the permutation of all three line on the top, and the factor of 2 results from two different choices to number those two gluon lines joining to a triple gluon vertex. To avoid computing more diagrams, an alternative way is to decompose the color factor of each Feynman diagram into planar diagrams. The disadvantage though is that we cannot get the cut diagrams directly. Instead, we have to use the factorization formula equ. (4.3) after we decompose all the color factors. To do it, we first use C4 as an example. The color factor of C4 can be represented by Fig. 22(a). We can use the identity shown in Fig. 18 to uncross the gluon lines, then Fig. 22(a) can be expressed as sum of two terms: Fig. 22(b, c). These two can be further simplified into planar diagrams as Fig. 22(d,e). We can do the same thing for the other diagrams in this subgroup, and the result is put in Fig. 23. Here each diagram has been expressed as product of spacetime diagrams and the color diagrams inside the bracket, which have been decomposed into planar diagrams. To get the cuts on the top line of the spacetime diagrams, we can group them according to color factors. For example, C8, C4, and C11 all contributes to a color diagram

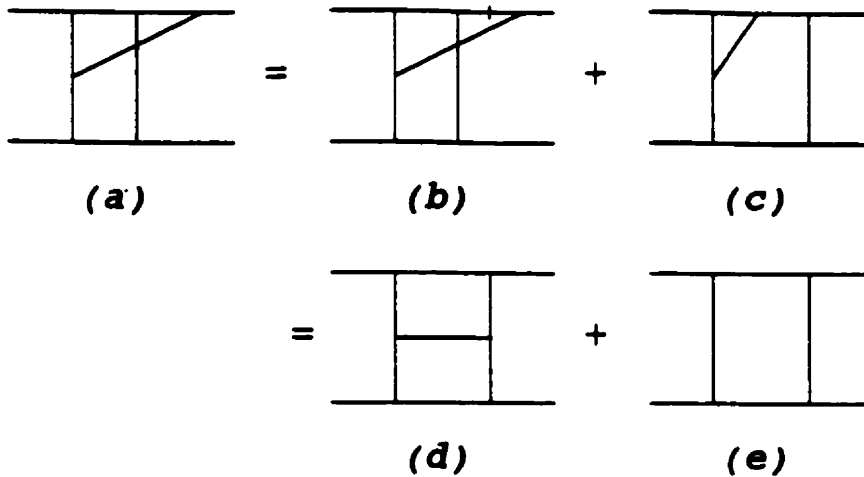


Figure 22: Decomposition of the color factor of C3 into planar color diagram.

Fig. 24(a). So we can sum them up. If we number the gluon lines as shown in Fig. 24, we can see that $[123] + [132] + [213] = \{2; 13\} = [2|13]$. (See section 4.5.1). We call the resulting diagram on the right hand side *C8c*.

C7, C12, and C3 also contribute to the same color factor. We did not mix them with the previous three diagrams, because it turns out that they themselves can be summed up into a cut diagram shown as *C7c* in Fig. 25. By doing the same thing for each color factor, we find that all the diagrams in this subgroup can be organized into cut diagrams shown in Fig. 25. Again we put the color diagrams in brackets.

Next we are going to compute these cut diagrams. In addition, we want to show by our calculation that up to this order, multi-Regge amplitude can be obtained from summing these cut diagrams, which in turn come from Feynman diagrams. We are going to do this in two steps. First we must decompose all the remaining

$$c_4 \quad \text{II} \cdot (\text{II} + \text{II}) = \text{II} \cdot (\text{H} + \text{II})$$

$$c_3 \quad \text{N} \cdot (\text{N} + \text{N}) = \text{N} \cdot (\text{H} + \text{II})$$

$$c_7 \quad \text{N} \cdot (\text{N}) = \text{N} \cdot (\text{II})$$

$$c_8 \quad \text{VI} \cdot (\text{VI}) = \text{VI} \cdot (\text{II})$$

$$c_{11} \quad \text{X} \cdot (\text{X} + \text{VI}) = \text{X} \cdot ({}^2\text{I} + {}^c\text{II})$$

$$c_{12} \quad \text{X} \cdot (\text{X} + \text{N}) = \text{X} \cdot ({}^2\text{I} + {}^c\text{II})$$

Figure 23: Color decomposition of 6th order diagrams with Y vertex.

$$\text{II} \cdot \left(\overset{1 \ 2 \ 3}{\text{II}} + \overset{1 \ 3 \ 2}{\text{VI}} + \overset{2 \ 1 \ 3}{\text{X}} \right) = \text{II} \cdot \overset{1 \ 3 \ 2}{\text{VI}}$$

(a) (b) (c) (d) (e)

Figure 24: Color decomposition of 6th order diagrams with Y vertex.

$$\begin{array}{ll}
C8c & \text{Diagram 1} * \binom{c}{\text{Diagram 2}} & C7c & \text{Diagram 3} * \binom{c}{\text{Diagram 4}} \\
C4c & \text{Diagram 5} * \binom{c}{\text{Diagram 6}} & C3c & \text{Diagram 7} * \binom{c}{\text{Diagram 8}} \\
C11c & \text{Diagram 9} * \binom{2}{c} \binom{c}{\text{Diagram 10}} & C12 & \text{Diagram 11} * \binom{2}{c} \binom{c}{\text{Diagram 12}}
\end{array}$$

Figure 25: Color decomposition of 6th order diagrams with Y vertex.

non-planar color factors of each cut diagram into sums of the planar color diagrams, as done in Fig. 23. Secondly, we are going to sum up all the contributions to each planar color factor and show that multi-Reggeon feature does exist.

All the color factors of the relevant cut diagrams can be calculated. The results are collected in Fig. 26. Here we have used the same convention as in [34] by calling the cut diagrams Cn_c with $n= 1,2,..21$.

Based on this result, all the cut diagrams will be computed according to different planar color factors as follows.

G_4 There is only one cut diagram $C15_c$ contributing to this color factor. This diagram is exactly the same as the abelian cut diagram for QED. Therefore,

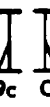
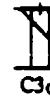
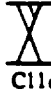
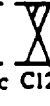
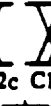
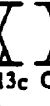
Group factors for SU(3) Diagrams	G_1	G_2	G_3	G_4
	0	0	0	1
	9/4	0	0	0
	0	-3/2	0	0
	0	-3/2	-1	0
	0	-3/2	0	0
	9/4	0	0	0
	0	-3/2	0	0
	0	-3/2	0	0
	0	-3/2	0	0
	0	-3/2	0	0
	0	0	1	0
	0	0	1	0
	-9/4	0	0	0
	-9/4	0	0	0
	-9/4	0	0	0
	-9/4	0	0	0
	0	-3/2	1	0
	0	0	1	0
	9/4	0	0	0
	9/4	0	0	0
	1	0	0	0
	0	1	0	0
	3/2	0	0	0

Figure 26: Color decomposition of all the cut diagrams at 6th order.

the T matrix element is given by

$$\frac{s}{2m^2} \frac{g^6}{6} I_3(\Delta) G_4 . \quad (6.3)$$

Again, $I_n(\Delta)$ is the n th-power convolution of I_1 with itself. (See equ. (4.6)).

G_1 Among others, there are two s -channel ladder diagrams $C16_c$ and $C19_c$ contributing to this color factor. But in these two diagrams, none of the propagators on the top line are cut. According to a theorem introduced in Ref.[34], diagrams (space-time) with two adjacent uncut propagators is unsaturated, in the sense that they give rise to subleading contributions. This theorem will be proven in App.B. Therefore, these two diagrams can be neglected at high energy approximation. That leaves contributions from $A1_c$, $B1_c$, $\bar{C}2_c$, $C11_c$, $C12_c$, $C13_c$, $C14_c$, and $C5_c$. $A1_c$ is just the Born term, and its result can be easily obtained as $A1c = -\frac{g^2 s}{2m^2 \Delta^2}$.

$B1c$ is shown in Fig. 27 with all the lines labeled. We can see that the longest path is (1,2,3), and the contributing pole is (4). Therefore, the integral of the longitudinal components can be easily obtained as $B1c = \frac{g^2 s}{2m^2} \beta c(\ln s) I_2$, where $\beta = g^2/(2\pi)$. The details of the calculation will be given in App. B.

To compute $\bar{C}2_c$, we need to perform the integral of the longitudinal momenta. We first need to draw the flow diagrams. There is only one flow diagram for this scalar diagram. We label the lines as shown in Fig. 27($\bar{C}2_c$). Then we choose the longest path as (6,8,9,10,7). And the contributing pole can be

immediately recognized as (5,11). And the result is

$$-\frac{s}{2m^2} \frac{g^6}{4\pi^2} (\ln^2 s) \left[\frac{1}{2} \Delta^2 I_2^2 - J_2 I_2 \right] c^2 ; J_2 \equiv \int \frac{d^2 q_\perp}{(2\pi)^2} \frac{1}{q_\perp^2} . \quad (6.4)$$

Again the detail to get this result will be given in App. B.

As for $C11_c$ shown in Fig. 27(b), the longest path will be (1,2,3,4,5) and the contributing pole is (6,7). So it can be easily calculated as

$$\frac{s}{2m^2} \frac{g^6}{4\pi^2} (\ln^2 s) \frac{1}{4} J_2 I_2 . \quad (6.5)$$

And we can see that

$$C11_c = C12_c = C13_c = C14_c . \quad (6.6)$$

$C5_c$ can be computed to be

$$-\frac{s}{2m^2} \frac{g^6}{8\pi} (\ln s) J_2 I_2 . \quad (6.7)$$

Since it is subleading compared to the other 5 diagrams, its contribution can be ignored here.

Therefore, the results can be summed to be

$$\frac{s}{2m^2} \left(-\frac{g^2}{\Delta^2} + \frac{g^4}{2\pi} c (\ln s) I_2 - \frac{1}{2} \frac{g^6}{(2\pi)^2} (\ln^2 s) \Delta^2 I_2^2 c^2 \right) . \quad (6.8)$$

G₃ As for the color factor of G_3 , the relevant diagrams are: $\bar{C}1_c$, $C20_c$, $C6_c$, $C3_c$, and $C4_c$.

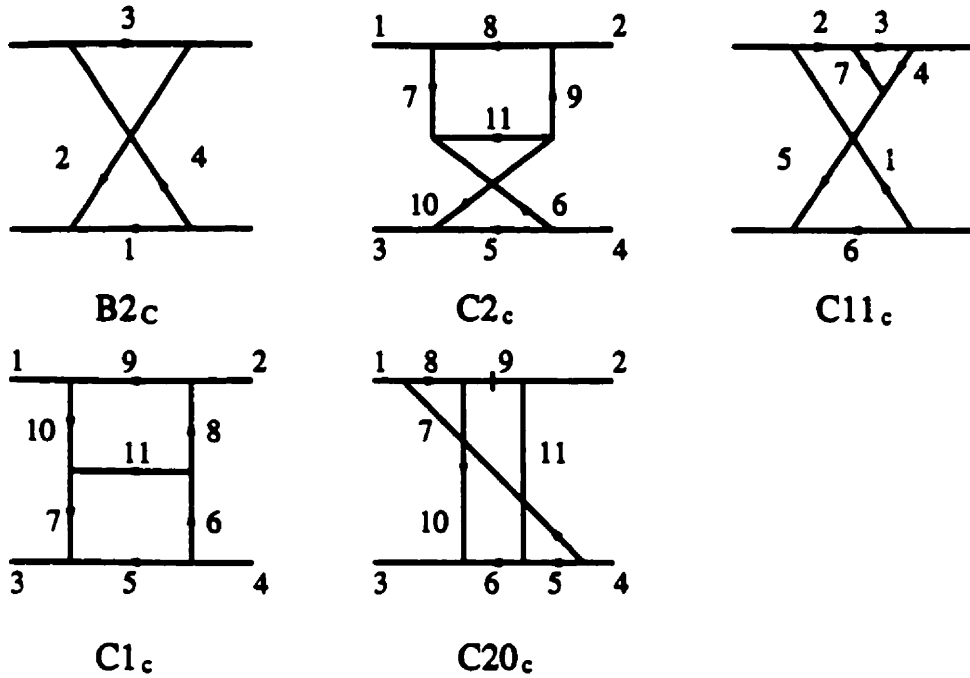


Figure 27: Flow diagram for $B2_c$, $C1_c$, $C11_c$, $C2_c$, and $C19_c$.

The flow diagram for $C1_c$ is shown in Fig. 27. The longest path is (6, 7, 8, 9, 10), and the contributing pole is (5, 11). The result can be obtained to be:

$$-\frac{s}{2m^2} g^4 i \beta (\ln s) \left[\frac{1}{2} \Delta^2 I_2^2 - J_2 I_2 \right]. \quad (6.9)$$

The result for $C6_c$ can also be easily computed as

$$-\frac{s}{2m^2} \frac{1}{2} g^4 \beta^2 \ln s J_2 I_2. \quad (6.10)$$

This result is just the same as the sum of $C3_c$ and $C4_c$.

The other diagram contributing to G_3 is $C20_c$. Its flow diagram is also drawn in Fig. 27 with longest path being (7, 8, 10). It can be computed as

$$\frac{s}{2m^2} g^4 \beta i (\ln s) I_3 G_3. \quad (6.11)$$

By summing all the results above, we can get the contribution to G_3 to be

$$\frac{s}{2m^2} ig^4 \beta(\ln s) (I_3 - \frac{1}{2} \Delta^2 I_3^2) . \quad (6.12)$$

G_2 This color factor receives contributions from one 4th order and three 6th order s -channel ladder diagrams. Instead of calculating the cut diagrams one by one, we use the formula shown in equ. (4.3) to resum them first. It turns out that this resummation is in general true for all orders as proven in the next section. For the 4th order cut diagram $B2c$, we can do the similar thing as for QED shown Fig. 13. Then we can get a cut on the lower line. And this simply gives $B2c = (1/2) \frac{s}{3m^2} ig^4 I_3$.

As for the 6th order, the diagrams we need to sum up are $C17c$, $C18c$, and $C20c$. We redraw them in Fig. 28 as (a), (b), and (c) respectively. Note that they are all spacetime diagrams. The diagram for $C17$ in Fig. 28 is the same as that in Fig. 26 because the top end of line-3 can be moved back to the left of line-1 using the commutable property of a cut. Now if we look at the bottom line, we have the following identity from equ. (4.3).

$$[321] + [231] + [213] = \{21; 3\} = [21|3] . \quad (6.13)$$

Graphically, this identity is shown in Fig. 28(1).

Therefore, summing these three diagrams, we can get a cut on the bottom line as shown in Fig.28(d). The computation of this diagram is straightforward

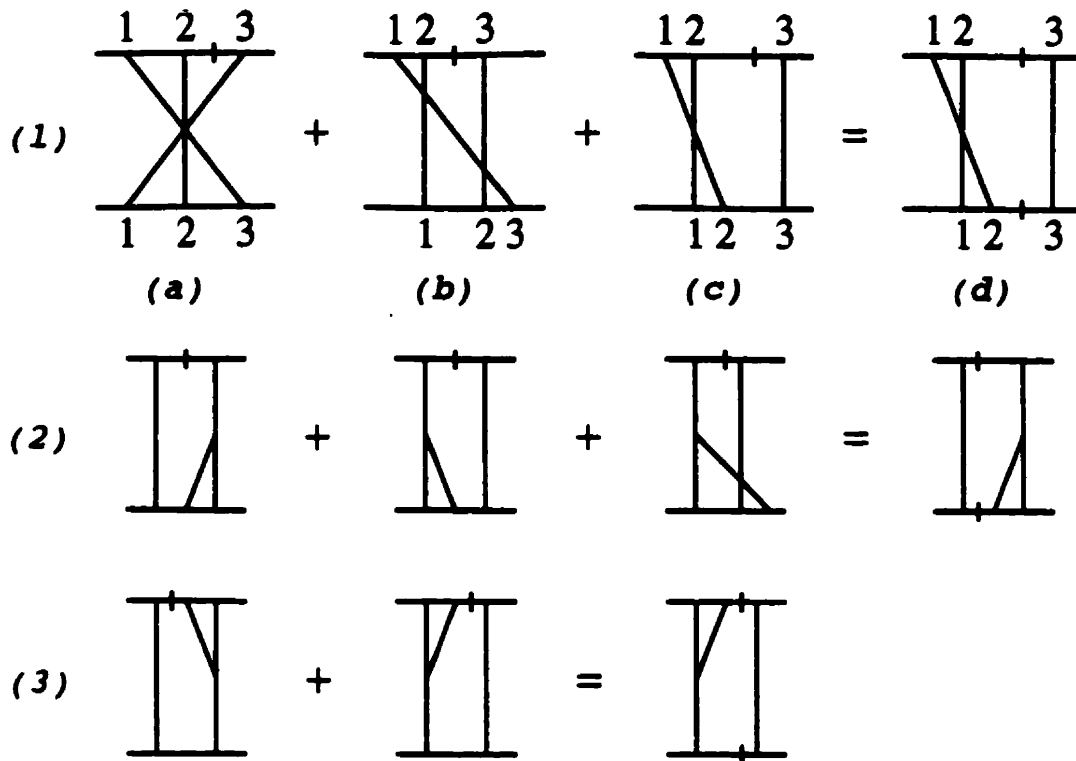


Figure 28: Summing cut diagrams to introduce cut in the lower fermion line.

because of those two cuts. In the longitudinal component space, because of the δ -functions, the line being cut on the top must carry momentum p_1 and the line being cut on the bottom must carry momentum p_1 . This means that the longitudinal component of this diagram is simply the product of the longitudinal components of A1 and B1. As for the transverse component, because the propagators of the cut lines are replaced by *delta*-functions, it is just the convolution of the transverse components of A1 and B1. Therefore, the result can be written as

$$-\frac{s}{2m^2} g^4 \beta i (\ln s) I_{3c} G_2 . \quad (6.14)$$

The other cut diagrams contributing to this color factor can be divided into

two groups: $C7_c + C8_c$, and $C6_c + C9_c + C10_c$. Using the same idea as above, we can obtain the identities shown as Fig. 28(2,3). It can be easily seen that the longitudinal part of the right-hand side of identities (2) and (3) in Fig. 28 can also be represented as product of a 2nd order diagram and a 4th order diagram. Note that the 4th order diagram is just a vertex correction [48], so that these two diagrams can be ignored compared with equ. (6.12).

In summary, we can sum all calculational result as follow

$$\begin{aligned}
\mathcal{T} &= \frac{(-i)s}{2m^2} \left(-\frac{ig^2}{\Delta^2} + \frac{g^4}{2\pi} ic \ln s I_3 - \frac{i}{2} \frac{g^6}{4\pi^2} c^2 \Delta^2 I_3^2 \ln^2 s \right) G_1 + \\
&\frac{(-i)s}{2m^2} \left(-\frac{1}{2} g^4 I_3 + \frac{g^6}{2\pi} c I_3 \ln s \right) G_2 + \\
&\frac{(-i)s}{2m^2} \left(-\frac{g^6}{2\pi} (\ln s) (I_3 - \frac{1}{2} \Delta^2 I_3^2) \right) G_3 + \\
&\frac{(-i)s}{2m^2} \left(ig^6 \frac{1}{6} I_3 G_4 \right) \\
&\equiv \frac{(-i)s}{2m^2} (X_1 G_1 + X_2 G_2 + X_3 G_3 + X_4 G_4) . \tag{6.15}
\end{aligned}$$

This result is the same as shown in Cheng and Wu's book [28] calculated directly from Feynman diagrams, not cut diagrams. Again one of the advantages of using non-abelian cut diagram is that for each cut diagram we need to keep only leading contributions. For example, if we use Feynman diagram directly, we will see that the leading contributions from B1 and B2 cancel each other in the color amplitude proportional to G_2 . So we need to calculate up to the subleading order.

In summary, although the above calculations is only up to the 6th order, the result in equ. (6.15) shows the following important points:

1. Factorization

If we take a look at the coefficient of G_4 in equ. (6.16), the corresponding cut diagram is $C15_c$. The transverse component is

$$I_3 = \int \prod_{i=1}^3 \left(\frac{d^2 q_{i\perp}}{(2\pi)^2} \frac{1}{q_{i\perp}^2} \right) (2\pi)^2 \delta^2 \left(\sum_{i=1}^3 q_{i\perp} - \Delta \right), \quad (6.16)$$

This is the 3rd power convolution of I_1 with itself. Performing a Fourier transformation, we can change it into a product in the impact parameter space,

$$\tilde{I}_3(b) = \int d^2 b e^{i\Delta \cdot b} I_3 = \tilde{I}_1^3. \quad (6.17)$$

as convolutions generally change into products. Thus to this order X_4 is just one-sixth ($1/3!$) of the third power of X_1 in the impact parameter space. Similarly, to this order, X_2 is just one half ($1/2!$) of X_1 in the impact parameter space. This is what we refer as *factorization*.

This factorization is crucial for the multi-Reggeon interpretation, as we shall see in the next item. Up to the 6th order, factorization emerges in the final result, and the question is whether it is true as well in higher orders. If it does, do we need to calculate all the relevant diagrams to show it? To get an idea, let us look at the 6th order calculations more carefully. X_4 is represented by a cut diagram like Fig. 13(b). The cuts on *both* the top and bottom lines actually separate this diagram into three parts, each of which is essentially an

A1. Since A1 determines the lowest order of X_1 , this shows a close connection between cuts and factorization.

Actually, we can prove in general that putting cuts on *both* the top and bottom lines to separate a diagram into parts is equivalent to factorizing these separated parts into products in the impact parameter space. To show it, let us look at a general Feynman diagram Fig. 29(a), which contributes to elastic scattering at the high energy limit. We assume that the incoming momenta are p_1 , and p_2 respectively, and the total momentum transfer is Δ , which is transverse. In Fig. 29(a), we have drawn two propagators explicitly connecting two shaded areas, which represent possibly very complex structures. We also assume that the propagator on the top line carries momentum $p_2 + k$. Then the amplitude of this diagram can be written as

$$M = \int d^4k A(k^+, k^-, k_\perp) B(k^+, k^-, \Delta - k_\perp) P(p_2 + k) P(p_1 - k), \quad (6.18)$$

where A and B are the amplitudes represented by those two shaded areas. We write them as functions of momentum transfer. $P(k)$ is the propagator. Now if we put cuts on those two propagators as shown in Fig. 29(b), those two propagators P are replaced by δ functions. The amplitude for the cut diagram will be:

$$M_c = -\frac{4\pi^2}{s} \int dk^+ dk^- d^2k_\perp \delta(k^-) \delta(k^+) A(0, 0, k_\perp) B(0, 0, \Delta - k_\perp). \quad (6.19)$$

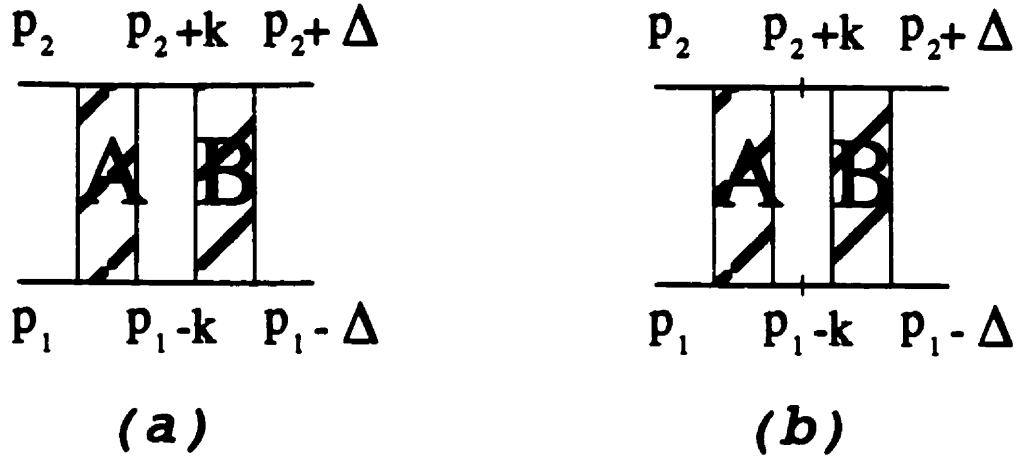


Figure 29: The connection between cuts and factorization.

In the impact parameter space, we have

$$\begin{aligned}
 \bar{M}_c &= -\frac{4\pi^2}{s} \int dk^+ dk^- d^2 k_\perp \delta(k^-) \delta(k^+) A(0, 0, k_\perp) B(0, 0, \Delta - k_\perp) e^{i\Delta \cdot b} d^2 \Delta \\
 &= -\frac{4\pi^2}{s} A(\bar{b}) B(\bar{b}) .
 \end{aligned} \tag{6.20}$$

Hence to show factorization of higher order diagrams, we need to put cuts on both the top and bottom lines. The non-Abelian cut diagrams give us a rule to introduce cuts to the top line. To put cuts on the bottom line, as we can see from the example in Fig. 28, we need to use the factorization formula to sum the relevant non-Abelian cut diagrams. This is not an easy task in general. Nevertheless, we are going to show that this can be done for the s -channel ladder diagrams in the next chapter.

2. Multi-Reggeon exchange

We can now show that up to the 6th order, equ. (6.15) contains multi-Reggeon-exchanges, with the reggeized-gluon propagator given by:

$$R_1(\Delta, s) = \frac{1}{\Delta^2} \exp(-\bar{\alpha}(\Delta) \ln s), \quad \bar{\alpha}(\Delta) = \frac{cg^2}{2\pi} \Delta^2 I_2(\Delta). \quad (6.21)$$

To see it, we first look at Born term A_1 . If we replace the gluon propagator in this diagram by a Reggeon propagator, graphically represent it by Fig. 9(a), this diagram can be interpreted as a single Reggeon exchange. Its amplitude is given by

$$\frac{1}{2m^2} \frac{1}{\Delta^2} \left(g^2 - g^4 \frac{c}{2\pi} \Delta^2 I_2(\ln s) + \frac{c^2}{4\pi^2} g^6 \Delta^4 I_2^2 + o(g^8) \right), \quad (6.22)$$

where we have expanded the exponential. We can see that the right-hand side of equ. (6.22) is just the same as the coefficient of G_1 in equ. (6.15) up to this order. Note that the coefficient of G_1 receives contributions from A_{1c} , B_{2c} , and C_{2c} . This means a Reggeon can be thought of as constructed from numerous gluons.

Furthermore, as we showed above, in the impact parameter space, $\vec{X}_2 = (1/2!) \vec{X}_1 \vec{X}_1$, and $\vec{X}_4 = (1/3!) \vec{X}_1 \vec{X}_1 \vec{X}_1$. If X_1 is interpreted as a single Reggeon exchange amplitude, these two can then be identified respectively as 2-Reggeon and 3-Reggeon exchange amplitudes. We can see that up to this order they

agree with an n -Reggeon exchange amplitude given by

$$\frac{g^{2n}}{n!} \frac{s}{2m^2} \frac{g^2}{2m^2} \int \left(\prod_{i=1}^n \frac{d^2 q_{i\perp}}{(2\pi)^2} R_1(q_{i\perp}, s) \right) \cdot (2\pi)^2 \delta^2 \left(\sum_{i=1}^n q_{i\perp} - \Delta \right) . \quad (6.23)$$

As for X_3 it is given by the lowest order two-Reggeon exchange amplitude like Fig. 9(e), with the gluon-Reggeon coupling described by the Lipatov vertex given in equ. (3.3).

Hence the color singlet component X_2 and X_3 gives the 6th order BFKL Pomeron, and the color singlet component of X_4 gives the lowest order Odderon [19, 49].

Chapter 7. High order calculation

If the sum of Feynman diagrams can be interpreted as given by n -Reggeon exchanges, then equ. (4.11) has to be satisfied for the sum. However, as discussed in the Introduction, the effective coupling constant is $g^2 \ln s$, so that a $(2k)$ th order Feynman diagram can contribute an amount $g^2 (g^2 \ln s)^{(k-1)}$, which is much bigger than $(g^2)^n (\ln s)^{(k-n)}$ in the region $g^2 \ll 1$. This means that a tremendous amount of cancellation must take place to yield a multi-Reggeon ($n > 1$) amplitude when Feynman diagrams are summed. We have seen how this occurred in the 6th order calculations of the last chapter for $n = 2$ and $n = 3$. If calculated directly, it means that each Feynman diagram must be computed to the accuracy of equ. (4.11), and not just to the leading-log precision. This is an extremely difficult task, so it is almost impossible to calculate the multi-Reggeon contributions directly in the usual way, much less showing whether they factorize into products of single-Reggeon amplitudes or not. This difficulty is however not present in the non-abelian cut diagram approach, for these cancellations have effectively taken place already to form each non-abelian cut diagram. In fact, we will show that a non-abelian diagram with $n - 1$ cuts has an energy dependence bounded above by equ. (4.11).

To prove this statement, first we look at a complementary cut diagram with $n - 1$ uncut propagators (on the top line). Using Fig. 18, such color diagrams can always be reduced to those with at most n gluon exchanges. Now the corresponding space-time diagram has $n - 1$ cut propagators. Remember from App. B that the $\ln s$ factor comes from the “—” integration of the Feynman propagator, and this $\ln s$ factor would be absent if the Feynman propagator is replaced by a δ -function. Therefore, a cut diagram with $(n - 1)$ cut propagators eliminate $n - 1$ potential $\ln s$ factors, so the corresponding space-time diagram contributes at most like $g^{2n}(g^2 \ln s)^{(k-n)}$, the same as equ. (4.11). If all the possible $\ln s$ factors in an s -channel ladder diagram are present in the amplitude, we call it a saturated diagram, otherwise, the diagram is unsaturated. As proven in App. B, diagrams without adjacent uncut lines are saturated, the others are unsaturated. Only the former ones are needed in leading-log computations; the latter ones can all be ignored in the discussion of this chapter.

In what follows, we shall use the abbreviation SC for s -channel ladder cut diagram, and the notation SCC for s -channel ladder complementary cut diagram.

For $(2k)$ th order amplitude, there are $k!$ s -channel ladder Feynman diagrams. Since there is a one-to-one correspondence between Feynman diagrams and cut diagrams, the number of SC is also $k!$.

One way to obtain all these $k!$ SC is to label the gluons attached to the lower line in the order $[123 \cdots k]$, then the order of the gluons along the top line can be used to specify the whole SC diagram. The $k!$ different SC diagrams correspond to

all possible permutations of these k gluons. Cuts on a SC diagram is determined by the rule introduced before, *i.e.*, they are placed behind a number if and only if there is not a smaller number to its right. Some 8th order SC diagrams are shown in Fig. 30 as illustrations.

For easier description for the factorization, we introduce another way to describe the diagrams. We can start from the planar diagram and obtain the others by pulling the upper ends of some gluon lines *leftward* in all possible ways. It is obvious that we can restore the $k!$ possibilities in doing that. The only question is where to put the cuts. The planar diagram has all its propagators on the top line cut, which can be understood if we still imagine that we number the gluon lines as before. As for the other SC diagrams, once a gluon line is moved leftward, the moved line has a larger number than the new neighbor to its right. Therefore, according to the multiple commutator rule, the propagator to its right should be uncut. Hence, when a gluon line is moved, the cut to its right disappears. Using this rule, we can actually forget about the numbers labeling the gluon lines. Fig. 30 can be used again as illustration about how this works. This time we do it as if the numbers were not there. We can start from the planar diagram Fig. 30(a). As a convention, we always keep all the gluon lines a planar diagram *vertical*. Fig. 30(a) is already drawn in such a way. When the upper end of a gluon line is moved, it becomes *slanted*. A SC diagram usually contains slanted lines and vertical lines. According to the rule above, the propagator to the right of a slanted line is uncut, but every other propagator is cut.

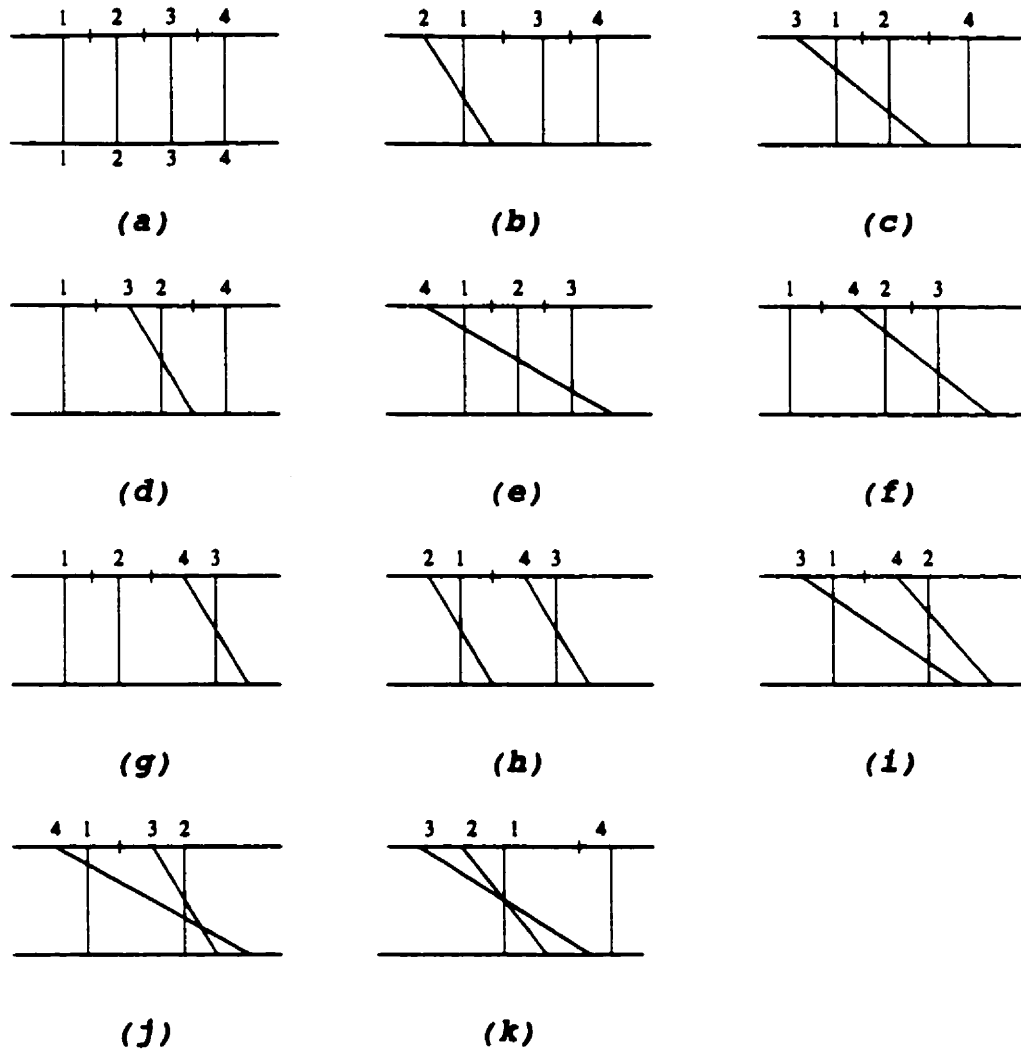


Figure 30: Examples of 8th order SC diagrams.

Since a saturated diagram cannot have two adjacent uncut lines, diagrams with two slanted lines adjacent to each other along the top line are unsaturated and can be ignored. For a saturated SC diagram, the neighbor to the right of a slanted line along the top line must always be a vertical line. Together they form a *skeleton cross*. The rest of the vertical lines have cuts on both sides, or a cut on one side and an external line on the other side. Because of the commutability resulting from the cuts, the upper end of these lines can be moved without affecting the amplitude of the SC diagram. For this reason, these vertical lines are called *mobile lines*. In contrast, the lines that form skeleton crosses are called *skeleton lines*. Skeleton lines have one cut propagator, or external line on one side, and an uncut line on the other side. The propagator inside the skeleton cross is always uncut for a SC diagram. According to the complementary rule, we can determine the corresponding SCC diagram as having cuts inside the skeleton crosses, and not cut elsewhere.

We will call vertical skeleton lines *v*-lines, slanted skeleton lines *s*-lines, and mobile lines *m*-lines. We label these lines respectively as $v_i, s_i (1 \leq i \leq k)$, and $m_j (1 \leq j \leq b = n - 2k)$ for different *m*. Here *n* is the total number of the gluon lines, and *k* is the total number of skeleton crosses. Because of the mobility of the *m* lines, and the skeleton crosses, the order of the *m* lines and the skeleton crosses along the top line are not important. We shall then use the order along the lower line to specify SC diagrams and SCC diagrams. Therefore a SC diagram is always

in the set

$$\mathcal{S}'_{k,b} \equiv \{v_1 s_2; v_2 s_2; \dots; v_k s_k; m_1; m_2; \dots; m_b\}. \quad (7.1)$$

Note that any permutation of the k skeleton crosses and the b mobile lines will give the same diagram, therefore the number of distinct diagrams is only $(2k+b)!/2^k k! b!$.

We then denote the set of distinct diagrams by $\mathcal{S}_{k,b}$. It contains the diagrams which are in $\mathcal{S}'_{k,b}$ and satisfy the rule that $v_1 < v_2 < \dots < v_k$, and $m_1 < m_2 < \dots < m_b$. We use $a < b$ to denote that line- a is to the left of line- b along the lower line.

7.1 Color factors

We have already learned how to decompose a SCC diagram into planar color factors, what we want to know now is the inverse procedure: how to find all the SCC that contain a given planar color factor.

To do that, we need to introduce several new conventions first. We define *primitive color factors* as color factors that remain connected after the upper and lower lines are removed. For example, Fig. 9(a), (e), (k) and (l) are primitive, but others in the same figure are not. We shall prove in App. C that in the leading-log approximation, every color factor that has the same number of primitive color units can be considered to be the same, no matter where the units are located. Therefore, 9(f) is the same as 9(g), and 9(i) is the same as 9(j). The complete color factor is given by $\Phi = \prod_{\alpha} \phi_{\alpha}$.

The primitive color factor of 9(a) will be denoted as I . The primitive color factor of (e) will be denoted as H . Therefore, the color factors of 9(b), 9(c), 9(d), 9(f), 9(g), 9(h), 9(i), 9(j) are then be written as $I^2, I^3, HI, HI^2, H^2, H^3$. Translated into the notation used in Chapter VI, $I = G_1, H = G_2, I^2 = G_3, \text{ and } I^3 = G_4$.

Now we review briefly how to decompose a SCC diagram into a summation of color factors. The main task is to uncross the gluon lines that overlap. We use the graphical commutation relations shown in Fig. 18 to move the lower end of a s -line leftward, until it comes to the right of the corresponding v -line, thus forming a skeleton cross with the s -line. We call this the *home position*. Operations like this decompose a SCC diagram into a sum of many *reduced diagrams*, each of which have the bottom end of any s -line lying to the left of their original positions, or has a cut to the right along the lower line. An s -line at the home position may or may not have such a cut; both situations are allowed. In addition, each reduced diagram is weighted with a minus sign if there are an odd number of cuts. Fig. 31 is an illustration.

If we remove the upper line and the lower line, the color factor of a reduced diagram may or may not be *connected* after we use the commutation relations to remove all the cuts. Those shown in Fig. 32 are connected and the one shown in Fig. 33 is not.

To judge connectivity of a reduced diagram, we can consider the cut in a SCC as a device to agglutinate together the pair of gluon lines it connects. Cuts on the

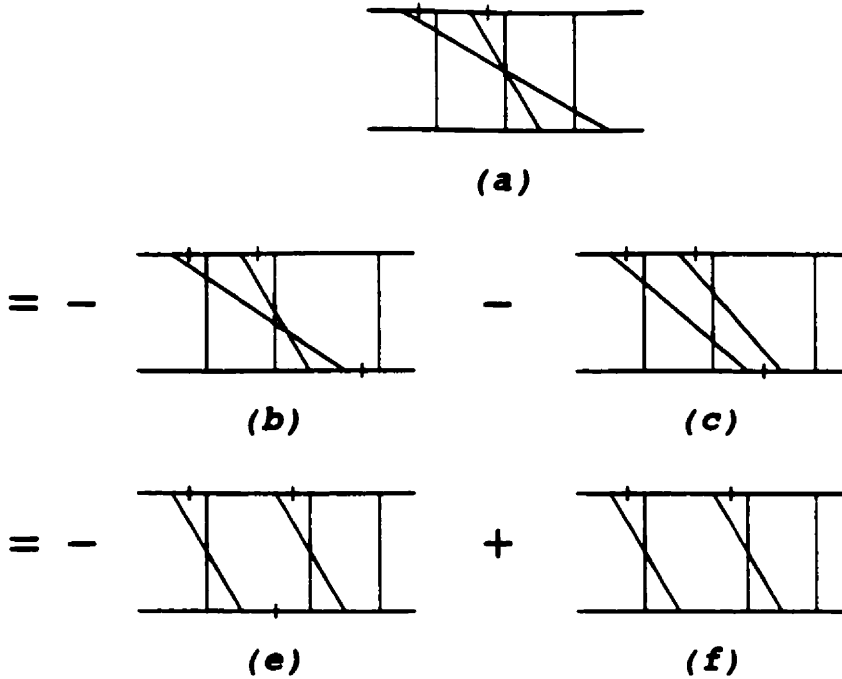


Figure 31: An example of the decomposition of SCC diagrams into sums of reduced diagrams.

upper line merge the upper ends of gluon lines, while cuts on the lower line merge the lower ends of gluon lines. Since the cuts on the top lines are always between the skeleton cross, thus we can determine the connectivity of a reduced diagram by only looking at the lower line. For example, the reduced diagram shown in Fig. 32(c) can be written as $[vs|m]$ according to the convention above. By only looking at this expression, we know that the v -line and the s line are connected because they form a skeleton cross, and the m -line is agglutinated to them by the cut. Therefore, it is a connected diagram.

The color factor of a disconnected reduced diagram is given by the product of the color factor of its connected components, according to the discussion above. So, in the following we shall focus on the discussion of the connected components.

The color factor of a connected component may or may not be primitive, depending on whether it is one of those shown in Fig. 32. The color factors in Fig. 32 are primitive, while those in Fig. 34 and Fig. 35 are not. Fortunately, it can be shown in App. C. that all non primitive color factors turn out to be zero, therefore we donot need to worry about them, at least for SCC diagrams.

All the primitive color factors encountered in SCC diagrams are collected in Fig. 32, together with those similar to Fig. 32(d) but with $p > 2$ skeleton crosses. Fig. 32(c) shows a structure like an H , and Fig.32(d) looks like two H 's merging together. So p is used to denote the number of H . Specially, Fig.32(a) and (b) donot look like H at all, and they are called H_{-1} and H_0 respectively. Also we can see that $p \geq 0$ is also the number of the horizontal gluon lines. By definition, $p = -1$ also means 0 horizontal gluon line. A primitive color factor has p horizontal gluon lines ($p \geq -1$), and the horizontal gluon line to the right is always located at a higher level. Thus we can denote these color factors by H_p , with $p = -1, 0, 1, 2 \dots$ (see Fig. 32 for illustration).

The primitive color factor defined before and shown in Fig. 32 can be written as the following cut tree along the lower line.

$$[H_{-1}] = [m]$$

$$[H_0] = [vs]$$

$$[H_1] = [vs|m]$$

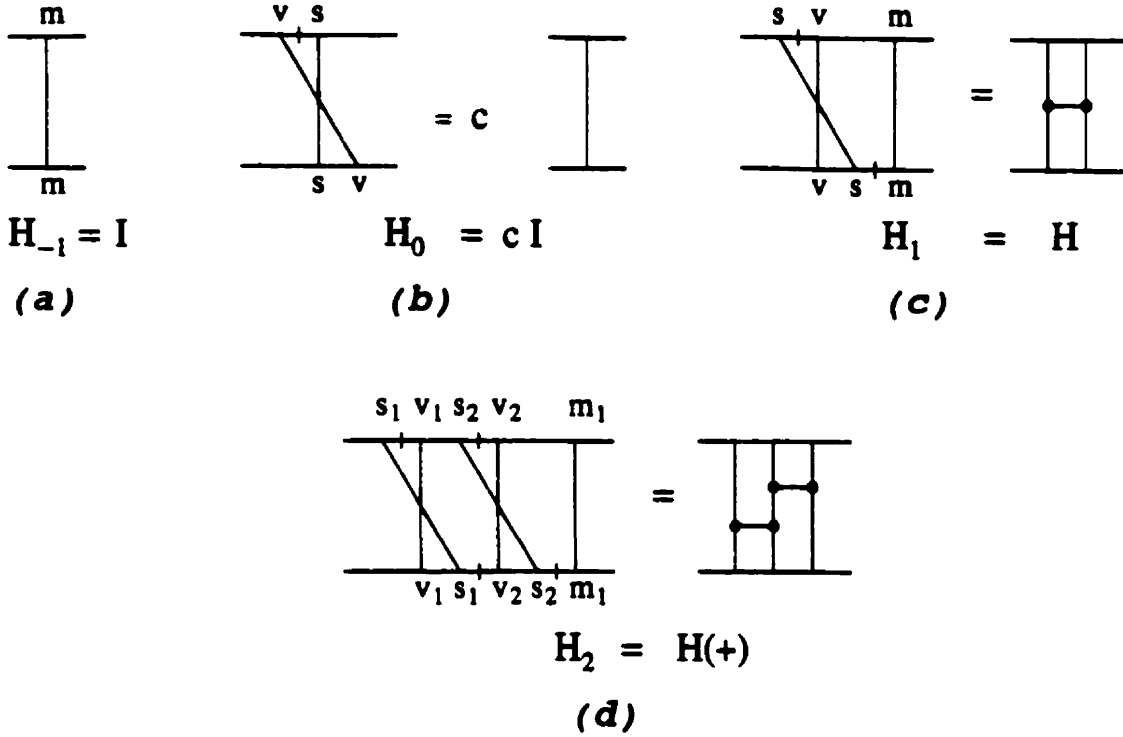


Figure 32: Examples of how primitive color factors are obtained from reduced components.

$$[H_2] = [v_1 m_1 | m_1 v_2 s_2 | m_2]$$

$$[H_p] = [v_1 s_1 | m_1 v_2 s_2 | m_2 \cdots v_p s_p | m_p], \quad (p \geq 1) \quad (7.2)$$

Given a regge color factor $\Phi = \prod_{p \leq -1} [(-1)^p H_p]^{f_p}$, we can obtain the reduced diagrams that contribute to this color factor by interleaving f_p copies of $[H_p]$ together in all possible ways. We can write

$$\{\Phi\} = \left\{ \prod_p (-1)^{p f_p} H_p^{f_p} \right\} = \{ [H_{-1}]; \cdots; [H_0]; \cdots; [H_1]; \cdots; [H_2]; \cdots; \cdots \} \frac{1}{\prod_p f_p!}, \quad (7.3)$$

where the ellipses after each $[H_p]$ is an instruction to repeat the same $[H_p]$ f_p times, separated by semicolons. The notation in the above equation for interleaving the cut trees in C_0 is similar to the notation $\{T_1; T_2; \cdots\}$ explained in Sec. V for interleaving

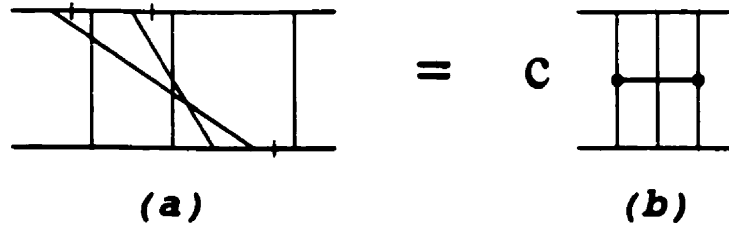


Figure 33: An example of a disconnected reduced diagram and the corresponding regge color factor.

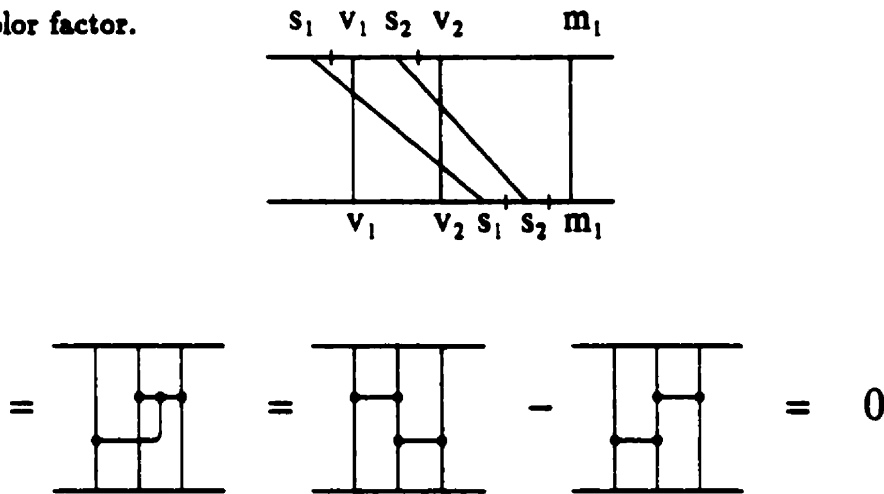


Figure 34: An example of a connected reduced diagram that is not primitive.

uncut trees T_i . But there are two differences needed to be noticed. First, lines separated by cuts should be thought of as being agglutinated by the cuts, so lines from other cut trees can never be inserted between them. Secondly, each cut diagram in $\{[H_p; \dots]\}$ repeats $f_p!$ times because of the identical nature of these diagrams. Since we allow only distinct diagrams in $\{\Phi\}$, the division by $\prod_p f_p!$ in equ. (7.3) is a formal way to remove such overcounting.

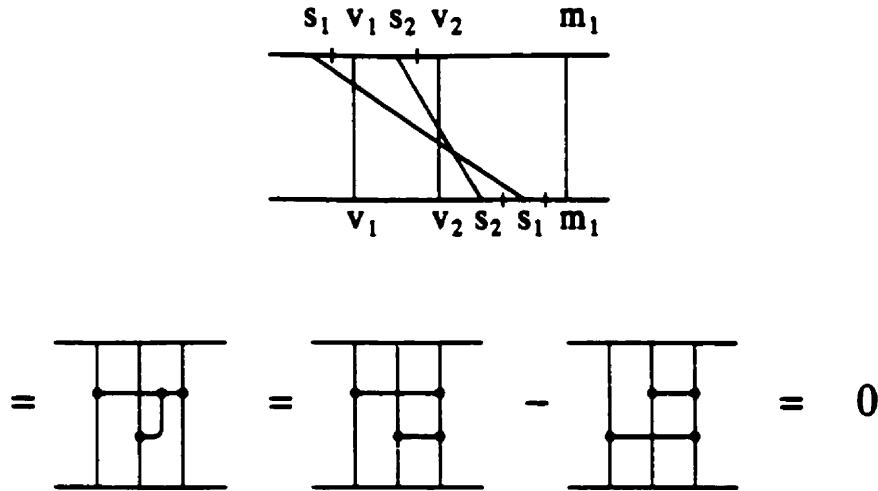


Figure 35: Another example of a connected reduced diagram that is not primitive.

The SCC diagrams in \mathcal{S} that contain the reduced diagrams in $\{\Phi\}$ will be denoted $\{\Phi\}_{\mathcal{S}}$. They can be obtained from the cut trees in $\{\Phi\}$ by getting rid of their cuts, which can be accomplished by moving the s -line rightward in all possible ways. Instead of first interleaving the cut trees $[H_p]$ and then getting rid of the cuts, $\{\Phi\}_{\mathcal{S}}$ can also be obtained by reversing the two operations by first removing the cuts and then interleaving the uncut trees, as discussed below in detail.

We can start from $[H_p] \in \mathcal{C}_0$, and remove the cuts by moving the s -lines rightward, to construct all $h_p^i \in \mathcal{S} (i = 1, 2, \dots)$ that reduce to $[H_p]$. In cases like Fig. 32(a) to 32(c) where there is only one tree for each $[H_p]$, the degeneracy index $i = 1$ will be omitted. This index is however needed in other cases. For example, $[H_2] = [v_1 s_1 | m_1 v_2 s_2 | m_2]$ in Fig. 32(d) gives rise to the uncut trees $h_2^1 = [v_1 m_1 s_1 v_2 m_2 s_2]$,

$h_2^2 = [v_1 s_1 v_2 s_2 m_1 m_2]$, $h_2^3 = [v_1 m_1 v_2 m_2 s_1 s_2]$, and $h_2^4 = [v_1 m_1 v_2 m_2 s_2 s_1]$. The set of all $h_p^i \in S$ for a fixed p will be denoted by $\{H_p\}_S$.

7.2 Factorization of sums of spacetime amplitudes

We continue to compute the sum of corresponding spacetime amplitudes of all saturated SC diagrams with a common regge color factor $\Phi = \prod_p ((-1)^p H_p)^{f_p}$. The relevant spacetime diagrams are those in the set $\{\Phi\}_S$.

Using the factorization formula for the lower tree, we can get

$$a\{\Phi\}_S = \sum_{[T] \in \{\Phi\}_S} a[T] = \sum_p \frac{1}{f_p!} (a\{H_p\}_S)^{f_p}, \quad (7.4)$$

where

$$\frac{1}{f_p!} (a\{H_p\}_S)^{f_p} \equiv \frac{1}{m_i!} (a\{h_p^i\})^{m_i}, \quad (7.5)$$

with the sum taken over all $m_i \leq 0$ subject to $\sum_i m_i = f_p$. Therefore, $a\{H_p\}_S = \sum_i a\{h_p^i\}$. The factorials in the denominators of equ.(7.4) arise because of the necessity to keep only distinct diagrams in $\{\Phi\}_S$.

The factorization in equ. (7.4) and (7.5) for the lower tree can also be applied to the SC amplitudes. To do this we need to make explicit use of the cut property of the upper tree, that the only uncut propagators are those between the two lines forming skeleton crosses. Let us first look at an example as an illustration. In Fig. 36, both (a) and (b) belong to the the set $\{231; 564\}$, but if we keep the upper ends of the gluon lines fixed in Fig. 36(a) and (b), permuting the lower ends of the

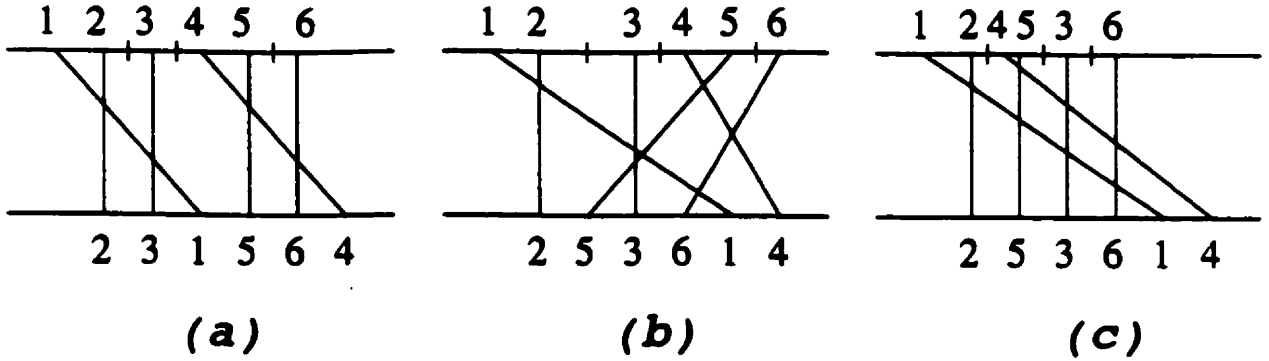


Figure 36: An example of re-organizing diagrams.

lines to get from 326(a) to 36(b) does not change the SC diagram Fig. 36(a) back to another SC diagram. Fig. 36(b), with lines 5 and 6 slanting the wrong way, cannot be an SC diagram. However, by making explicit use of the commuting properties of the amplitude of the upper tree, $a[12|3|44|6] = a[12]a[3]a[45]a[6] = a[12|45|3|6]$, Fig.36(b) can be redrawn as Fig.36(c), which is a legal SC diagram. This can always be done so that factorization of the lower tree really leads to a factorization of the sum of saturated SC amplitudes.

Now we deal with the gluon propagators, quark propagators, vertex factors, and loop integrations. In light-cone coordinates, the measure of loop-integration is

$$\frac{d^4 q}{(2\pi)^4} = \frac{d^2 q_\perp}{(2\pi)^2} \frac{dq_+ dq_-}{8\pi^2}. \quad (7.6)$$

We assume that the Dirac spinors are normalized to $\bar{u}u = 1$, and a common factor is taken out of the T -matrix amplitude $\mathcal{T} = -(s/2M^2)\mathcal{A}$, then each factorized amplitude $a\{H_p\} = \sum_i a_i[h_p^i]$ corresponds to a saturated SC amplitude $\mathcal{A}\{H_p\}_s(\Delta) = \sum_i \mathcal{A}[h_p^i](\Delta)$, where we have indicated explicitly the dependence on

the momentum transfer Δ . The product of two lower tree amplitudes $a\{H_a\}a\{H_b\}$ is turned into a convolution of two SC amplitudes:

$$[\mathcal{A}\{H_a\}_s * \mathcal{A}\{H_b\}](\Delta) \equiv (-i) \int \frac{d^2 q_\perp}{(2\pi)^2} [\mathcal{A}\{H_a\}_s](\Delta - q_\perp) [\mathcal{A}\{H_b\}](q_\perp). \quad (7.7)$$

In obtaining the above equation, we have used the identity

$$i \int \frac{dq_+ dq_-}{8\pi^2} (-2\pi i)^2 \delta(\sqrt{s}q_+) \delta(\sqrt{s}q_-) (2s) = -i. \quad (7.8)$$

The sum of all saturated SC amplitudes with the regge color factor Φ is then given by

$$[\mathcal{A}\{\Phi\}_s](\Delta) = \prod_p \frac{1}{f_p!} [\mathcal{A}\{H_p\}_s]^{*f_p}(\Delta). \quad (7.9)$$

All the products in the above equation are meant to be convolutions. In particular, $[\mathcal{A}\{H_p\}_s]^{*f_p}$ is taken to mean f_p convolutions of the same amplitude. In the impact-parameter space, such convolutions are replaced by simple products.

Therefore, we have proved in this chapter the factorization of the s-channel diagrams.

Chapter 8. Conclusion

In the leading logarithm approximation of perturbative QCD, only the 2-Reggeon exchange amplitude contributes to the quark-quark forward elastic scattering amplitude. The resulting BFKL Pomeron amplitude violates unitarity at the asymptotic limit. This reveals the importance of going beyond the leading logarithm ($n > 2$ in equ. (4.11)) in order to unitarize the BFKL Pomeron. If all these subleading contributions can be summed and interpreted as multi-Reggeon exchange amplitudes, then unitarity can be restored.

Cheng and Wu first demonstrated by direct calculation up to 6th order [28] that multi-Reggeon exchange can be obtained by summing Feynman diagrams. They also showed that the multi-Reggeon exchange amplitude factorizes in the impact parameter space into products of single Reggeon amplitude. Unfortunately, it is hard to apply these methods to higher order calculations because of difficulties encountered in the usual techniques. One of these difficulties comes from the fact that the leading contributions of individual Feynman diagrams tend to have higher powers of $\ln s$ than the one given in equ. (4.11). Therefore if multi-Reggeon exchanges can be obtained from Feynman diagrams, these extra powers of $\ln s$ must all get cancelled in their sum. In order to get a finite sum, we are forced by the usual techniques to keep subleading, or even subsubleading, contributions in computing individual Feynman

diagrams. This kind of cancellation can already be seen at the 4th and 6th order in the multi-Reggeon channels as shown by the direct calculations of Cheng and Wu [28]. Although the desired subleading contributions can be successfully obtained in an ingenious way at these orders, they become so difficult in higher orders that even the 8th order calculations were only partially finished using the usual techniques.

That is one of the motivations for introducing non-Abelian cut diagrams. As shown in the previous chapters of this thesis, the difficulty mentioned above is circumvented in a non-Abelian cut diagram approach. The reason is that the leading contribution of a non-Abelian cut diagram can be shown to be bounded above by equ. (4.11), therefore there is no need for cancellation to occur, so we only need to compute the leading contribution of each cut diagram. In other words, the cancellations have already been taken into account in forming individual cut diagrams. This greatly simplifies the calculations.

The s -dependence of either a Feynman diagram or a non-Abelian cut diagram comes from the longitudinal integrals in the momentum space. Contour integrations are used in their evaluations. Cheng and Wu invented *flow diagrams* [28] to identify the contributing poles for these contour integrations. In this thesis we have extended their technique by introducing the path method. Our technique greatly simplifies the extraction of the s -dependence of multi-loop diagrams.

Both these techniques have been used to confirm the existing result up to the 6th order, and to illustrate the relative simplicity of the new methods. To exam-

ine whether multi-Reggeon exchanges emerge from higher order diagrams, and if so whether the multi-Reggeon amplitudes factorizes or not, we have chosen to investigate the problems in a class of Feynman diagrams (s -channel ladder diagrams). We have shown that multi-Reggeons do emerge, and that their amplitudes indeed factorize as hoped. Such properties are crucial for the unitarization of the BFKL Pomeron amplitudes, as discussed in the Introduction.

In this thesis, we have not attempted to show the presence of multi-Reggeons, nor the factorization of their amplitudes, beyond the 6th order and beyond the s -channel ladder diagrams. Neither have we demonstrated for QCD how factorization of multi-Reggeon amplitudes leads explicitly to unitarization as we did for QED in Chapter IV. These problems have been partially solved recently[18] using the new techniques developed in this thesis.

A Multiple commutator formula

To prove equ. (5.6), we first need to prove another one: folding formula, which is expressed as follow:

$$a[LSR] = \sum_{k=0}^N (-1)^k a\{L; \bar{\sigma}_{1,k} \cdot s\} a[\sigma_{k+1,N}] \equiv \sum_{k=0}^N (-1)^k a\{L; \bar{\sigma}_{1,k} \cdot s | \sigma_{k+1,N}\} . \quad (\text{A.1})$$

The notations we used are explained in the following. $[LSR]$ is a tree containing a subtree L , a line $[s]$, and another subtree $[R]$. N is the total number of lines included in tree $[R]$. $\sigma_{i,j}$ is a subtree of $[R]$ containing the i th line to j th line. Specially, $\sigma_{1,0}$ and $\sigma_{N+1,N}$ are defined to be null tree $[0]$. Also $a[0] \equiv 1$. The notation $\bar{\sigma}_{1,k}$ means the tree $\sigma_{1,k}$ read in the reverse order. Therefore, if $[R] = [28137546]$, then $\sigma_{1,5} = [28137]$, $\sigma_{6,8} = [546]$, and $\bar{\sigma}_{1,5} = [73182]$. Another notation appearing in the above equation $\{T_1; T_2; \dots; T_A.t\}$ means the following. $[t]$ is an arbitrary tree, which may or may not have cuts. The above symbol denotes the set of tree $[Tt]$ for all the $[T] \in \{T_1; T_2; \dots; T_A\}$. We also used $a\{T_1; T_2; \dots; T_A.t\}$ to denote the sum of all these amplitude $a[Tt]$.

The above idenity re-expresses the original amplitude $a[LSR]$ as sums of products of amplitudes, in each of which line- s is moved to the end of the tree. This reshuffling will enable us later to resum the nonabelian diagrams into cut diagrams.

The folding formula is also called cutting and folding formula. It can be graphi-

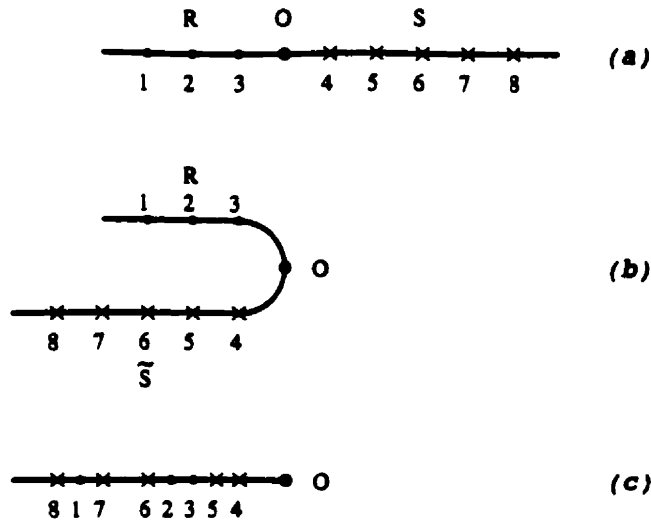


Figure 37: Folding formula.

cally explained as shown in Fig. 37. We first cut off the the tree $\sigma_{k+1,N}$ at the end of $[LsR]$, and then fold the remaining tree about the point s . Finally, both branches of the folded tree should be interleaved to obtain the trees $\{L; \tilde{\sigma}_{1,k,s}\}$.

Now we proceed to prove this formula using induction. First we look at $N = 1$. Remember N is the length of the tree R . For $N = 1$, we can write the formula explicitly. The left hand side is $a[LsR]$, and the right hand side can be written as

$$a[Ls|R] - a\{L; R.s\} = a\{Ls; R\} - a\{L; R.s\} . \quad (\text{A.2})$$

From the definition of the *cut*, we can easily recognize that the first term of the right side can be written as $a[LsR] + a\{L; R.s\}$. Subsitute this back to the above equation, we can see that the folding formula holds for $N = 1$. Assuming it is true for $N \leq m - 1$, and we need to prove it is true for $N = m$.

We start from equ. (A.1), and assume that $R = [t_1 t_2 \cdots t_m]$

$$a\{Ls; \sigma_{1,m}\} = a[Ls]a[\sigma_{1,m}] . \quad (\text{A.3})$$

where $\sigma_{p,q} = [t_p t_{p+1} \cdots t_q]$. The left hand side of the above equation can be rearranged as summation according to number k of lines in R appearing to the left of line- s . So that the above equation can be written as

$$a[Ls]a[R] = a[LsR] + \sum_{k+1}^m a\{L; \sigma_{1,k} \cdot s \sigma_{k+1,m}\} . \quad (\text{A.4})$$

Now for $k \leq 1$, there are at most $(m-1)$ lines to the right of s . Therefore, for each individual amplitude appearing in the summation of the right hand side above, we can apply the induction hypothesis. Then the second can be written as

$$a\{L; \sigma_{1,k} \cdot s \sigma_{k+1,m}\} = \sum_{l=0}^{m-k} (-)^l a\{L; \sigma_{1,k}; \bar{\sigma}_{k+1,k+l} \cdot o\} a[\sigma_{k+l+1,m}] . \quad (\text{A.5})$$

Putting this back into equ. (A.4), we can obtain

$$a[LsR] = a[Ls]a[R] - \sum_{k=1}^m \sum_{l=0}^{m-k} (-)^l a\{L; \sigma_{1,k}; \bar{\sigma}_{k+1,k+l} \cdot o\} a[\sigma_{k+l+1,m}] . \quad (\text{A.6})$$

Introducing a new variable $k' = k + l$ and change the order of summation, we get

$$a[LsR] = a[Ls]a[R] - \sum_{k'=1}^m (-)^{k'} a[\sigma_{k'+1,m}] \sum_{k=1}^{k'} (-1)^k a\{L; \sigma_{1,k}; \bar{\sigma}_{k+1,k'} \cdot o\} \quad (\text{A.7})$$

The summation over k can be simplified by using the relation

$$\sum_{k=0}^{k'} (-)^k a\{L; \sigma_{1,k}; \bar{\sigma}_{k+1,k'} \cdot o\} = 0 , \quad (\text{A.8})$$

which will be proven later. Now equ. (A.7) becomes

$$a[LSR] = a[LS]a[R] + \sum_{k'=1}^m (-)^{k'} a\{L; \bar{\sigma}_{1,k'.o}\} a[\sigma_{k'+1,m}], \quad (\text{A.9})$$

which is just the $N = m$ case for the folding formula.

Let us go back to prove equ. (A.8). We use $a < b$ to mean line- a lying to the left of line- b in a tree. We can ignore L and s first. Look at a tree $T_k = \{\sigma_{1,k}; \bar{\sigma}_{k+1,k'}\}$, all the lines on it obey the order $t_1 < t_2 < \dots < t_k$, and $t_{k'} < \dots < t_{k+1}$. Because the semicolon means interleaving, so that in $(-)^k a\{T - k\}$ there are two kinds of terms: $t_k > t_{k+1}$ or $t_k < t_{k+1}$. The first kind of terms will be cancelled by similar terms in $(-)^{k-1} a[T_{k-1}]$, and the second kind of terms will be cancelled by similar terms in $(-)^{k+1} a[T_{k+1}]$. Specially, the terms in $k = 0$ are completely cancelled by terms in $k = 1$, and terms in $k = k'$ are completely cancelled by terms in $k = k' - 1$. Therefore, we have proven that equ. (A.1) is true, and finish the proof of the folding formula. Adding in L and o does not affect the proof above.

The next step is to use the folding formula to prove the multiple commutator formula. Take any Feynman daigram (the space-time part). Use the folding formula to cut and fold, so as to move the number '1' to the end. What we get is a product of two $a[\dots]$, the first one having '1' at the end, and the second one not containing "1". Apply the folding formula again on the second $a[\dots]$, and this time move the smallest number in its argument to the right most end. Continue this process, and the final result will be sum of products of several $a[\dots]$, each of which has the smallest

number in its argument being at the right most end. Recalling the definition of a cut, we can immediately recognize that each term in the sum satisfies the cut rule for space time diagram.

Now we can see that each Feynman diagram (space-time part) corresponds to a sum of several cut diagrams. There is still the color part we need to deal with. What we need to do is to organize the sum of diagrams according to the space-time cut diagram, or say, for certain cut diagram $a[\rho]_c$, we need to find out all the Feynman diagrams that contribute to it. Thus we need to unfold the tree $[\rho]_c$. If there is not cut on $[\rho]_c$, it will be of the form $\rho]_c = [\tau 1]$. Then we find all the τ_i that satisfies $[\tau 1] \in \{\tau_1; \tau_2.1\}$, and unfold the tree to get $[\sigma] = [\tau_1 1 \tau_2]$. The sign involved is $(-)^k$, where k is the number of lines in tree $[\tau_2]$. We sum up all the possibilities and get the color factor associated with this space-time cut diagram as $\sum (-)^k t[\tau_1 1 \tau_2]$, which can be recognized as the multiple commutator $t[\rho]'_c$. If $[\rho]_c$ has explicit cuts, then we can use the above way to deal with each of the cut sections, and obtain a multiple commutator of the color factor for each section. This then finishes the proof of the multiple commutator.

B Spacetime amplitudes

Assume that there are n -gluon connected to the upper fermion line. The incoming fermion carries on-shell momentum $p_1 = (\sqrt{s}, 0, 0)$, while the outgoing fermion car-

ries on-shell momentum $p'_1 = (\sqrt{s}, 0, \Delta)$. The energy of each gluon is far less than \sqrt{s} . At high energy, the numerator of a fermion can be written as

$$\begin{aligned}\gamma \cdot p &= 2m \sum_{\lambda} u_{\lambda}(p_1) \bar{u}_{\lambda}(p_1), \\ \bar{u}_{\lambda}(p) u_{\lambda'}(p) &= \delta_{\lambda\lambda'}.\end{aligned}\tag{B.10}$$

Then each fermion vertex can be approximated by $2p_1^{\mu}$, and each fermion line has an overall normalization factor $1/(2m)$.

Based on the above approximation, to calculate a Feynman diagram, we can either use Feynman-parameter representation [47] as done by Cheng and Wu [28], or use light-cone coordinates in momentum space. We choose the latter approach here. Using the same convention as in Ref. [28], we assume that the momentum of the incoming fermion on the top contains only + component, and the momentum of Incoming fermion on the bottom contains only - component. Calculations using this approach follows three steps:

1. use residue calculus to carry out the + momentum integrations;
2. carry out the - component integration to obtain the $\ln s$ dependence;
3. express the transverse momentum integrations in terms of I_n and J_n .

We always close integration contours in the lower half planes. The contributing poles are given by the path method. For a scalar diagram, the \mathcal{T} -matrix element equals to the product of J propagators $D^{-1} = (q^2 - m^2 + I\epsilon)^{-1}$, integrated over the

l loop momenta $d^4 k_a = \frac{1}{2} dk_+ dk_- d^2 k_\perp$, with an overall numerical factor $-[i/2\pi]^{4l}$.

Since there is a factor $-2\pi i$ from each '+' integration, the \mathcal{T} -matrix is given by

$$\mathcal{T} = - \sum \int Dk_\perp \left(\prod_{a=1}^l \frac{dk_{a-}}{4\pi} \right) \frac{1}{\prod_{i=1}^J D_i}, \quad (\text{B.11})$$

where

$$Dk_\perp \equiv \prod_{a=1}^l \frac{d^2 k_{a\perp}}{(2\pi)^2} \quad (\text{B.12})$$

is the measure for transverse momentum integration, and D_i is either the propagator evaluated at the contributing pole or the residue of the contribution pole.

Now we can calculate amplitude B2c. As shown in Fig. 38(a), we choose the momentum of line-1 to be k , and line-4 to be the contributing pole, then all the D_i can written as

$$\begin{aligned} D_1 &= p_1^-; \\ D_2 &= -(k_\perp + \Delta)^2; \\ D_3 &= -p_2^+ k^-; \\ D_4 &= -k_\perp^2; \end{aligned} \quad (\text{B.13})$$

The '-' integration only comes from D_3 , and we have

$$\begin{aligned} \int_0^{+\infty} \frac{dk_-}{k^-} &= \int_{a/s}^1 \frac{\sqrt{sdz}}{\sqrt{sz}} \\ &= \ln s. \end{aligned} \quad (\text{B.14})$$

Therefore the amplitude is given by

$$\mathcal{T} = \frac{I_2}{4\pi s}. \quad (\text{B.15})$$

Putting back the QED vertex and normalization factor $(2s)^2 g^4 / (2m)^2$, we get the result given in Chapter 6.

The next diagram we need to compute here is C2c. We label the propagators the same as in Fig. 27, and the momentum carried by each of them is given in Fig. 38(b).

Again, line 5 and line 11 are the contributing poles. All the D_i 's are listed below:

$$\begin{aligned}
D_6 &= p_1^- ; \\
D_8 &= -k_{1\perp}^2 ; \\
D_7 &= -\frac{(k_2)^-(k_{1\perp} - k_{2\perp})^2}{k_2^-} - (k_2)_\perp^2 ; \\
D_8 &= -p_2^+(k_2)^- ; \\
D_9 &= -\frac{(k_2)^-(k_{1\perp} - k_{2\perp})^2}{k_2^1} - (k_2)_\perp^2 ; \\
D_{10} &= -(k_{1\perp} + \Delta)^2 ; \\
D_{11} &= k_2^- . \tag{B.16}
\end{aligned}$$

As for the numerator N , after combine part of C22 following Ref. [28]. (A complete list of Feynman rules can be found in [50].) Then we have

$$\begin{aligned}
N &= -2s^2 / \text{ov} 2m^2 [(k_{1\perp} + k_{2\perp}) \cdot (k_{1\perp} + k_{2\perp} - 2\Delta) + (k_{1\perp} - k_{2\perp})^2] ; \\
&= -22s^2 / \text{ov} 2m^2 [k_{1\perp}^2 + k_{2\perp}^2 - \Delta \cdot (k_{1\perp} + k_{2\perp})] . \tag{B.17}
\end{aligned}$$

Thus the numerator is independent of k_1^- and k_2^- . As for the k_1^1 and k_2^- integrations, we can see that the leading contribution comes from the region

$$k_1, k_2 \gg k_1 - k_2 . \tag{B.18}$$

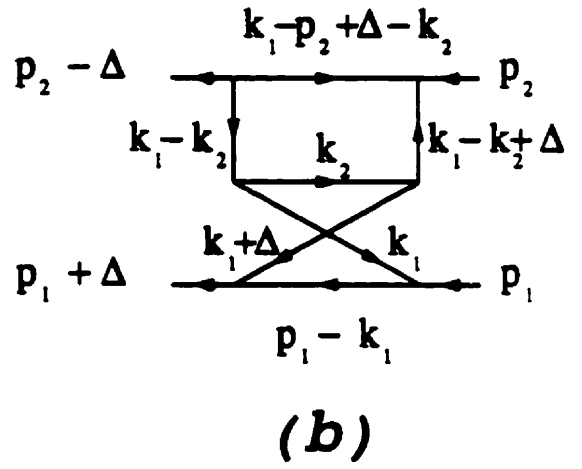
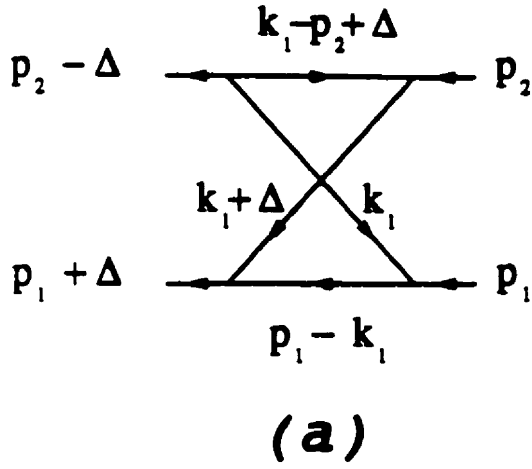


Figure 38: B2c and C2c

This gives us the final answer

$$\mathcal{T} = -\frac{g^4 s}{4\pi^2 m^2} (\ln^2 s) [\Delta^2 I_2^2 - J_2 I_2] . \quad (\text{B.19})$$

Now we want to prove in general that the diagrams with two adjacent uncut propagators on the top line is unsaturated, or say, is a diagram in lower order of $\ln s$ than the that shown in equ.(4.11).

For a s -channel diagram without adjacent uncut propagators on the top line, these is always only one flow diagram. For this flow diagram, the pole for the “+” integrations can always be taken along the lower line. After taken these poles, all the gluon propagators become $\sim 1/q_{i\perp}^2$, and can be considered to be $O(1)$. Then only the uncut propagator along the top line are relevant to the “-” integrations.

Each of these uncut propagators contributes a factor of $\ln s$ via “-” integration of the type $\int_{s_i-1} dx_i/x_i$. Therefore, such diagrams have their full share of $\ln s$ factors and are saturated.

For diagrams with two or more adjacent uncut line, there are always more than one flow diagrams corresponding to each of them, because the flow direction along the boundary of the two adjacent uncut loopw cannot be uniquely determined. This results in that at least one pole of the “+” integration must not come from the lower line. Explicit calculation then shows that such diagrams are at least one $\ln s$ down from the saturated ones.

The reason for this reduction can be traced back as follows. After the integration of “+” momenta, the “+” momentum of the pole lines can be estimated as inversely proportional to its “-” momentum. The “+” momentum for other lines can be then determined by momentum conservation. Since the large “-” momentum flows mainly along the lower line, a pole taken on a gluon line will have a relatively larger “+” component than a pole on the lower line. According to momentum conservation, there must a return flow passing through part of the lower line and another gluon line. The Feynman propagators of these lines are large due to the large “+” flow through them. This brings about at least two small factors of x_i , overcompensating the large factor from the residue of the pole. Therefore, at least a $\ln s$ factor will be lost from the “-” integrations as a result. This is the reason that these diagrams are unsaturated.

C Color factors of nonabelian cut diagrams

To get rid of a cut on a SCC diagram, we can use the rule presented in Fig. 18. As a result, a cut always eliminate the number of lines attached to the upper line, and diagrams with $m - 1$ uncut propagators along the upper line can have at most m gluon lines joined to it. Since cuts on a SCC diagram is always on the upper line, then after we eliminate them, the number of lines joined to the upper line m is usually smaller than the number of lines joined to the lower line n . This cannot be a regge color factor, since the reggeon exchanged between the two energetic fermion lines is conserved. But we have seen several cases that by using the rules in Fig. 18 again to manipulate the lines attached to the lower tree, we can reduce the lines attached to the lower line to be m .

It is possible that for very complicated diagrams we cannot reduce n to m using the rules in Fig. 18 alone. Then because of the conservation of the exchange reggeon, the resulting color factor with $n > m$ cannot contribute to the final answer if the reggeization proposal is true. Therefore, we shall define the leading-log approximation to exclude all such color factors that cannot be reduced to $n = m$.

Now we want to prove why Regge color factor with the same primitive color factors but in different positions are the same in leading-log approximation. Using the rule in Fig. 18, we can exchange the positions of gluon lines attached to the upper line or lower line, and the compensation for this exchange is a diagram with

using the same rule along the middle vertical line, we can see that (d) and (e) can also be combined to get (a). Using the above argument, we know that in the leading-log approximation, we can move the middle vertical line of Fig. 39 (d) and (e) to the right most position, and they remain the same color factors. This then tells us that $\text{Fig. 39(d)}=(c)$ and $\text{Fig. 39(b)}=(e)$. Hence $\text{Fig. 39(a)}=(b)-(c)=(c)-(b)=0$.

References

- [1] C. Zweig, CERN Rep. 8419/TH 412.
- [2] J.C. Collins and P.V. Landshoff, *Phys. Lett.* **B276**, 196 (1992);
A. Donnachie and P.V. Landshoff, *Phys. Lett.* **B296**, 227 (1992).
J.R. Cudell, A. Donnachie and P.V. Landshoff, *Nucl. Phys.* **B482**, 241 (1996).
- [3] P. Hoyer and C.S. Lam, *Z. Phys.* **C70**, 449 (1996);
M. Derrick et al. (ZEUS Koll.), *Phys. Lett.* **B315**, 481 (1993); *Z. Phys.* **C68**,
569 (1995); *Phys. Lett.* **332**, 228 (1994);
T. Ahmed et al. (H1 Koll.), *Nucl. Phys.* **B429**, 477 (1994); *Phys. Lett.* **B348**,
681 (1995);
C. Adloff et al. (H1 Koll.), *Z. Phys.* **C76**, 613 (1997); *Phys. Lett.* **B428**, 206
(1998).
- [4] C. Lopez and F.J. Yndurain, *Nucl. Phys.* **B171**, 231 (1980).

- [5] A. Donnachie and P.V. Landshoff, Nucl. Phys. **B267**, 690 (1986); Nucl. Phys. **B244**, 322 (1984);
 A. De Rujula et al., Phys. Rev. **D10**, 1649 (1974).
 J.R. Cudell, *A review of the soft Pomeron*, hep-ph/9512209 (1995).
- [6] A.H. Mueller, Nucl. Phys. **B415**, 373 (1994); Nucl. Phys. **B437**, 107 (1995);
 A.H. Mueller and B. Patel, Nucl. Phys. **B425**, 471 (1994);
 Z. Chen and A.H. Mueller, Nucl. Phys. **B451**, 579 (1995);
- [7] Y.V. Kovchegov, Phys. Rev. **D60**, 034008 (1999).
- [8] F.E. Low, Phys. Rev. **D12**, 163 (1975);
 S. Nussinov, Phys. Rev. Lett. **34**, 1286 (1975);
 J.F. Gunion and D.E. Soper, Phys. Rev. **D15**, 2617 (1977).
- [9] C. Itzykson and J. Zuber, *Quantum Field Theory*, McGraw-Hill Inc. (1980).
- [10] V.S. Fadin, E.A. Kuraev and L.N. Lipatov, Phys. Lett. **B60**, 50 (1975);
 L.N. Lipatov, Sov. J. Nucl. Phys. **23**, 338 (1976);
 Ya. Ya. Balitskii and L.N. Lipatov, Sov. J. Nucl. Phys. **28** 822 (1978);
 L.N. Lipatov, Sov. Phys. J.E.T.P. **63**, 904 (1986);
 L.N. Lipatov, *Pomeron in Quantum Chromodynamics*, in "Perturbative Quantum Chromodynamics" (A.H. Mueller, ed.), World Scientific, Singapore 1989;

A.R. White: *Int. J. Mod. Phys. A* **6**, 1859 (1990); *Nucl. Phys. B* **12**, 190 (1990);
Nucl. Phys. B **25**, 167 (1992);

J. Bartels, *Z. Phys. C* **60**, 471 (1992);

J.B. Bronzan and R. L. Sugar, *Phys. Rev. D* **17**, 585 (1978);

T. Jaroszewicz, *Acta. Phys. Polon. B* **11**, 965 (1980).

[11] L.N. Gribov, E.M. Levin and M.G. Ryskin, *Phys. Rep.* **100**, 1 (1983).

[12] B. Badelek et al., *Rev. Mod. Phys.* **64**, 927 (1992).

[13] A.D. Martin, *Acta. Phys. Polon. B* **25**, 265 (1994).

[14] J. Kwiecinski, *Nucl. Phys. B* **39** (Proc. Suppl.), 58 (1995).

[15] V.S. Fadin and L.N. Lipatov, *Phys. Lett. B* **429** 127 (1998);

M. Ciafaloni and G. Camici, *Phys. Lett. B* **430**, 349 (1998).

[16] V. del Duca, *NLL BFKL and NNLO*, hep-ph/9906278 (1999);

Z. Bern, V. del Duca, W.B. Kilgore and C.R. Schmidt, *The infrared behavior of QCD cross-sections at next-to-next-to leading order*, hep-ph/9903525 (1999).

[17] M. Froissart, *Phys. Rev.* **123**, 1051 (1961).

[18] R. Dib, J. Khoury, and C.S. Lam, *Phys. Rev. D* **60**, 036001 (1999)..

[19] L.Lukaszuk and B. Nicolescu, *Nuov. Cim. Lett.* **8**, 405 (1973);

- D. Joynson, E. Leader, C. Lopez, and B. Nicolescu, *Nuov. Cim.* **30**, 345 (1975).
- R.R. Janik and J. Wosiek, *Phys. Rev. Lett.* **79**, 2935 (1997); *Solution of the odderon problem*, hep-th/9802100 (1998), *Phys. Rev. Lett.* **82**, 1092 (1999); *New results on the odderon in QCD*, hep-th/9805135 (1998).
- P.V. Landshoff and O. Nachtmann, *Some Remarks on the Pomeron and the Odderon in Theory and Experiment*, hep-ph/9808233 (1998).
- [20] J. Bartels and M. Wuesthoff, *Z. Phys.* **C66**, 157 (1995);
- [21] E.A. Kuraev, L.N. Lipatov, and V.S. Fadin, *Zh. Eksp. Tero. Fiz.* **71** 840 (1976) [*Sov. Phys. JETP* **44** 443(1976)].
- [22] T. Cheng and L. Li, *Gauge Theory of Elementary Particle Physics*, Oxford University press, 1984.
- [23] H. Cheng and T.T. Wu, *Phys. Rev. Lett.* **22** 666 (1969); *Phys. Rev. Lett.* **24**, 1456 (1970).
- [24] C.Y. Lo and H. Cheng, *Phys. Rev.* **D13**, 1131 (1976); **D15** 2959 (1977);
H. Cheng, J.A. Dickinson, and K. Olausen, *Phys. Rev.* **D23** 534 (1981).
M. Grisar, H. Schnitzer and H.S Tsao, *Phys. Rev.* **D12**, 4498 (1973).
- [25] H. Cheng, J. Dickinson, C.Y. Lo, K. Olausen, and P.S. Yeung, *Phys. Lett.* **76B**, 129 (1978).

- [26] H. Cheng, J. Dickinson, C.Y. Lo, and K. Olaussen, *Nuov. Cim. Lett.* **25**, 175 (1979).
- [27] N.T. Nieh and Y.P. Yao, *Phys. Rev. Lett.* **32** (1974); *Phys. Rev. D***13**, 1082 (1976);
B.McCoy and T.T. Wu, *Phys. Rev. Lett.* **35**, 604 (1975); *Phys. Rev. D***12**, 3257 (1975); **D13**, 1076 (1976);
L. Tyburski, *Phys. Rev. D***13**, 1107 (1976);
L.L. Frankfurt and V.E. Sherman, *Yad. Fiz.* **23**, 1099 (1976) [*Sov. J. Nucl. Phys.* **23**, 581 (1976)];
A.L. Mason, *Nucl. Phys.* **B117**, 493 (1976).
- [28] H. Cheng and T.T. Wu, *Expanding Protons: Scattering at High Energies*, (M.I.T. press, 1987).
- [29] H. Cheng and T.T. Wu, *Phys. Rev.* **186**, 1611 (1969);
M. Levy and J. Sucher, *Phys. Rev.* **186**, 1656 (1969);
- [30] C.N. Yang and R. Mills, *Phys. Rev.* **96**, 191 (1954).
- [31] C.S. Lam and K.F. Liu, *Nucl. Phys.* **B483** 514 (1997).
- [32] Y.J. Feng, O. Hamidi-Ravari and C.S. Lam, *Phys. Rev. D***54** 3114 (1996).

- [33] Y.J. Feng and C.S. Lam, *Phys. Rev. D* **53**, 2115 (1996). Y.J. Feng and C.S. Lam, *Phys. Rev. D* **56**, 6640 (1997).
- [34] Y.J. Feng and C.S. Lam, *Phys. Rev. D* **55** 4016 (1997).
- [35] P.D. Collins, *An Introduction to Regge Theory and High Energy Scattering*, Cambridge University Press (1977).
- [36] R. Omnes and M. Froissart, *Mandelstam Theory and Regge Poles*, W. A. Benjamin Inc, 1963;
- [37] J.A. Dickinson, *Phys. Rev. D* **16**, 1863 (1977).
- [38] G.B. Arfken and H.J. Weber, *Mathematical Methods for Physicists*, Academic Press (1995).
- [39] Y.J. Feng and C.S. Lam, *Phys. Rev. D* **50**, 7430 (1994).
- [40] L.N. Lipatov, *Yad. Fiz.* **23**, 642 (1976) [*Sov. J. Nucl. Phys.* **23**, 338 (1976)].
- [41] V. Del Duca, hep-ph/9503226, published in *Scientifica Acta* Vol. 10, No.2: 91-139, 1995.
- [42] Y.J. Feng and C.S. Lam, *Evaluation of multiloop diagrams via light cone integration*, hep-ph/9707396, to appear in *J. Math. Phys.*
- [43] C.S.Lam, *Chin. J. Phys.* **35** 758 (1997); *J. Math. Phys.* **39** 5534 (1998).

- [44] C.S. Lam, Lectures given at the First Asia Pacific Workshop on Strong Interactions, Taipei. August 1st to 27th, 1996.
- [45] C.Y. Lo, Nucl. Phys. **B157**, 212 (1979); Phys. Rev. **D23**, 508 (1981);
- [46] M. Gell-Mann, Nuovo Cim. Supp. **4**, 848 (1956); Phys. Rev. **125**, 1067 (1962).
- [47] B.W. Lee and R.F. Sawyer, Phys. Rev. **127**, 2266 (1962);
- J.C. Polkinghorne, J. Math. Phys. **4**, 503 (1963);
- P.G. Federbush and M.T. Grisaru, Annals of Physics **22**, 263 (1963);
- J.D. Bjorken and T.T. Wu, Phys. Rev. **130**, 2566 (1963);
- G.Tikopoulos, Phys. Rev. **131**, 480 (1963);
- R.J. Eden, P.V. Landshoff, D.I. Olive, and J.C. Polkinghorne, *The Analytic S-Matrix*, (Cambridge University Press, 1966);
- J.V. Greenman, J. Math. Phys. **7**, 1782 (1967);
- C.S. Lam, Nuovo Simento **62A**, 97 (1969).
- [48] V.S. Fadin and L.N. Lipatov, Yad. Fiz. **50**,1141 (1989); Nucl. Phys. **B406**, 259 (1993);
- V.S. Fadin and R. Fiore, Phys. Lett. **B 294**, 286 (1992);
- V.S. Fadin, R. Fiore and A. Wuartarolo, Phys. Rev. **B50**, 5892 (1994);
- V. S. Fadin, R. Fiore and M.I. Kotsky, Phys. Lett. **B359**, 181 (1995);

V. Del Duca, *Phys. Rev. D* **54**, 989 (1996); *Phys. Rev. D* **54** 4474 (1996);

N. Armesto, J. Bartels and M.A. Braun, *Phys. Lett. B* **442**, 459 (1998);

Y.V. Kovchegov and A.H. Mueller, *Phys. Lett. B* **439**, 428 (1998).

[49] G.P. Korchemsky, *Nucl. Phys. B* **443**, 255 (1995); **462**, 333 (1996).

[50] G. Sterman, *Quantum Field Theory*, Cambridge University, 1993;